

**ORIGIN OF CARBONATE HOSTED GOLD RICH REPLACEMENT
DEPOSITS AND RELATED MINERALIZATION STYLES IN THE KETZA RIVER DEPOSIT,
YUKON TERRITORY**

by

Ana L. Fonseca

B.Sc., University of Alaska Fairbanks, 1993.

THESIS SUBMITTED IN PARTIAL FULFILLMENT OF THE REQUIREMENTS FOR THE
DEGREE OF MASTER OF SCIENCE

in

THE FACULTY OF GRADUATE STUDIES
DEPARTMENT OF EARTH AND OCEAN SCIENCES

We accept this thesis as conforming to the required standard

THE UNIVERSITY OF BRITISH COLUMBIA

May, 1998

© Ana Fonseca

In presenting this thesis in partial fulfilment of the requirements for an advanced degree at the University of British Columbia, I agree that the Library shall make it freely available for reference and study. I further agree that permission for extensive copying of this thesis for scholarly purposes may be granted by the head of my department or by his or her representatives. It is understood that copying or publication of this thesis for financial gain shall not be allowed without my written permission.

Department of EARTH AND OCEAN SCIENCES

The University of British Columbia
Vancouver, Canada

Date MAY 6, 1998

ABSTRACT

The Ketz River deposit consists of gold-rich, base metal-poor oxidized and unoxidized manto style orebodies and Fe-silicate alteration zones hosted in Early Cambrian limestones, and quartz-sulphide veins and stockwork in Late Proterozoic to Early Cambrian metasedimentary rocks. Sulphide mineralogy in unoxidized mantos, Fe-silicate alteration zones and in veins and stockwork consists mainly of pyrrhotite, pyrite, arsenopyrite, marcasite, and chalcopyrite. Minor amounts of native bismuth are present in all ore types. Gangue minerals are mainly carbonates (calcite and ankerite), and quartz. Additionally, Fe-silicate alteration zones have locally abundant magnetite and Fe-amphibole.

The area was affected by two episodes of folding, followed by two of faulting. All units exposed in the area are affected by the deformation. The two phases of folds have coincident, E-W-trending axes, and are distinguished on the basis of their vergence and nature of the axial planar foliation. First phase folds (F_1) have upright axial-planar foliation (S_1), whereas second phase folds (F_2) have moderately NE-dipping axial planar foliation (S_2) defined by spaced crenulation cleavage. Folding was followed by NNE-directed thrusting, which was in turn followed by doming and extension that produced horsts and grabens.

Arsenopyrite geothermometry was performed in ore samples from various locations in the deposit, and yielded 27.4 to 29.4 average atomic % arsenic, corresponding to temperatures below 330°C.

$^{40}\text{Ar}/^{39}\text{Ar}$ analysis of white mica from a quartz-sulphide vein gives a mid-Cretaceous (108 +/- 0.3 Ma) age for the mineralization that coincides with the emplacement of the Cassiar plutonic suite.

Lead isotopic ratios of samples from the different styles of mineralization in the Ketz River deposit plot in overlapping fields, suggesting a genetic relationship between the different ore

types. Analyses from carbonate hosted mineralization have a wider spread, suggesting more complex rock-fluid interactions or less homogenization of Pb isotopes.

The distribution of orebodies along normal faults and the coincidence of the age of mineralization with the emplacement of a plutonic suite in the region, make the Ketzá River deposit a typical intrusion centered sedimentary rock hosted hydrothermal system, with different ore manifestations according to host rock type. However, the central part of the system (the intrusive source of heat, and possibly fluids, metals, and sulphur) is not exposed.

TABLE OF CONTENTS

ABSTRACT.....	II
LIST OF FIGURES.....	VII
LIST OF PLATES.....	IX
LIST OF TABLES.....	XII
ACKNOWLEDGEMENTS.....	XIII
1. INTRODUCTION.....	1
1.1 Location and access.....	2
1.2 Goals of this study.....	2
1.3 Methods.....	2
1.4 Previous studies.....	4
1.5 Regional geology.....	4
2. STRATIGRAPHY.....	10
2.1 Unit 1a.....	10
2.1.1 Subunits of Unit 1a.....	13
2.2 Unit 1b.....	15
2.3 Unit 1c.....	15
2.4 Unit 1d.....	16
2.4.1 Facies of unit 1d.....	16
2.5 Unit 1e.....	20
2.6 Unit 2.....	22
2.7 Intrusive rocks outside the map area.....	24
3. STRUCTURAL EVOLUTION OF THE KETZA RIVER DEPOSIT.....	25
3.1 Compressional ductile deformation (D_1)	25
3.2 Compressional, non-coaxial ductile deformation (D_2)	27
3.3 Faults.....	34
3.3.1 Thrusts.....	34

3.3.2	Normal faults.....	34
3.3.3	Thrust.....	41
3.4	Discussion.....	41
4.	MINERALIZATION AND ALTERATION.....	44
4.1	Mineralization styles in the Ketzá River area.....	44
4.1.1	Carbonate hosted manto style mineralization.....	44
4.1.2	Au-rich Fe-silicate alteration.....	46
4.1.3	Metasedimentary rock hosted quartz-sulphide veins.....	46
4.2	Mineralization styles outside the map area.....	48
4.3	Alteration.....	48
4.3.1	Dolomitization and decalcification.....	48
4.3.2	Other alteration effects.....	57
4.4	Ore petrography.....	57
4.4.1	Opaque and gangue mineralogy in carbonate hosted ores.....	57
4.4.2	Opaque and gangue mineralogy in veins hosted by metasedimentary rock.....	63
4.4.3	Summary of ore mineralogy and paragenetic sequence.....	64
5.	GEOTHERMOMETRY.....	67
5.1	Arsenopyrite geothermometry.....	67
5.2	Techniques.....	69
5.3	Temperature estimates from arsenopyrite geothermometry.....	70
5.4	Fluid inclusion thermometry.....	72
6.	DATING AND PB ISOTOPIC STUDIES.....	76
6.1	Previous work.....	76
6.2	$^{40}\text{Ar}/^{39}\text{Ar}$ dating.....	76
6.2.1	$^{40}\text{Ar}/^{39}\text{Ar}$ age of mica from a quartz-sulphide vein.....	76
6.2.2	$^{40}\text{Ar}/^{39}\text{Ar}$ age of mica from a manto style orebody.....	79
6.3	Pb isotopic data.....	80
6.3.1	Techniques.....	81

6.3.2	Pb isotopic composition of samples from the Ketzal River deposit.....	82
6.3.3	Discussion.....	87
7.	SUMMARY AND DISCUSSION.....	94
7.1	Introduction.....	94
7.2	Stratigraphy.....	94
7.3	Structural geology.....	95
7.4	Mineralization and alteration.....	96
7.5	Temperature of mineralization.....	96
7.6	Relative and absolute ages of mineralization.....	97
7.7	Discussion.....	97
7.7.1	Deposit model.....	97
7.7.2	Comparisons with other manto style deposits.....	98
7.7.2.1	Midway.....	100
7.7.2.2	Central Colorado mineral belt.....	102
7.8	Recommendations for future work.....	105
8.	REFERENCES.....	106
9.	APPENDICES.....	109

LIST OF FIGURES

Figure 1.1 Schematic model for sediment-hosted disseminated Au, manto, and skarn deposits about an intrusion.....	3
Figure 1.2 Location of the Ketzra River deposit.....	3
Figure 1.3 Early to mid-Cretaceous magmatic suites in Yukon and Northwest Territories.....	7
Figure 1.4 Geological map of the Ketzra-Seagull uplift.....	8
Figure 1.5 Lithotectonic map showing the location of the Cassiar terrane.....	9
Figure 2.1 Detailed stratigraphic column for the Ketzra River area.	11
Figure 2.2 Geologic map of Ketzra River.....	12
Figure 3.1 Peel Anticline (F_1) cross-section and stereoplot.....	26
Figure 3.2 Fork Anticline (F_1) cross-section and stereoplot.	27
Figure 3.3 Break-Ridge Syncline (F_2) cross-section and stereoplot.....	28
Figure 3.4 Hoodoo Anticline (F_2) composite cross-section and stereoplot.....	29
Figure 3.5 Stereoplot of small intrafolial folds (F_2) in the Gully Zone.....	30
Figure 3.6 Stereoplot of small intrafolial folds (F_2) in the QB Zone.....	30
Figure 3.7 Stereoplot of shear joints on the Break-Ridge Syncline.....	30
Figure 3.8 Stereoplot of a-c joints in the QB zone.....	30
Figure 3.9 Cross-section showing a thrust fault cross-cutting a second phase fold.....	35
Figure 3.10 Cross-section of the Cathedral fault syncline.....	37
Figure 3.11 E-W cross –section showing the structural domains produced by normal faulting...	38
Figure 3.12 Stereoplot of b-c joints filled by calcite veins in the 1510 adit drag anticline.....	40
Figure 3.13 Cross-section showing the youngest thrust.....	42
Figure 4.1 N-S cross-section showing the location of Fe-silicate alteration zones.....	47
Figure 4.2 Paragenetic diagrams of major opaque minerals in mantos, quartz-sulphide veins, and Fe-silicate alteration zones.....	58
Figure 4.3. Paragenetic sequence of opaque and gangue minerals.....	66
Figure 5.1 Histogram of atomic % As measured in core and rim of arsenopyrite crystals.....	71

Figure 5.2 Activity of S_2 -temperature projection of stability field of arsenopyrite, showing area defined by analyses of samples from Ketz River.....	71
Figure 5.3 Geological map of Ketz River, with location of arsenopyrite geothermometry samples.	73
Figure 5.4 Histograms of atomic percent As in arsenopyrite from Ketz River.....	74
Figure 6.1 Plateau shaped (undisturbed) $^{40}\text{Ar}/^{39}\text{Ar}$ age spectrum.....	77
Figure 6.2 Saddle shaped (mixed) $^{40}\text{Ar}/^{39}\text{Ar}$ age spectrum.....	77
Figure 6.3 Geological map of Ketz River, showing location of Pb-Pb samples.....	85
Figure 6.4 Geological map of the Ketz-Seagull uplift, showing location of Pb-Pb samples from outside the map area..	86
Figure 6.5 Plot of $^{207}\text{Pb}/^{204}\text{Pb}$ versus $^{206}\text{Pb}/^{204}\text{Pb}$ and $^{208}\text{Pb}/^{204}\text{Pb}$ versus $^{206}\text{Pb}/^{204}\text{Pb}$ for samples from Ketz River, Iona Silver, and Oxo deposits.....	88
Figure 6.6 Plot of $^{207}\text{Pb}/^{206}\text{Pb}$ versus $^{208}\text{Pb}/^{206}\text{Pb}$ for samples from Ketz River, Iona Silver, and Oxo deposits.	89
Figure 6.7 Plot of $^{207}\text{Pb}/^{204}\text{Pb}$ versus $^{206}\text{Pb}/^{204}\text{Pb}$ does not represent a mixing line isochron.....	91
Figure 6.8 Plot of $^{207}\text{Pb}/^{204}\text{Pb}$ versus $^{206}\text{Pb}/^{204}\text{Pb}$ does not represent a mixing line isochron.....	92
Figure 7.1 Schematic diagram of interpreted model for the origin of the Ketz River deposit.....	99
Figure 7.2 Geological map of the Rancheria district and location of the Midway deposit.....	101
Figure 7.3 Location of the Colorado mineral belt.	103
Figure 7.4 Generalized geological map of the central Colorado mineral belt.....	103
Figure 7.5 Schematic illustration of the hydrologic model inferred for the Gilman deposit.....	104

LIST OF PLATES

Plate 2.1 Cliff of unit 1a.....	14
Plate 2.2 M-QZE (unit 1a) in drill core.....	14
Plate 2.3 M-PHYL (unit 1a) in drill core.	14
Plate 2.4 Cliff of unit 1d.	14
Plate 2.5 WBN facies in drill core.	18
Plate 2.6. Porosity in WBN.....	18
Plate 2.7 BXLT facies in drill core.	18
Plate 2.8 BXLT in gradational contact with MSLT.	18
Plate 2.9 Porosity in BXLT.....	19
Plate 2.10 MSLT facies in drill core, with locally dolomitized ooids.....	19
Plate 2.11 Porosity in MSLT1.....	19
Plate 2.12 BSLT facies in drill core.	19
Plate 2.13 Outcrop of BSLT facies overlying MSLT facies.....	21
Plate 2.14 Porosity in MSLT2.....	21
Plate 2.15 FSLT facies in outcrop.	21
Plate 2.126 CCLT facies – polished slab.	21
Plate 3.1 Vertical to overturned upper limb of the Break-Ridge Syncline.....	28
Plate 3.2 Intrafolial folds (F_2) in unit 1a.	30
Plate 3.3 Intrafolial folds (F_2) in unit 2a.	30
Plate 3.4 Photomicrograph of spaced crenulation cleavage (S_2).	30
Plate 3.5 Photomicrograph of stylolite in unit 1d.	30
Plate 3.6 Different lithologies within unit 1a develop foliation (S_2) differently.....	32
Plate 3.7 Outcrop of 1a, with S_0 , S_1 , and S_2	32
Plate 3.8 A-c joints filled by later veins.	32
Plate 3.9 Older vein boudinaged during D_2	32
Plate 3.10 Thrus fault with NNE-directed movement.	35

Plate 3.11 Topographic expression of the structural domains defined by normal faults.....	38
Plate 3.12 Massive sulphide along a-c parallel calcite veins on the 1510 adit drag anticline.....	40
Plate 3.13 1510 drag anticline.....	40
Plate 3.14 Structural complications produced by superimposed thrusting and normal faulting...	40
Plate 3.15 Mining cut in the Ridge Pit, exposing the relationship between the latest thrust and the Peel Fault.....	42
Plate 4.1 Small massive sulphide manto outcrop in MSLT facies.	45
Plate 4.2 Small oxidized manto in MSLT facies.	45
Plate 4.3 Fe-silicate alteration in drill core.	45
Plate 4.4 Oxide ore in drill core.	45
Plate 4.5 Brecciated quartz veins in outcrop.	49
Plate 4.6 Brecciated quartz vein in drill core.	49
Plate 4.7 Quartz-arsenopyrite vein hosted in unit 1a.	49
Plate 4.8 Quartz-arsenopyrite vein along a syn-D ₂ a-c joint.	49
Plate 4.9 Quartz-galena-pyrite vein in drill core.	50
Plate 4.10 Massive sulphide boulders and quartz vein in the Gully Zone.....	50
Plate 4.11 Au-bearing quartz-pyrite stringer stockwork in M-PHYL (unit 1a).....	50
Plate 4.12 Mineralized quartz-sulphide vein hosted in calcareous quartzite of unit 1a.....	50
Plate 4.13 Dolomitized oolitic lense in FSLT facies.	52
Plate 4.14 Moderate dolomitization of ooids in MSLT (drill core).	52
Plate 4.15 Strongly dolomitized MSLT outcrop.....	52
Plate 4.16 Strong decalcification and dolomitization of unit 1d in drill core.....	52
Plate 4.17 Moderate dolomitization of BXLT (drill core).	53
Plate 4.18 Pervasive dolomitization and initial oxide alteration in MSLT (drill core).....	53
Plate 4.19 Bleaching of metasedimentary rock (unit 1a) next to quartz-sulphide vein.....	53
Plate 4.20 Silicified quartzite (unit 1a) hosting quartz-sulphide stringer stockwork (drill core).....	53
Plate 4.21 Cathodoluminescence signature of invisible hydrothermal dolomitization.....	54
Plate 4.22 SEM image of hydrothermal dolomitization.	54

Plate 4.23 Cathodoluminescence signature of invisible hydrothermal calcite.....	55
Plate 4.24 SEM image of hydrothermal calcite.	55
Plate 4.25 Cathodoluminescence pattern of dolomitized ooids but no evidence of hydrothermal alteration.....	56
Plate 4.26 SEM image of hydrothermal signature enhanced along fissures.....	56
Plate 4.27 Photomicrograph of euhedral magnetite surrounded by euhedral pyrite.....	59
Plate 4.28 Photomicrograph of magnetite being replaced by pyrite, cross-cut by muscovite.....	59
Plate 4.29 Photomicrograph of early arsenopyrite cross-cut by quartz and muscovite.....	59
Plate 4.30 Photomicrograph of pyrite with bladed texture.....	59
Plate 4.31 Photomicrograph of cataclastic pyrite.	60
Plate 4.32 Photomicrograph of colloform marcasite.....	60
Plate 4.33 Photomicrograph of marcasite replacing pyrite cubes.....	60
Plate 4.34 Photomicrograph of chalcopyrite cross-cutting arsenopyrite.....	60
Plate 4.35 SEM image of native bismuth around arsenopyrite crystal.....	61
Plate 4.36 Photomicrograph of fine-grained muscovite intergrown with pyrrhotite and quartz....	61
Plate 4.37 Photomicrograph of Fe-amphibole needles and magnetite in Fe-silicate alteration...	61
Plate 4.38 SEM image of Fe-amphibole, calcite, and magnetite.....	61
Plate 5.1 Photomicrograph of arsenopyrite geothermometry assemblage.....	68
Plate 5.2 Photomicrograph of arsenopyrite geothermometry assemblage.....	68
Plate 6.1 SEM image of clean muscovite dated by $^{40}\text{Ar}/^{39}\text{Ar}$ method.....	78
Plate 6.2 SEM image of fine-grained muscovite intergrown with sulphide and quartz, dated by $^{40}\text{Ar}/^{39}\text{Ar}$ method.	78

LIST OF TABLES

Table 2.1 Summary of physical characteristics of subunits 1a through 2a.....	23
Table 3.1 Characteristics of F ₁ folds.	25
Table 3.2 Characteristic of F ₂ folds.	31
Table 4.1 Opaque mineralogy in massive sulphide mantos.	62
Table 4.2 Gangue mineralogy in massive sulphide mantos.	62
Table 4.3 Opaque mineralogy in Fe-silicate alteration zones.	63
Table 4.4 Gangue mineralogy in Fe-silicate alteration zones.	63
Table 4.5 Opaque mineralogy in metasedimentary rock hosted quartz-sulphide veins.....	64
Table 4.6 Gangue mineralogy in metasedimentary rock hosted quartz-sulphide veins.....	64
Table 5.1 Microprobe calibration standards and analytical parameters.	70
Table 5.2 Summary statistics and description of arsenopyrite geothermometry samples.....	72
Table 6.1 Common lead data for sulphides, carbonate rock, and Mississippian (?) volcanics....	83
Table 6.2 Isotopic compositions from the Iona Silver mine.	84

ACKNOWLEDGEMENTS

Throughout the preparation of this document, many people contributed their knowledge and support. My supervisor, Jim Mortensen led me by the hand across the rocky road of ignorance and into the realm of science. I owe him much for all his teachings, patience, and support. Also at UBC, Matti Raudsepp, Arne Toma, and Lori Kennedy went far out of their way to assist me since the early stages of this masters degree.

Robert Stroshein was a key person throughout the length of this project. Many of the ideas discussed in this document were originally proposed by him. Mike Cathro and Carl Schulze shared insightfull observations from their days in the Ketza River deposit.

Dan McCoy and Rainer Newberry from the University of Alaska Fairbanks guided me through the long days of arsenopyrite analyses, and spared me from a substantial amount of potential grief and pitfalls. Also in Alaska, Steve Masterman opened the doors of gold exploration for me, and saw me through a smooth and fascinating start.

Terri Maloof, Manfred Hebel, and Caroline Gemaine provided entertainment of all kinds and levels, and constantly reminded me not to spill all my marbles over rocks. Topaz followed me loyally to every outcrop.

From far away, my parents and Guy Tytgat gave me the love and support without which these two years in Vancouver would have been unbearable.

1 INTRODUCTION

The Ketza River deposit in south-central Yukon is an example of a poorly understood class of gold-rich and base-metal poor carbonate hosted manto-style replacement deposits (e.g. Titley, 1993, Sillitoe and Bonham, 1990). The deposit produced over 100 thousand ounces of gold. A broad gold-in-soils geochemical anomaly immediately north of the known gold deposit makes the Ketza River area an attractive exploration target for other mineralization styles associated with manto deposits.

Two main styles of mineralization are distinguished, based on host rock: a) Early Cambrian limestones host Au-rich manto style massive sulphide and oxidized orebodies and Au-rich Fe-silicate alteration; b) Late Proterozoic to Early Cambrian metasedimentary rocks host Au-bearing quartz-arsenopyrite veins, Au-rich massive sulphide veins and replacement orebodies, and Au-bearing stringer stockwork. Most known mineralization in the Ketza River deposit is contained in manto-style unoxidized (Lab, Peel West, Bluff zones) and oxidized (Peel Oxides, Ridge, Fork, Break, Hoodoo, Knoll zones) orebodies. Farther to the northeast, the Ag-Pb veins of the Iona Silver Mine are interpreted to be distal mineralization related to the Ketza River hydrothermal system (Cathro, 1992). This association of mineralization styles is analogous to the spectra proposed by Sillitoe and Bonham (1990) for intrusion centered systems (Figure 1.1).

An understanding of the detailed stratigraphy, structural evolution, and magmatic activity in the Ketza River area is needed for modeling ore controls and ore style zonation. The structure of the Ketza River deposit is complex, with two phases of folding followed by three generations of faults. Folds, faults, and favourable carbonate strata are the principal controls over the location of mineralization, and their recognition is the key to successful exploration.

The source of mineralizing fluids, heat, metals, and sulphur for the Ketza River deposit is not obvious. Structural setting, ore mineralogy, age constraints, and associated mineralization styles

suggest the presence of a blind intrusion. The only intrusive rocks exposed in the area are Mississippian (?) stocks and dykes that show no apparent relationship to the mineralization. A blind intrusive body related to the mid-Cretaceous Cassiar suite is speculated to have driven the hydrothermal circulation that produced the Ketz River deposit (Abbott, 1986).

1.1 Location and access

The Ketz River deposit, in the Pelly Mountains of south-central Yukon Territory, is approximately 40 km south of the town of Ross River, and less than 30 km SW of the Tintina Trench (Figure 1.2). Access from the Robert Campbell Highway is via a 40 km gravel road with no winter maintenance.

1.2 Goals of this study

The purpose of this study is to characterize the geological and metallogenic setting of the wide range of mineralization styles observed in the Ketz River area, where no exposed plutonic rocks seem to have been the source of heat, fluids, metals, or sulphur to drive hydrothermal activity, and where controls over the spatial location of orebodies were poorly understood. This project aimed at explaining the structural and stratigraphic controls over the location of orebodies, and speculating on possible sources of heat, fluids, and metals. The ultimate goal of this project is to formulate a metallogenic model to explain the location of mineralization in the Ketz River deposit and in similar geological and metallogenic settings elsewhere.

1.3 Methods

Field work involved 1:2000-scale mapping and sampling of an area of approximately 6.5 km² and re-logging over 3 km of diamond drill core. Field work concentrated on establishing stratigraphy within the mineralized units, and unravelling the structural history of the Ketz River deposit, and

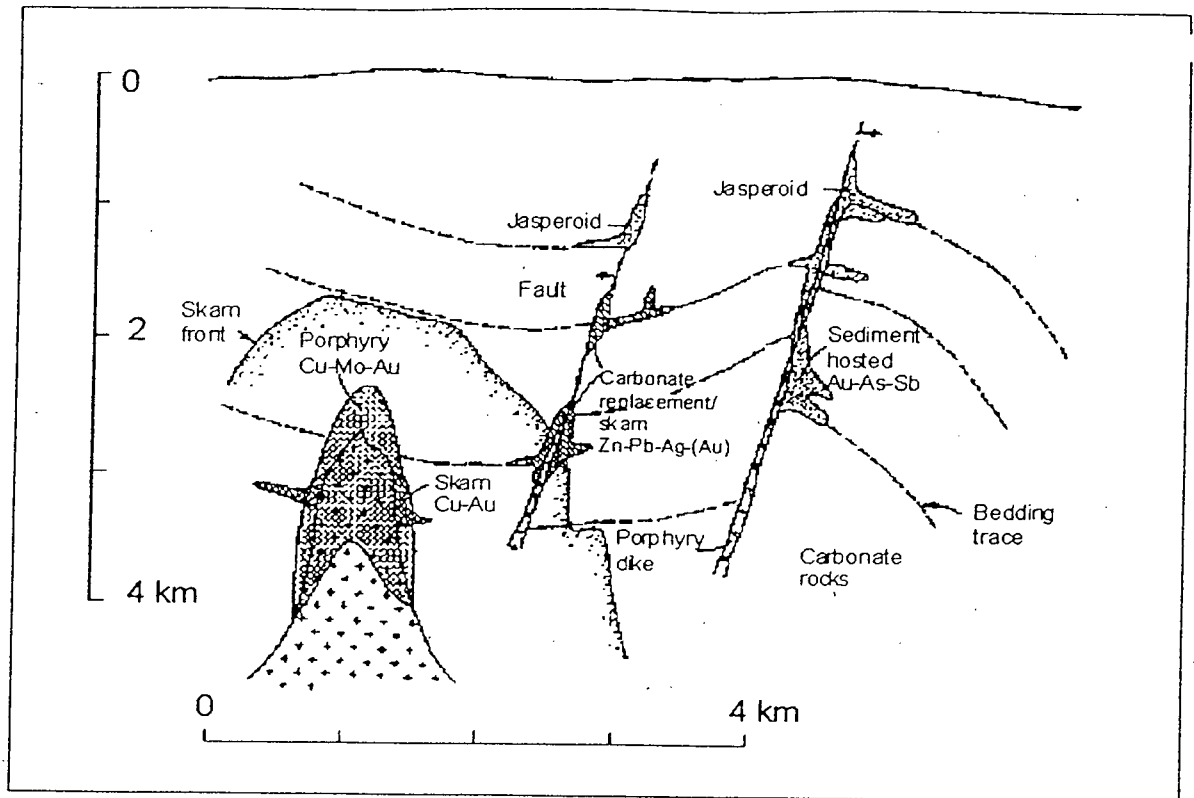


Figure 1.1. Schematic model illustrating relative positions of sediment-hosted disseminated Au, manto, and skarn deposits about an intrusive source of heat, and/or metals. From Sillitoe and Bonham, 1990.

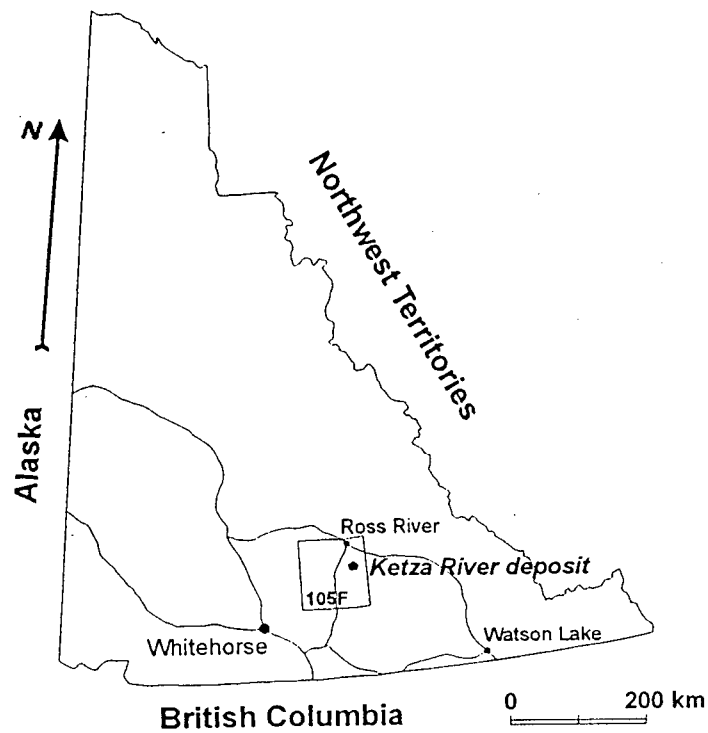


Figure 1.2. Map of the Yukon Territory, showing the location of the Ketza River deposit.

provided a geological framework for interpretation of analytical data. Analytical work involved: a) dating alteration minerals by the $^{40}\text{Ar}/^{39}\text{Ar}$ method; b) determining the isotopic signature of Pb, a trace element in the different styles of mineralization and in carbonate host rocks and intrusive rocks exposed in the area; c) constraining depositional temperatures through arsenopyrite geothermometry; d) preliminary cathodoluminescence study of alteration effects in limestone.

The results of this study shed new light on the stratigraphic and structural controls on manto-style and associated gold mineralization in the Ketzka River deposit. However, some aspects of the origin of the deposit, particularly the mechanism driving hydrothermal activity, remain unresolved.

1.4 Previous studies

Three previous studies were carried out at the Ketzka River area. Read (1980) described and divided the Lower Cambrian through Upper Cambrian stratigraphy, sedimentary features, and fossil record in the Ketzka River area. Cathro (1992) provided detailed petrographic descriptions of sulphide minerals in the manto-style ores, geochemical analyses of the carbonate minerals in the host rock, and a comprehensive summary of local stratigraphy, regional geology, and exploration and production history. Staveley (1992) determined stable isotope ratios in quartz veins and carbonate rocks, and studied fluid inclusions in quartz veins from a number of localities and rocks in the Ketzka River area.

1.5 Regional geology

Abbott (1986) described the geology and metal occurrences of the Ketzka River and Seagull Creek areas, and Cathro (1992) provided a summary of the depositional and tectonic history of the Pelly-Cassiar platform. The overall structural setting of the central Pelly Mountains was described by Templeman-Kluit (1977b), and Mortensen (1982).

Platformal carbonate and clastic units underlying the Ketz River area were deposited in Late Proterozoic to mid-Paleozoic time. From Early Cambrian through Devonian time, the Pelly-Cassiar platform was an area of positive relief separated from the North American margin by the Selwyn Basin to the east. The Pelly-Cassiar Platform and the Selwyn Basin were part of the west facing North American miogeocline. Deposition of typical miogeoclinal clastic and carbonate units in the Pelly-Cassiar platform was interrupted at the Precambrian-Cambrian boundary (Fritz and Crimes, 1985), Lower to Upper Cambrian boundary (Fritz et al., 1991), and in the Upper Devonian (Gordey, 1991). By Late Devonian the Pelly-Cassiar Platform had ceased to exist, and younger clastic units were deposited in a basinal environment. The main part of the miogeoclinal section exposed in the Ketz River area consists of Late Proterozoic to Early Cambrian siliciclastic and carbonate rocks.

Mississippian time in the Pelly-Cassiar platform area was characterized by widespread eruption of alkaline volcanics and emplacement of associated syenitic intrusions in the area north of Ketz River. Upper Devonian through Mississippian was a time of block faulting in the subsiding Pelly-Cassiar Platform (Gordey, 1991). Volcanogenic massive sulphide prospects associated with Mississippian felsic volcanic rocks are common along the McConnel and Seagull Creek, and Indigo Lake areas (e.g. Mortensen, 1982, Doherty, 1997, Holbek and Wilson, 1998).

In the Mesozoic, rocks of the Pelly-Cassiar Platform were deformed and intruded by granitic plutons. The absolute ages of Mesozoic deformation events are poorly constrained, and mechanism driving Mesozoic deformation inboard of the western North American marginal arc poorly understood.

Mortensen (1982) mapped an area of approximately 500 km² immediately to the north and west of the Ketz River deposit. He reported two prominent sets of folds with coincident, generally NW-trending axes associated with lower to upper greenschist facies metamorphism. These two early folding events are separated by thrust faulting. A third, poorly developed set of folds formed

NE-trending regional warps. Mortensen (1982) observed that NE-directed thrust faults are folded along second phase folds. Gordey (1981) mapped the Indigo Lake area of the Cassiar Terrane, approximately 50 km southeast of the Ketzka River deposit, and reported a single set of NW-trending folds associated with NNE-directed thrusts. Thrust to fold transitions are common in the Indigo Lake area.

Cretaceous magmatism in the Yukon comprises several spatially, compositionally, and temporally distinct plutonic suites (Mortensen, 1998) (Figure 1.3). The Cassiar Suite, an elongate NW-trending belt of predominantly biotite-granite and granodiorite plutons that lack coeval volcanic rocks straddles the Ketzka River deposit. Felsic plutonic rocks of the Cassiar Suite comprise mainly crustally derived melts (Driver, 1998). The largest pluton of the Cassiar Suite is the Cassiar Batholith, with K-Ar ages on biotite ranging from 85 to 110 Ma, and a whole rock Rb-Sr isochron of 109 Ma (Woodsworth et al., 1991). No Cretaceous plutonic rocks are exposed or have been intersected by drilling in the Ketzka River area, but a small body of Cretaceous quartz-monzonite was mapped (Templeman-Kluit, 1977a) approximately 12 km southeast of the deposit area. Abbott (1986) defined the Ketzka-Seagull arch (Figure 1.4) as a wide Cretaceous window exposing strata of structurally lower units and containing abundant epigenetic Au-Ag occurrences. Abbott (1986) proposed three possible origins for the arch: a) doming and uplift around a buried Cretaceous intrusion; b) uplift by a step on a thrust floor; or c) a combination of the previous two models.

Early Tertiary, mainly strike-slip dextral motion along the Tintina Fault system displaced the prong-shaped Cassiar Terrane, which contains the Pelly-Cassiar platform (Figure 1.5). By Early Tertiary time, the elongate Cassiar Terrane had moved over 450 km to the NW of its initial position and was placed in structural contact with rocks of the Yukon Tanana Terrane on both sides.

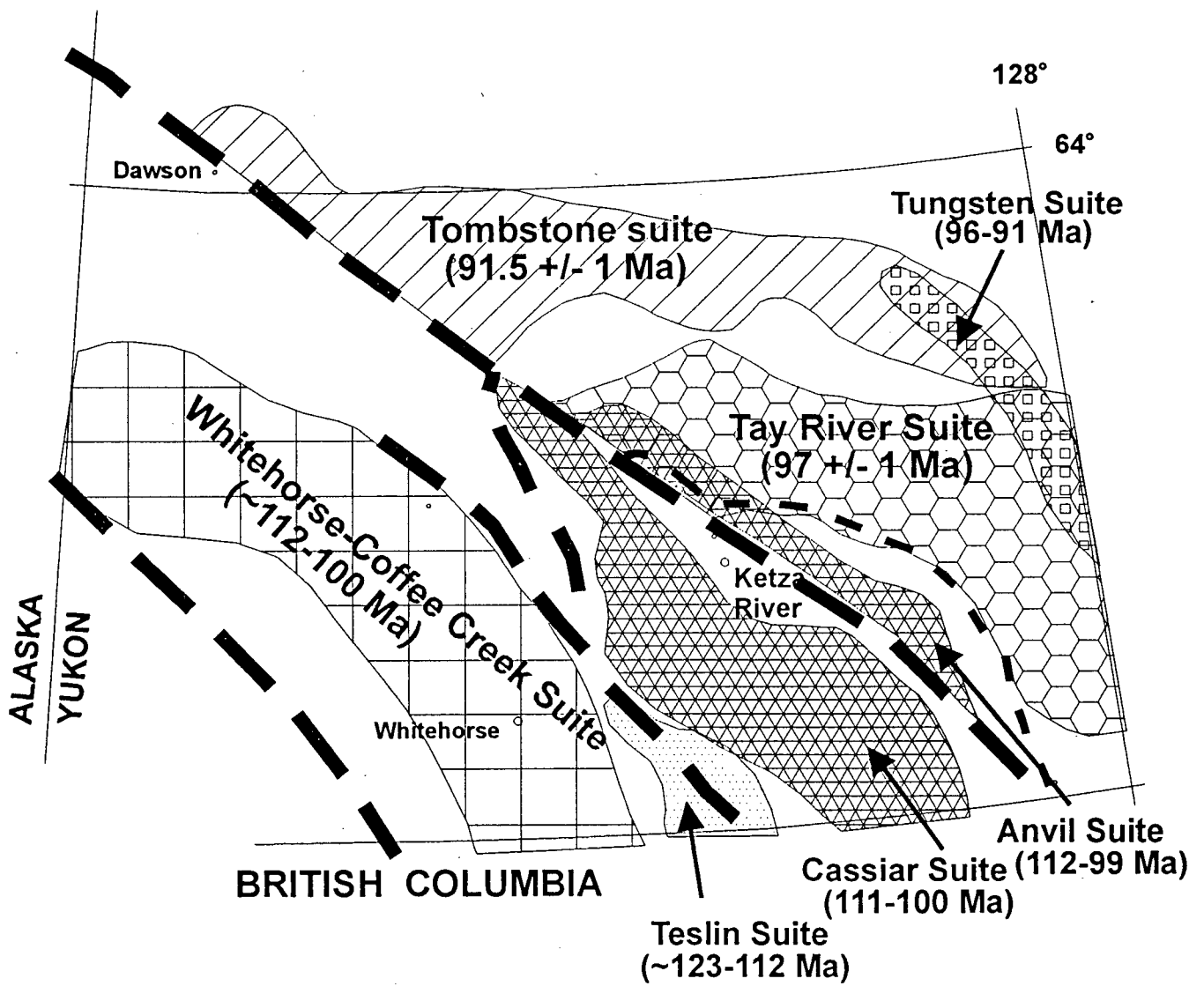


Figure 1.3. Early to mid-Cretaceous magmatic suites in Yukon and Northwest Territories (modified from Mortensen, 1998).

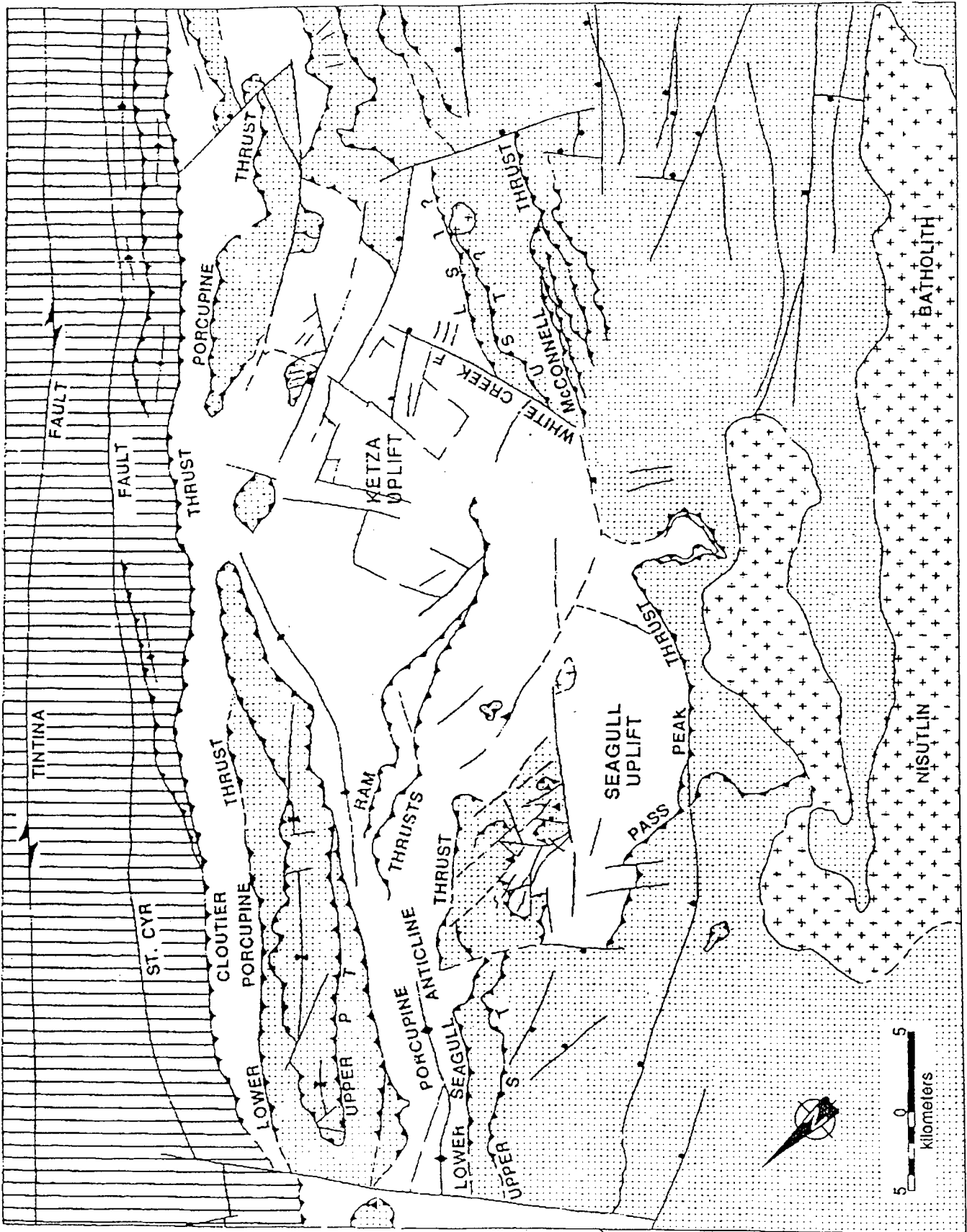
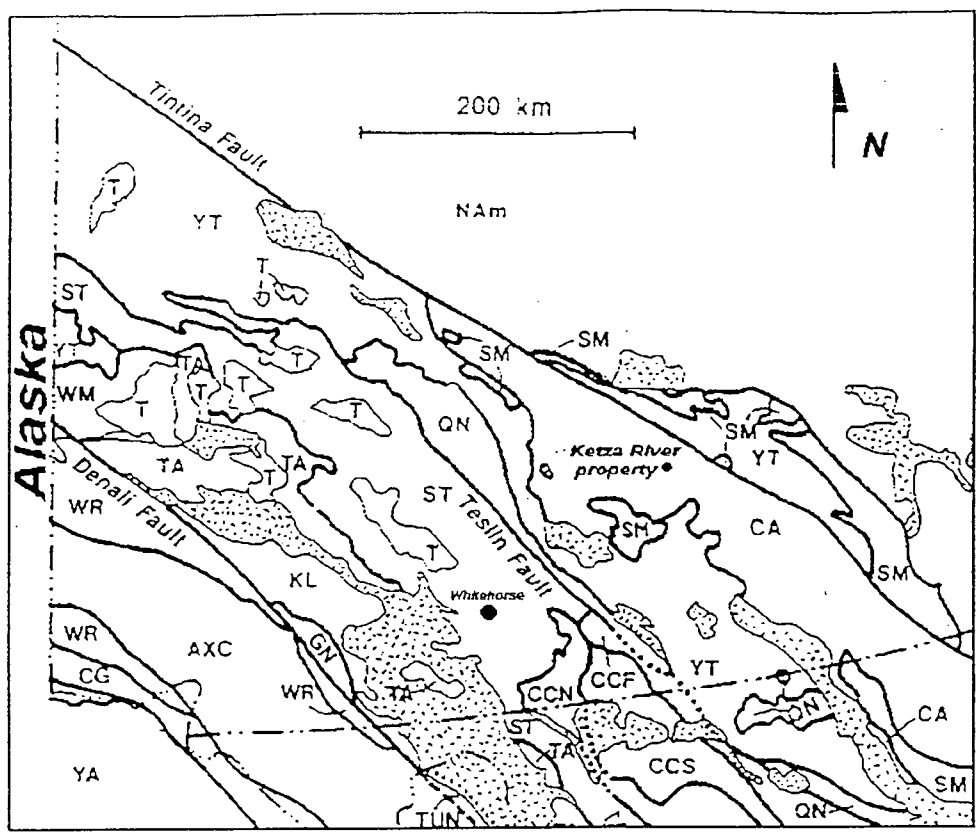


Figure 1.4. Geological map of the Ketza-Seagull uplift. Modified from Abbott, 1986.



LEGEND

Accreted Terranes

- | | | |
|-------------------------------|---------------------|---------------------|
| AX - Alexander | CG - Chugach | TA - Tracy Arm |
| AXC - Craig subterrane | KL - Kluane | TUN - Taku |
| CA - Cassiar | QN - Guesneilia | WM - Windy-McKinley |
| CC - Cache Creek | SE - Saint Elias | WR - Wrangellia |
| CCF - French Range subterrane | SM - Slide Mountain | YA - Yakutat |
| CCN - Nakina subterrane | ST - Stikinia | YT - Yukon-Tanana |
| CCS - Sentinal subterrane | | |

Other Rocks

- | | | |
|--|--------------------------|--|
| NAM - North American craton | T - Tertiary cover rocks |  Plutonic rocks |
| GN - Gravina-Nutzotin Overlap Assemblage | | |

Symbols

-  Terrane-bounding fault (dashed where approximate, dotted where covered)
-  Post-amalgamation or post-accretion contact (depositional and intrusive)

Figure 1.5. Lithotectonic terrane map showing the Cassiar terrane emplaced between two slices of Yukon Tanana Terrane. Modified from Monger and Berg, 1984.

2 STRATIGRAPHY

Wheeler et al. (1960) divided Upper Proterozoic and Paleozoic rocks of the Quiet Lake map area into 8 units. Unit 1 consists of a 700 m thick succession of Lower Cambrian rocks subdivided into lower quartzite, medial shale, and upper carbonate units. Read (1980) further subdivided unit 1 into five lithologically distinctive subunits: 1a through 1e. These units have sharp and unequivocal contacts (except for the assigned 1c/1d contact), and lack evidence for significant depositional hiatuses. Based on the fossil record (mainly archeocyathids and trilobites), Read (1980) assigned a Late Proterozoic to Early Cambrian age to rocks of unit 1, and correlated them with the Sekwi Formation of the Mackenzie and Selwyn mountains, and the Atan Group of the Cassiar Mountains.

This study further subdivided subunit 1d into several mappable limestone facies, and identified marker beds within subunit 1a. Table 2.1 is a summary of physical characteristics of subunits 1a through 2a, based on the results of this study. Figure 2.1 is a generalized composite columnar section for the Ketz River area.

2.1 Unit 1a

Unit 1a consists of rusty- and recessive-weathering shale, siltstone, quartzite, and calcareous quartzite. On the south side of Peel Creek (Figure 2.2), unit 1a forms steep cliffs (plate 2.1). The typical mineral assemblage in rocks of unit 1a is quartz, muscovite, and chlorite, which correspond to the chlorite zone of greenschist facies metamorphism (Yardley et al., 1990). Because of its characteristic colour and foliated nature, and apparently monotonous fine-grained composition, the field name of "argillite" is used for unit 1a.

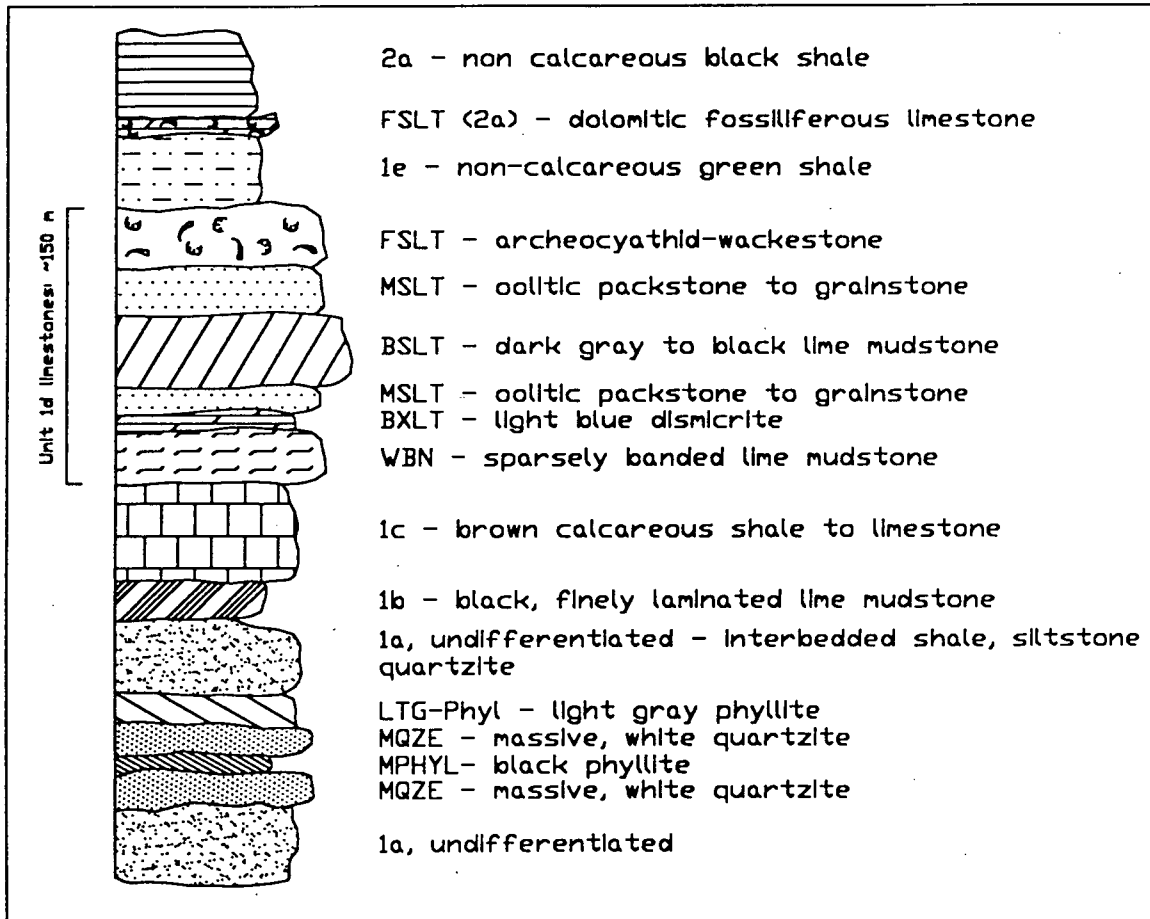


Figure 2.1. Detailed stratigraphic column for the Ketz River area. Horizontal widths represent resistance to weathering.

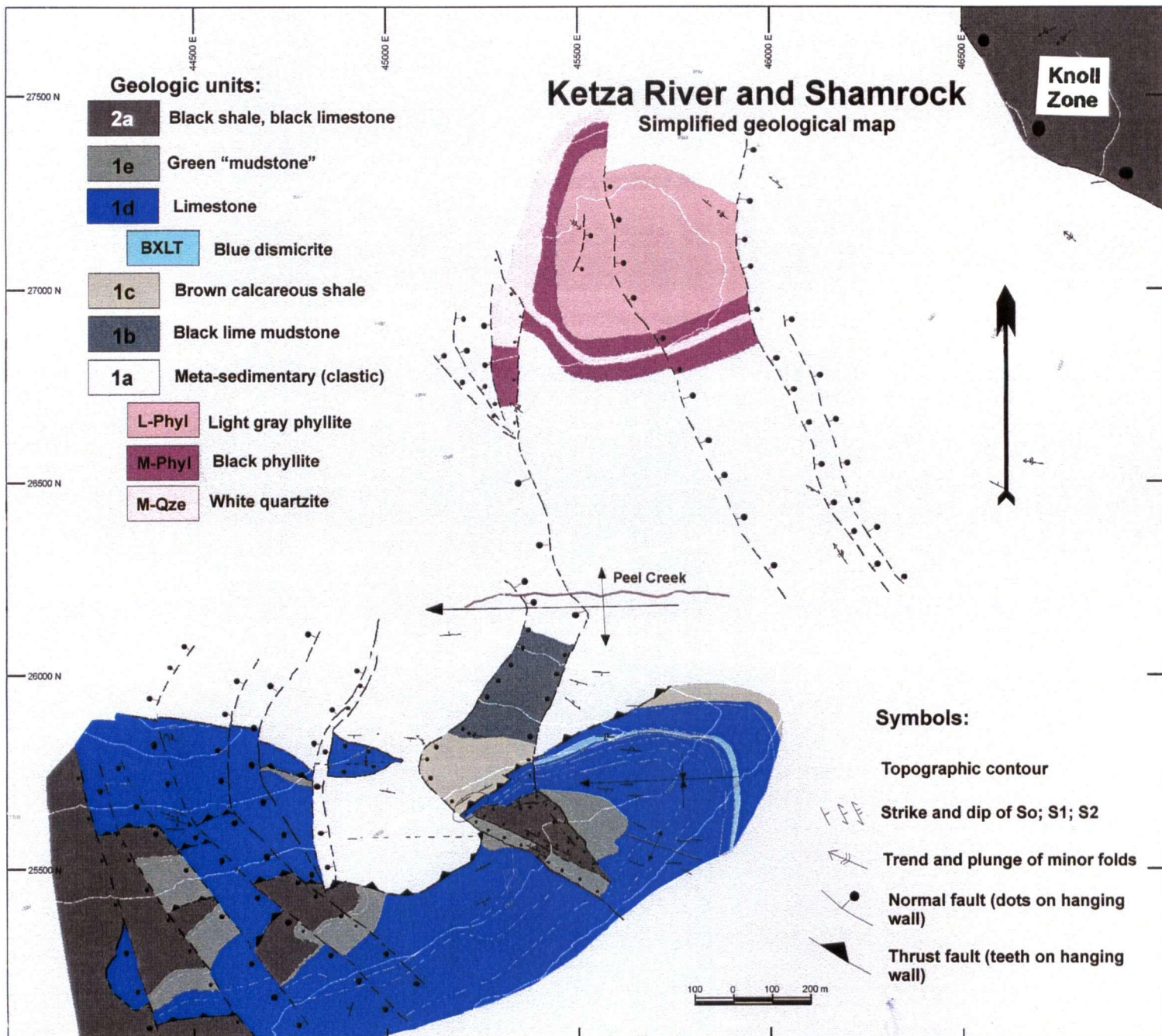


Figure 2.2 Geological map of Ketz River and Shamrock zone, showing the location of Peel Creek.

The lower contact of unit 1a is not exposed in the map area. The upper contact is gradational into black lime mudstone of unit 1b, and is only exposed in faulted blocks. Total thickness of unit 1a in the map area, estimated from surface mapping and drill hole data, is over 250 m.

Sedimentary features are sparsely developed in unit 1a, and evidence for bioturbation is rare. Rare cross-lamination in quartzite beds provide the only top indicators.

2.1.1 Subunits of Unit 1a

The following marker beds were recognized and mapped (from oldest to youngest):

a) M-QZE1: Light gray to white, massive quartzite, homogeneously coarse-grained (plate 2.2).

The thickness of this subunit varies from 25 to 30 m.

b) M-PHYL: Recessive weathering, distinctive dark gray phyllite (plate 2.3). No coarser-grained interbeds were identified. Tectonic foliations are very well developed in this unit, and transposed bedding is common. Contacts with massive quartzite above and below are sharp and unequivocal. This unit is 15 to 20 m thick.

c) M-QZE2: Light gray to white, massive quartzite. It lacks finer-grained interbeds, and is only distinguishable from M-QZE1 by its stratigraphic position and difference in true width. The width of this unit is 35 to 40 m.

d) LTG-PHYL: Recessive-weathering light gray phyllite with minor silty interbeds. Tectonic foliations are very well developed, and bedding is commonly transposed. The contact with massive quartzite below (M-QZE2) is gradational.

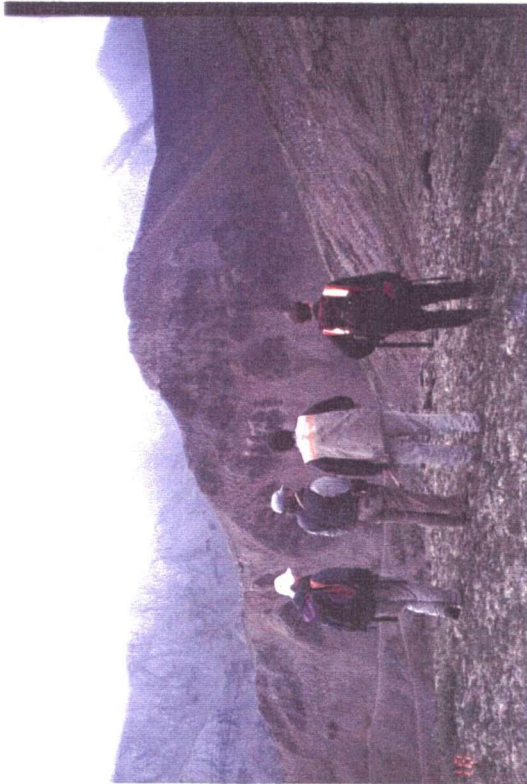


Plate 2.1. Cliff at background formed by rusty-weathering metasedimentary (clastic) rocks of unit 1a. Looking S.



Plate 2.2. M-QZE (unit 1a) massive, light gray to white quartzite. HQ core. Core diameter = 61 mm.



Plate 2.3. M-PHYL - black phyllite is the most conspicuous marker within unit 1a. HQ core. Core diameter = 61 mm.



Plate 2.4. Cliff of 1d limestones, immediately south of the map area. Looking SW.

The lack of supratidal and intertidal features such as flaser bedding, dessication structures, etc., suggests subtidal deposition.

The alternation of medium and fine-grained sediments suggest that unit 1a was deposited on a shallow marine, intermittently agitated environment. Massive quartzite beds (M-QZE1 and M-QZE2) and lenses are the result of stronger currents.

The lack of bioturbation in coarse siltstones and quartzites suggests rapid sedimentation.

2.2 Unit 1b

Unit 1b consists of black, finely laminated lime mudstone. Contacts with 1a and 1c are gradational where exposed in the map area. In the map area, unit 1b is not exposed in its full width, but outside the map area its width varies from 35 to 60 m (Read, 1980). Fossils and bioturbation were not observed.

Unit 1b precipitated in a low energy, subtidal, restricted environment as indicated by the lack of fossils, bioturbation, and traction current structures, absence of supratidal features, and abundance of mud. Parallel silty laminations indicate periodic changes in current velocity or sediment supply.

2.3 Unit 1c

Unit 1c consists of recessive-weathering, light brown calcareous shale to limestone. Calcareous content increases upwards. Contacts with unit 1b are gradational. The contact with unit 1d was arbitrarily defined as the point where calcareous material makes up approximately 50% of the rock (Read, 1980). Exposures of unit 1c in the map area are restricted to faulted blocks. Outside the map area, unit 1c is 75 to 105 m thick (Read, 1980). Fossils are rare, and include small

trilobites in the lower (more clastic) part, and more common archeocyathids toward the top (limestone).

Unit 1c was deposited in a low energy, subtidal environment, as indicated by the predominance of fine-grained clastic sediments, and absence of current or supratidal features. The scarcity of fossils in the lower part of this lithology could indicate restricted conditions, whereas the presence of archeocyathids towards the top suggests a change towards normal open marine conditions.

2.4 Unit 1d

Limestones of unit 1d form resistant cliffs (plate 2.4). Unit 1d hosts nearly all of the manto-style mineralization in the Ketzá River area, and facies variations within this unit were carefully examined and documented in order to evaluate possible lithological controls on the localization of mineralization and facilitate recognition of minor fault offsets. Unit 1d limestones were subdivided into eight facies. The total thickness of unit 1d is 150 to 180 m. Contacts with unit 1c are defined at the point where the rock is composed of 50% carbonate sediments and 50% clastic sediments. Contacts with unit 1e are gradational.

2.4.1 Facies of unit 1d

Seven facies are laterally continuous and mappable. Contacts are gradational, and are more easily identified in drill core than in outcrop. Facies are distinguishable at a macroscopic (outcrop and diamond drill core) scale. The continuous units are described below from oldest to youngest. Facies are named according to the carbonate rock classification scheme of Dunham (1962), and crystalline carbonate rocks are named according to the classification of carbonate textures of Folk (1962). In the rocks described below, porosity volume was quantified from thin sections, and therefore may not represent the total porosity of these units.

- a) WBN ("wispy banding limestone"): Light gray, sparsely banded, weakly to moderately recrystallized lime mudstone (plate 2.5). This unit is 35 to 40 m thick. The recrystallized nature of WBN makes it one of the preferential ore hosts along fold hinges, where secondary fracture porosity (plate 2.6) amounts to up to 7% of the rock volume. WBN hosts the deepest manto-style orebodies in the Ketzal River area. Fossils are rare, and are limited to small archeocyathids.
- b) BXLT ("blue crystalline limestone"): Light blue, diamicrite (plates 2.7 and 2.8). Thickness varies from 15 to 20 m. The brittle character of BXLT produced enhanced fracture porosity (plate 2.9), especially along large-scale fold hinges. Secondary fracture porosity locally reaches 12% of rock volume. BXLT is host to the largest manto-style and skarn orebodies at Ketzal River. Surface weathering produces a characteristic yellow staining. Jointing is very well developed in BXLT outcrops, and in drill core it is typically moderately to highly broken. The absence of fossils may be due to complete recrystallization.
- c) MSLT1 ("massive oolitic limestone"): Light to medium gray, oolitic packstone to grainstone (plates 2.8 and 2.10). Thickness is approximately 20 m. Secondary intraparticle (oolitic) porosity (plate 2.11) locally reaches 20% of rock volume, and makes MSLT1 one of the favourable replacement ore hosts. Outcrops are generally massive and unjointed. Fossils are sparse.
- d) BSLT ("black silty limestone"): Dark gray to black, intensely bioturbated lime mudstone (plates 2.12 and 2.13). BSLT is characterized by abundant irregular and discontinuous ("swishy") calcite stringers. Thickness is 20 to 25 m. Silty patches and pockets are common, and usually display evidence of soft-sediment deformation. Outcrops do not display significant jointing. Small archeocyathid fossils are abundant. Due to the high detrital content and lack of porosity, BSLT generally does not host orebodies.



Plate 2.5. WBN facies (unit 1d) - light gray, sparsely silty banded lime mudstone. NQ core. Core diameter = 45 mm.

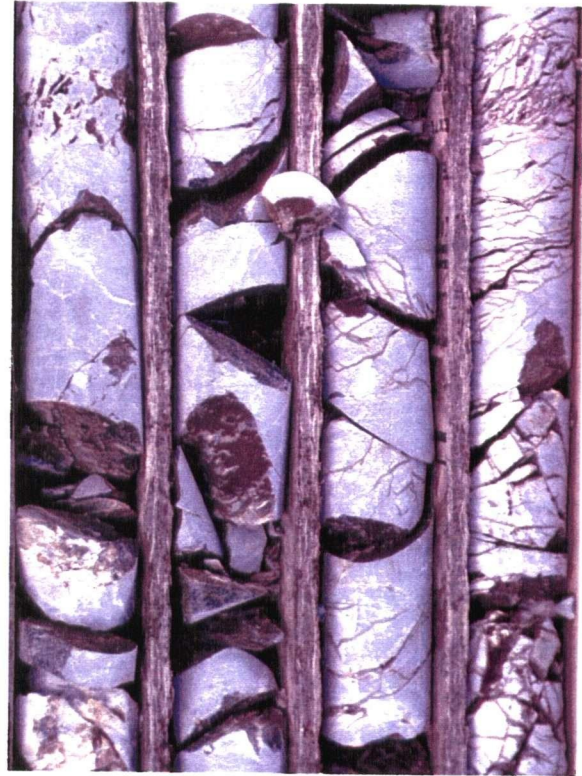


Plate 2.7. BXLT (unit 1d) - blue, coarsely crystalline dismicrite, with abundant fractures. NQ core. Core diameter = 61 mm.



Plate 2.6. Secondary fracture enhanced porosity (12%) in WBN. Field of view = 1 mm.

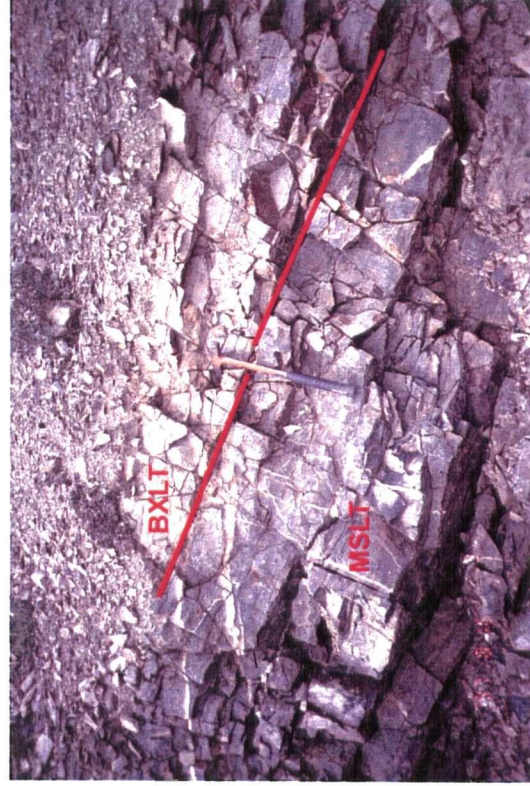


Plate 2.8. BXLT (above, light blue) in gradational contact with MSLT (below, medium gray).

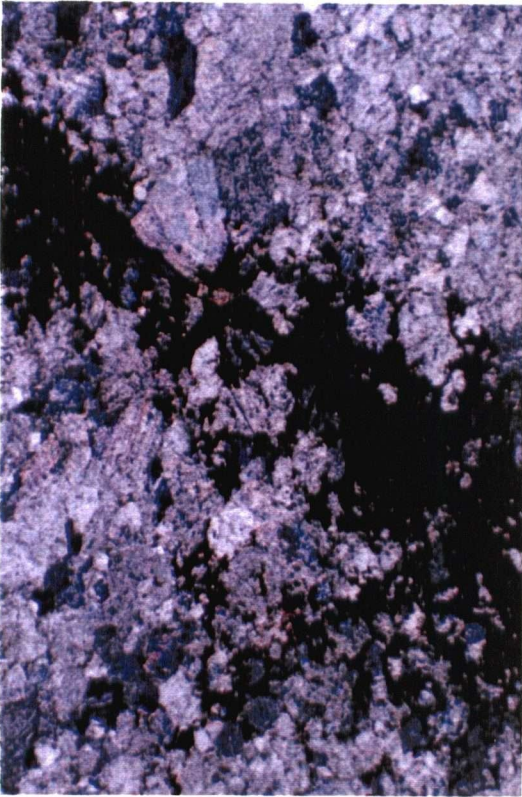


Plate 2.9. Secondary fracture enhanced porosity (dark, approximately 12%) in BXL1. Field of view = 1 mm.

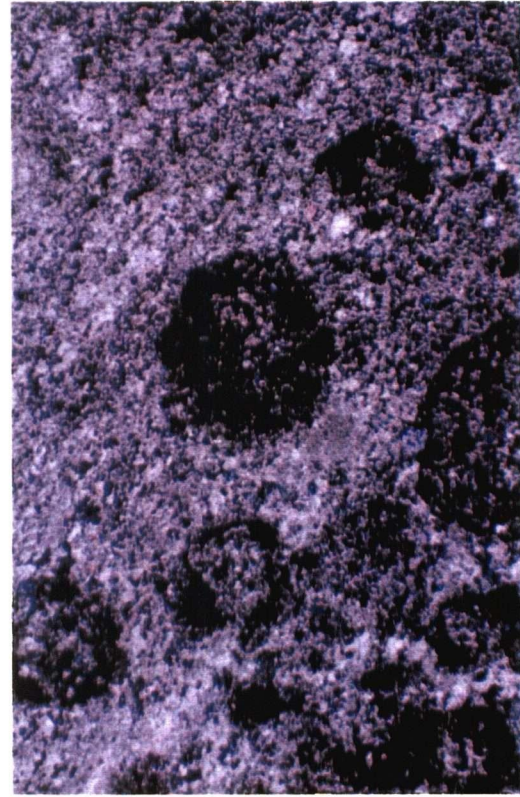


Plate 2.11. Secondary enhanced intraparticle (oolitic) porosity (~20%) in MSLT1. Dark areas are pores. Field of view = 1 mm.

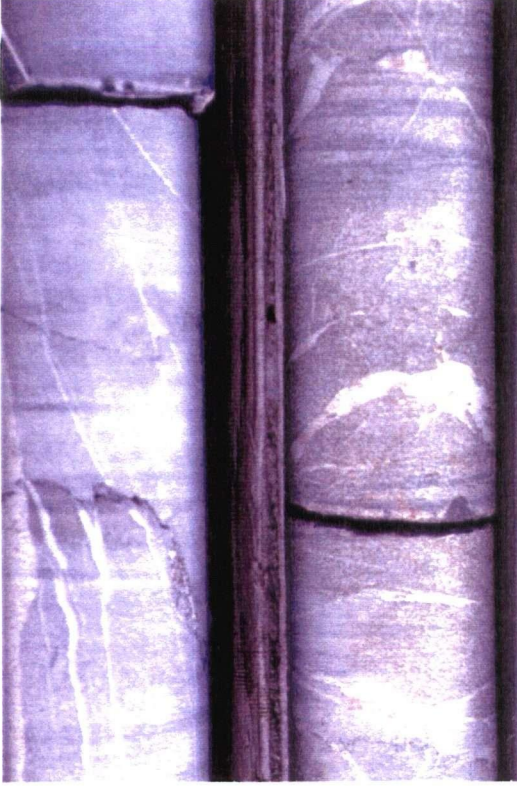


Plate 2.10.MSLT (unit 1d) - massive oolitic grainstone to packstone, with locally dolomitized ooids. NQ core. Core diameter = 47 mm.



Plate 2.12.BSLT (unit 1d) - black, silty lime mudstone with soft sediment deformation features. HQ core. Core diameter = 61 mm.

- e) MSLT2 ("massive oolitic limestone"): Medium gray oolitic packstone to grainstone. MSLT2 is similar to MSLT1, but darker gray, and less porous. Thickness is 20 to 25 m. Low secondary intraparticle (oolitic) porosity (plate 2.14) represents less than 7% of rock volume. This unit hosts a few, discontinuous manto-style orebodies.

- f) FSLT ("fossiliferous limestone"): Medium to dark gray archeocyathid-bearing wackestone (plate 2.15). Thickness is approximately 30 m. Fossil recrystallization produced reduced porosity (generally < 3%), which hindered the development of orebodies in this facies. Outcrops are recognized by abundant archeocyathids and irregular silty bands. Oolitic lenses up to 3 m wide are common within the FSLT facies.

Two other facies are recognized locally, but cannot be mapped as laterally continuous units:

- a) MARBLE: White dismicrite found along the 1d/1c contact beneath the Break zone only (Figure 2.2).

- b) CCLT ("calic limestone"): Striped, light blue and white, pervasively recrystallized archeocyathid-bearing marble (plate 2.16). CCLT forms discontinuous lenses up to 7 m thick, at various parts of unit 1d.

The lack of supratidal features, and the increase in archeocyathid content towards the top of the section suggests that carbonate precipitation in unit 1d took place in increasingly warm, shallow water, in a subtidal platformal environment. Subunit BSLT represents a period of greater agitation, and enough circulation for organisms to thrive, producing bioturbation. Subunit MSLT forms continuous oolitic beds rather than the typical lateral ooid shoals observed in modern carbonate platforms.

2.5 Unit 1e

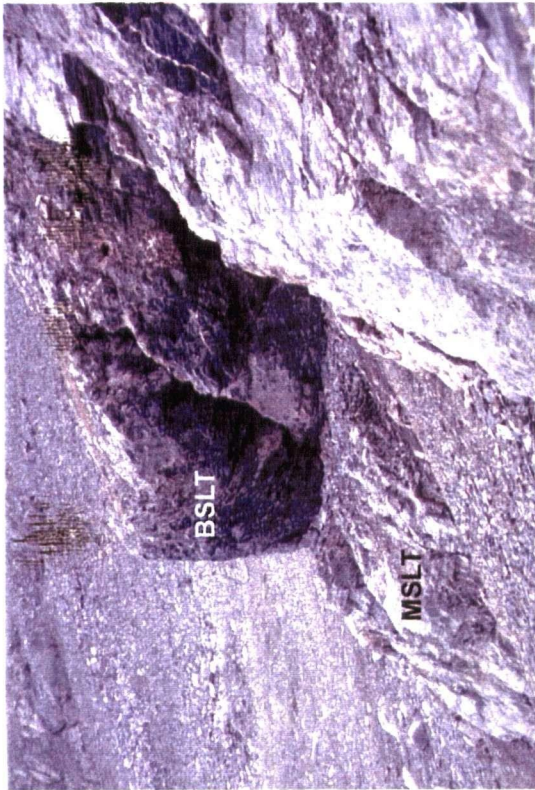


Plate 2.13. BSLT (above, dark) in contact with MSLT (below, medium gray).

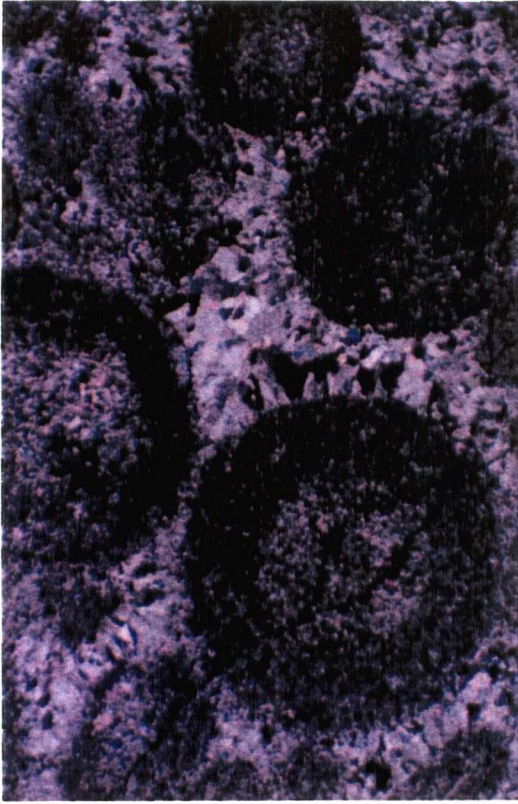


Plate 2.14. Recrystallization reduced intraparticle (oolitic) porosity (<3%) in MSLT2. Field of view = 1 mm.



Plate 2.15. FSLT (unit 1d) - archeocyathid wackestone.

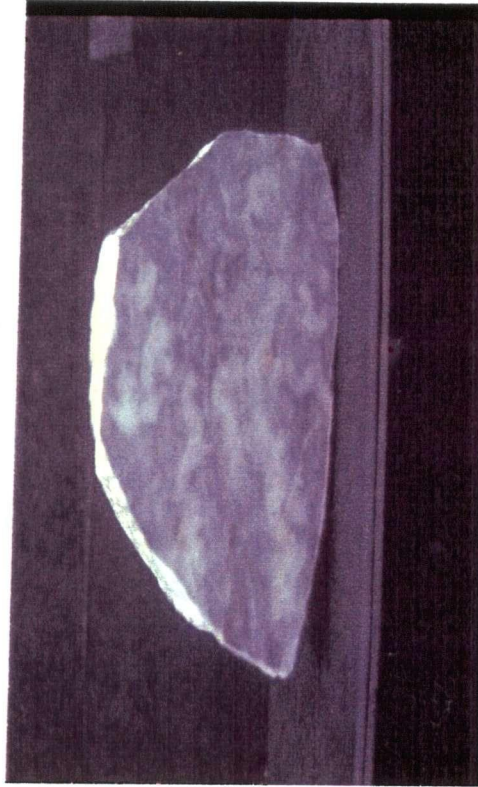


Plate 2.16. CCLT (unit 1d) - light blue-gray and white marble. CCLT forms discontinuous lenses throughout 1d lithology.

Unit 1e consists of light green phyllite with lenses of dolomite. Its maximum thickness is 90 m (Read, 1980). In the map area, unit 1e has an unconformable upper contact, which results in highly variable thickness. Contacts with the underlying unit 1d are gradational from archeocyathid-rich wackestone (FSLT facies) to green phyllite. The light green phyllite consists of recessive-weathering, non-calcareous phyllite with two well developed foliations. Dark gray to orange dolomitic archeocyathid-wackestone or oolitic grainstones form irregular and discontinuous lenses, up to 7 m thick.

The presence of abundant archeocyathids suggests a shallow marine, intermittently agitated, subtidal environment with good water circulation. Intermittent current or wave activity produced lenses of high energy deposits (oolitic grainstone) interbedded with the green phyllite.

2.6 Unit 2

Rocks of unit 2 are of Upper Cambrian to Ordovician age (Read, 1980). The thickness of unit 2 can exceed 1000 m (Cathro, 1992). Within the map area, the greatest thickness of unit 2 rocks is approximately 35 m. The lower contacts are erosional, and the upper contacts are not exposed.

Unit 2 is composed of two major lithologies:

- a) Recessive weathering, fissile black shale with two well developed foliations. Black shale of unit 2 is the stratigraphically highest unit exposed in the southwest part of the map area. No mineralization is associated with black shales.
- b) Dark gray to black, coarse dismicrite to laminated lime mudstone. This rock type has well developed foliation and intrafolial folds. The Knoll manto-style orebody (Figure 2.2) is hosted in limestone of unit 2a.

Restricted conditions and anoxic waters were the likely environment of deposition for the black shales. A change to more agitated waters led to the deposition of limestones.

Table 2.1 Summary of physical characteristics of units 1a through 2a.

unit	field name	sediment type	outcrop/weatherin	colour
1au	argillite	terrigenous	rusty, recessive	light yellow to gray
M-QZE1 (1a)	massive quartzite	terrigenous	resistant	light gray to white
M-PHYL (1a)	massive phyllite	terrigenous	recessive	dark gray to black
M-QZE2 (1a)	massive quartzite	terrigenous	resistant	light gray to white
LTG-PHYL	light gray phyllite	terrigenous	rusty, recessive	light gray
1b	black limestone	chemical	resistant	black
1c	calcareous shale	terrigenous (bottom) chemical (top)	recessive	light yellow to brown
WBN (1d)	wispy banded limestone	chemical	resistant, jointed	light gray
BXLT (1d)	blue crystalline limestone	chemical	resistant, jointed	light blue
MSLT1 (1d)	massive oolitic limestone	chemical	resistant	light to medium gray
BSLT	black limestone	chemical	resistant	dark to medium gray
MSLT2 (1d)	massive oolitic limestone	chemical	resistant	medium gray
FSLT	fossiliferous limestone	chemical	resistant	medium to dark gray
1e	mudstone	terrigenous/chemical	recessive	light green
2a	poker chip black limestone	terrigenous/chemical	recessive	black

unit	rock types	penetrative structures	width	sedimentary structures	fossils
1au	phyllite, quartzite, slate calcareous quartzite,	2 well developed foliations	>250 m	few cross-laminations	local bioturbation
M-QZE1 (1a)	quartzite	poorly developed foliations	25-30 m	few cross-laminations	
M-PHYL (1a)	phyllite	2 well developed foliations tight intrafolial folds	15-20 m		
M-QZE2 (1a)	quartzite	poorly developed foliations	35-40 m		
LTG-PHYL	phyllite	2 well developed foliations tight intrafolial folds	35 m		
1b	lime mudstone	2 well developed foliations intrafolial folds	35-60 m (Read, 1980)	silt laminae	
1c	calcareous shale, lime mudstone	2 moderately developed foliations	75-105 m (Read, 1980)		trilobite fragments archeocyathids
WBN (1d)	lime mudstone		35-40 m	discontinuous, fine clay to silt lenses	
BXLT (1d)	dismicrite		15-20 m		
MSLT1 (1d)	oolitic packstone to grainstone		20 m		archeocyathids
BSLT	lime mudstone		25-30 m	soft sediment deformation of small clay to silt lenses	bioturbation
MSLT2 (1d)	oolitic packstone to grainstone		20-25 m		archeocyathids
FSLT	archeocyathid-bearing wackestone		25-30 m		archeocyathids trilobites
1e	slate, dolomitic lime mudstone to archeo- cyathid-wackestone	2 well developed foliation	40-90 m		archeocyathids
2a	slate, lime mudstone	2 well developed foliations intrafolial folds	>1000 m (Read, 1980)	silt laminae	

2.7 Intrusive rocks outside the map area

Two intrusive bodies are found within 3 km of the map area. Cathro (1992) mapped a light green, pervasively foliated and altered dyke approximately 1 km east of the map area, and interpreted it as being associated with the Mississippian volcanic rocks that are common in the Cassiar Terrane. Templeman-Kluit (1977a) reported a 2 km wide quartz monzonite stock of inferred mid-Cretaceous age approximately 8 km southwest of the map area.

3 STRUCTURAL EVOLUTION OF THE KETZA RIVER DEPOSIT

The structural style of the Ketza-Seagull district area is dominated by N-verging thrust faults (Abbott, 1986) and NW-trending folds. In the area of the Ketza River deposit, E-W-trending folds, NNE-directed thrusts, and NNW-trending normal faults characterize the main structural style. Unravelling the sequence of folds and faults in the deposit was critical for the interpretation of analytical results discussed in later chapters. The individual deformation events in the study area are described from oldest to youngest in the following sections. Two main compressional events were followed by extension, which in turn was followed by a late compressional event.

In this chapter, structures mapped are referred to according to the right hand rule.

3.1 D₁ – Compressional ductile deformation

The first deformation event produced large scale, open, E-W-trending folds (F₁) and a generally upright axial planar foliation (S₁). The Peel Anticline (Figure 3.1) and the Fork Anticline (Figure 3.2) are the only two large scale folds (F₁) in the map area. The axis of the Peel Anticline is located slightly south of and parallel to Peel Creek. Table 3.1 summarizes the characteristics of the Peel and Fork anticlines.

Table 3.1 Characteristics of F₁ folds.

Structure	Peel Anticline	Fork Anticline
Trend and plunge of axis	12→270	1→290
Approx. wavelength	>500 m	150 m
Tightness	Gentle	Gentle
Axial planar foliation	Well developed	Lacking
Rock units affected	Unit 1a (metaclastic)	Unit 1d (limestone)

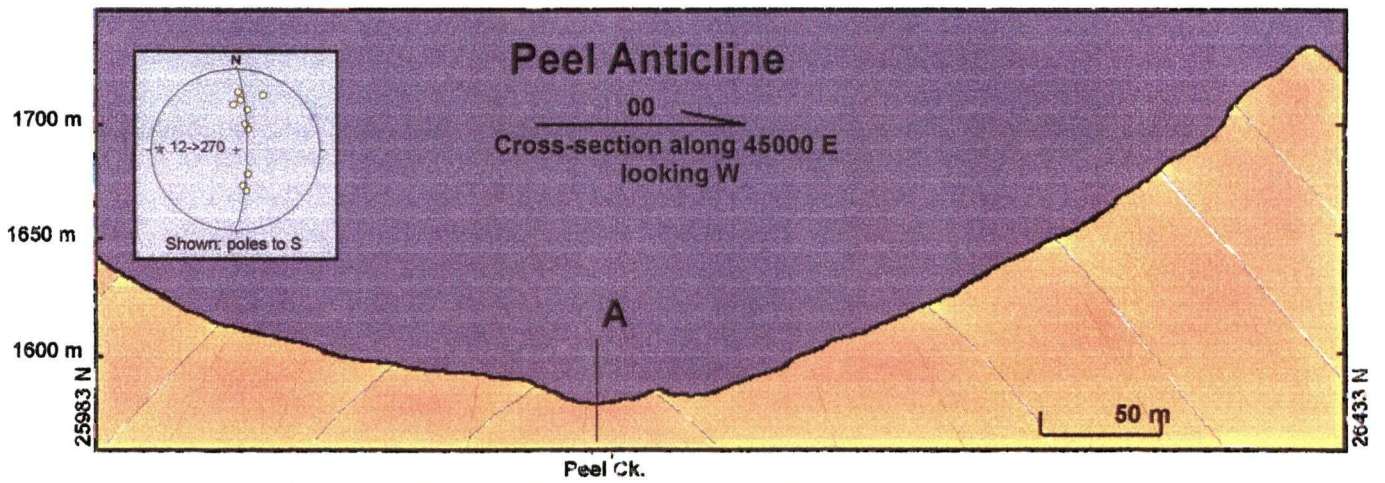


Figure 3.1. Peel Anticline (F_1) cross-section (A-A' on map) and stereoplot.

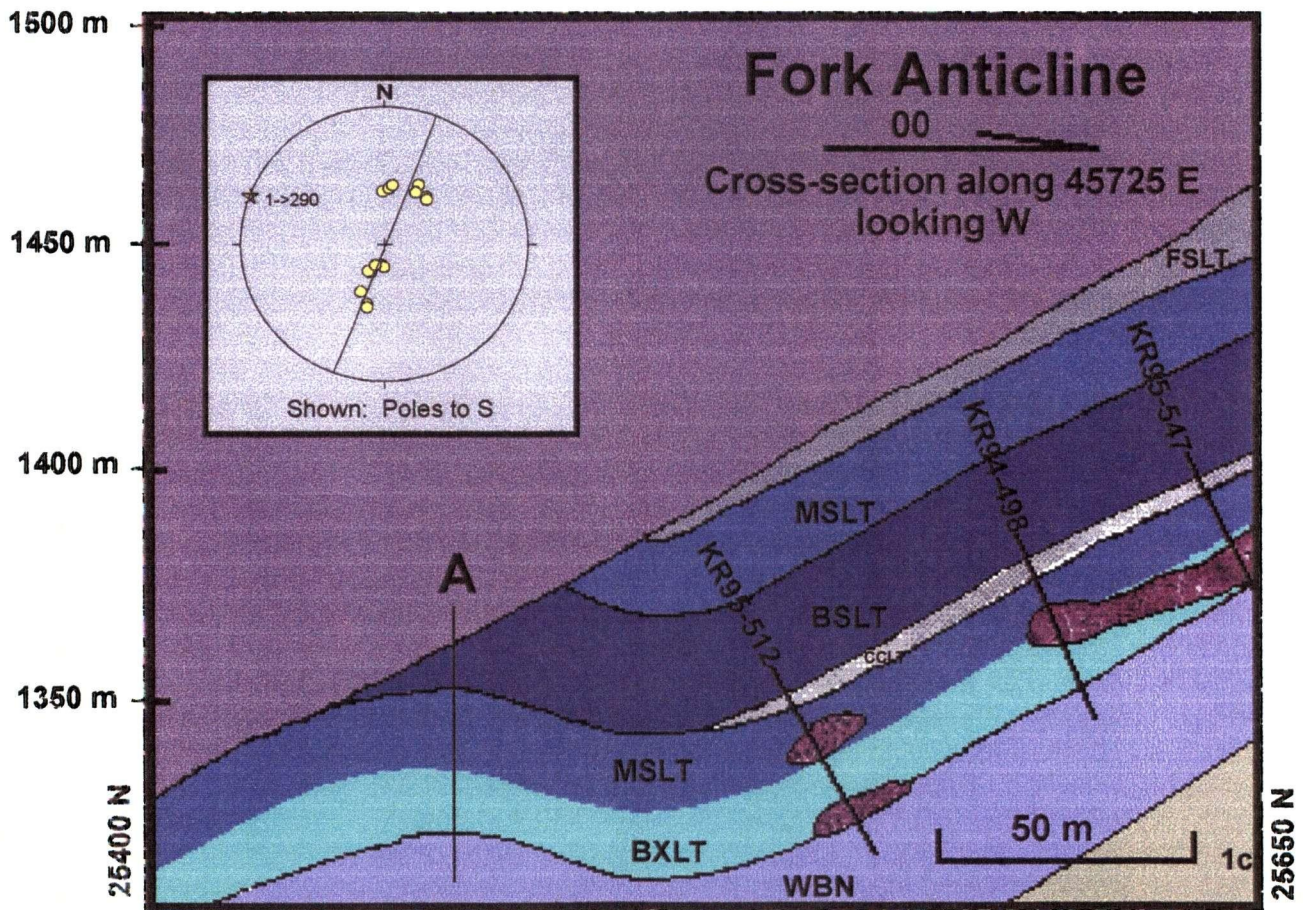


Figure 3.2. Fork Anticline (F_1) cross-section (B-B' on map) and stereoplot.

A well defined, steeply dipping to vertical axial-planar foliation (S_1) is conspicuous in meta-pelitic rocks of unit 1a. The E-W axis of the Peel Anticline differs from the generally NE trending regional first phase folds reported by Gordey (1981) and Mortensen (1982) elsewhere in the Pelly Mountains. This difference is likely a result of local variations of the stress field.

3.2 D_2 – Compressional, ductile deformation

A penetrative foliation (S_2) defined by unevenly spaced crenulation cleavage (plate 3.4) is the most ubiquitous feature produced by the second deformation event. Other structures and features formed during D_2 include: stylolites developed in limestones (plate 3.5), shear joints (figure 3.7), a-c joints (figure 3.8, plate 3.8), concentration of carbonate minerals along F_2 intrafolial hinges, crystallization of chlorite zone greenschist facies minerals (muscovite and chlorite), and deformation of previously formed veins (plate 3.9).

Two large scale second phase folds (F_2) are prominent on the southern half of the map area, where they deform limestones of unit 1d. F_2 folds are characterized by moderately NE-dipping axial planes, and E-W- to WNW-trending axes. Table 3.2 summarizes the characteristics of the two large-scale second phase folds. The axes of F_2 and F_1 folds in the study area are approximately coincident. However, F_2 folds are distinguished on the basis of the gentle dip of their axial surfaces (as opposed to upright F_1 axial surfaces) and by crenulation of S_1 (axial planar to F_2) produced during D_2 . The Break-Ridge Syncline (Figure 3.3 and plate 3.1) is the largest second phase fold in the map area, and is the only fold that can be readily recognized by its map pattern. The interlimb angle of the Break-Ridge syncline increases to the east from close to open. The Hoodoo anticline (Figure 3.4) is a second phase fold within thrust and normal fault blocks in the SW portion of the map.

Small scale intrafolial folds (figures 3.5 and 3.6, plates 3.2 and 3.3) are common in the northern half of the map area, and are particularly well developed in pelitic beds of unit 1a. In the

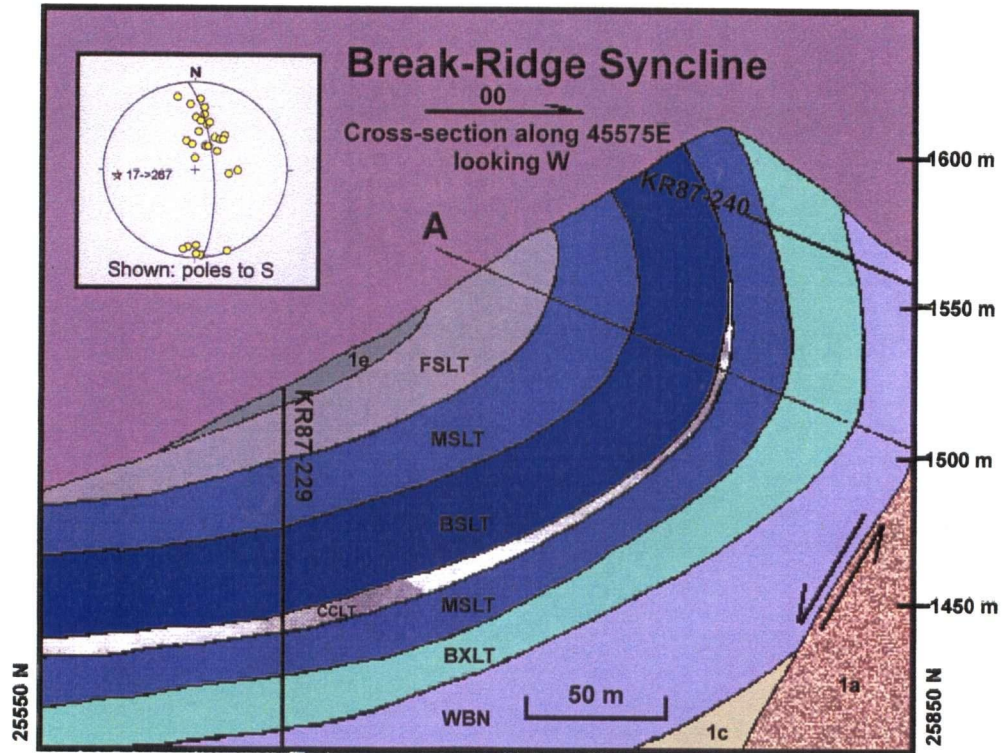


Figure 3.3. Break-Ridge cross-section (C-C' on map) and stereoplot.

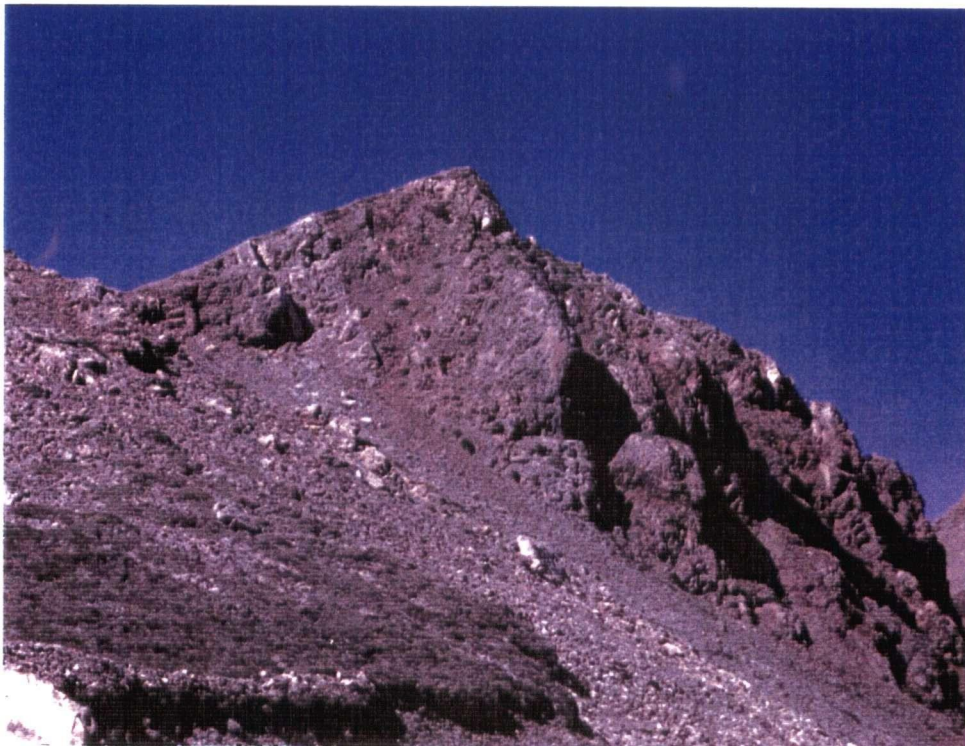


Plate 3.1. Vertical to overturned beds in the upper limb of Break-Ridge Syncline. Looking west. Field of view is approximately 120 m.

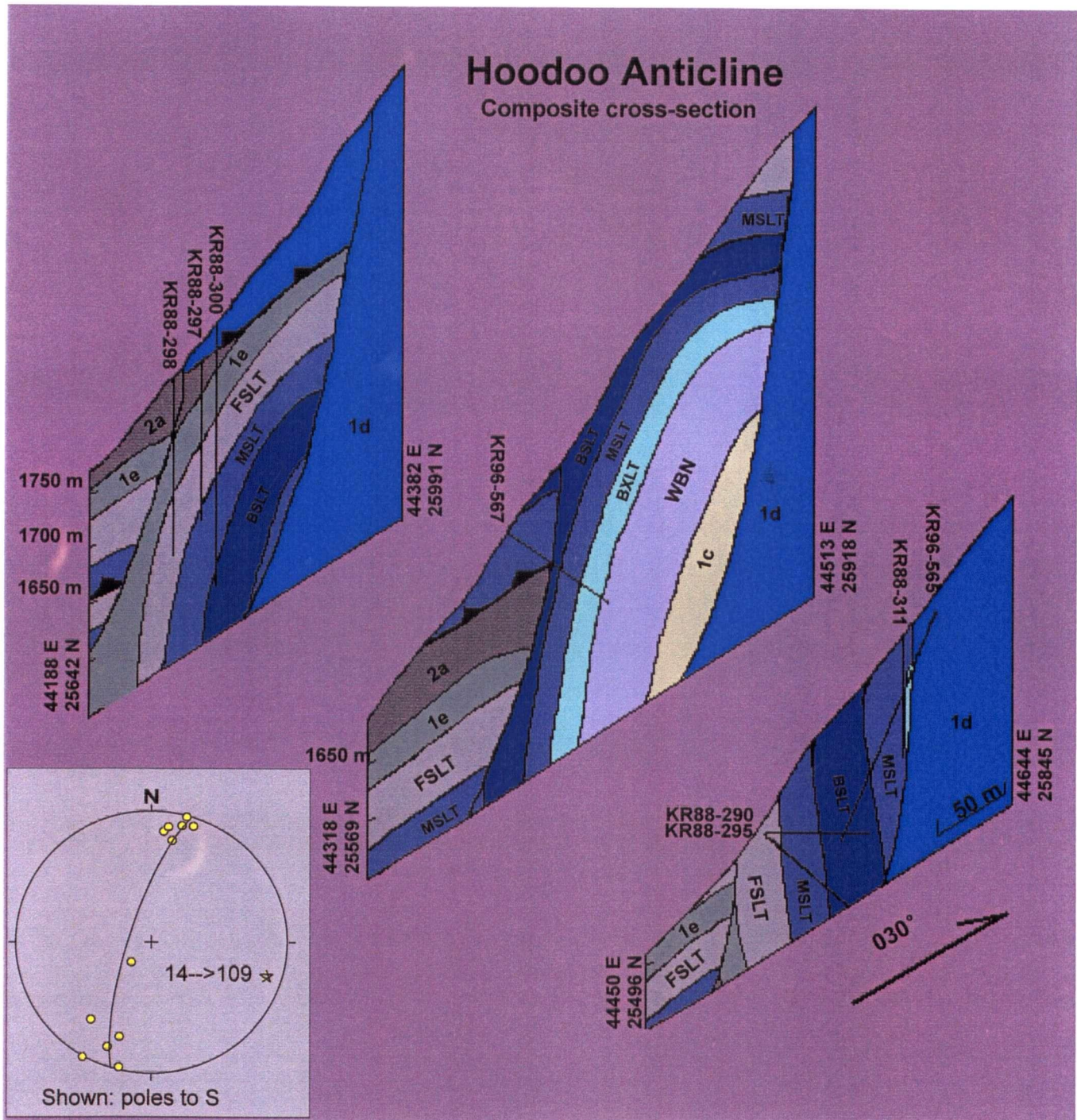


Figure 3.4. Composite cross-section and stereoplot of the Hoodoo Anticline. The anticline is cross-cut by younger thrust and normal faults. Cross-sections D1-D1', D2-D2', and D3-D3' on map.



Plate 3.2. Intrafolial folds in unit 1a argillite in the Gully zone. Looking east.

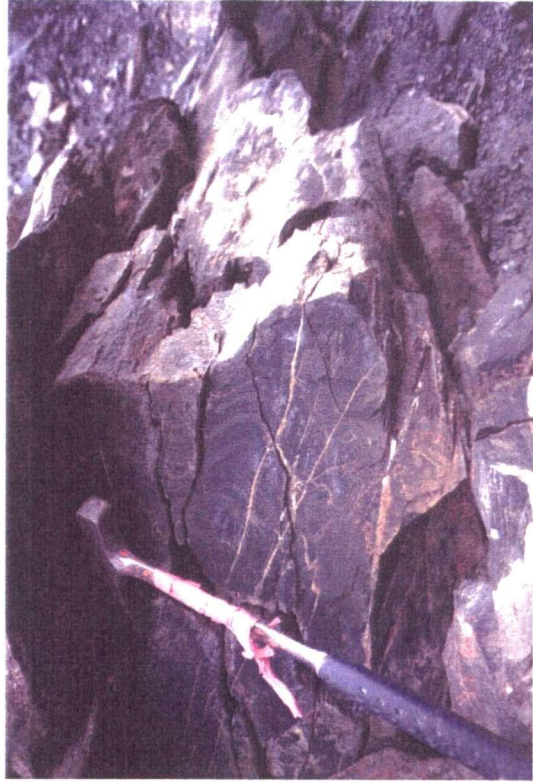


Plate 2.3. Intrafolial folds in unit 2a black limestone in the Knoll zone. Looking southwest.

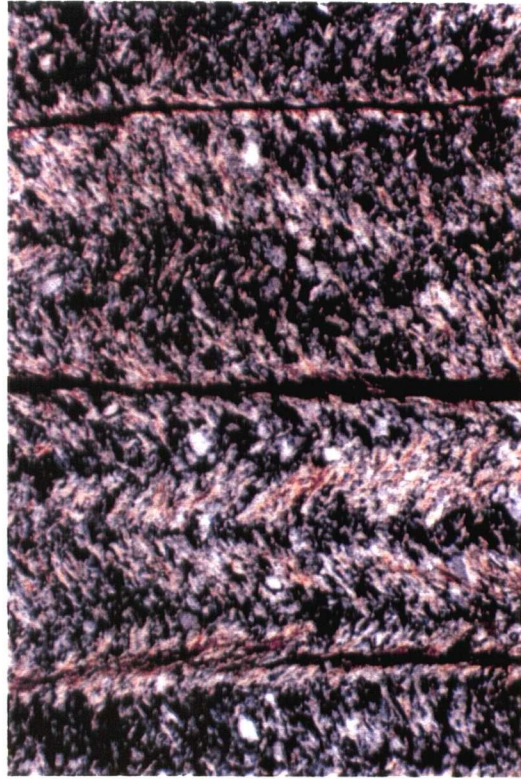


Plate 3.4. Photomicrograph showing spaced crenulation cleavage (S2) developed in unit 1a in the Shamrock Zone. Field of view = 1 mm

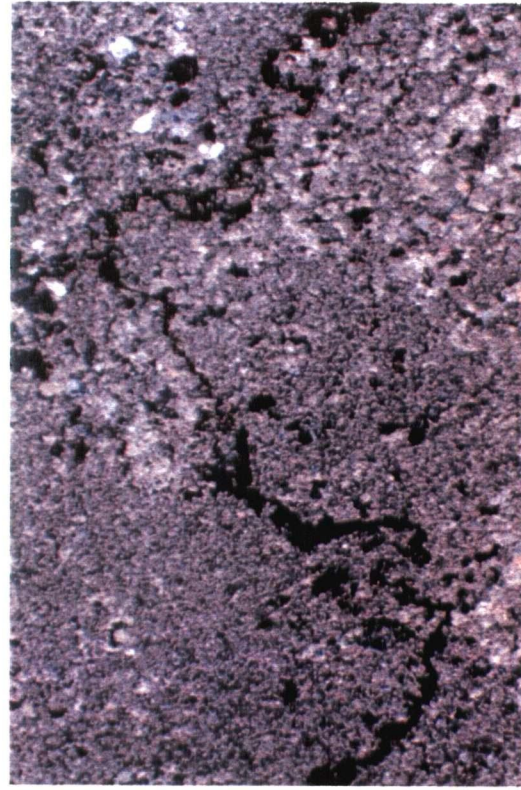


Plate 3.5. Photomicrograph showing stylolite developed in limestone (unit 1d). Field of view = 2 mm.

Shamrock zone, they form shallowly NE-dipping asymmetric "S" folds along the eastern limb of the Peel anticline. The pronounced SE vergence of intrafolial folds indicates that they are F_2 structures, and are not parasitic to the Peel anticline.

A well developed, NNE-dipping axial-planar foliation (S_2) is developed in pelitic lithologies. S_2 is an unevenly spaced crenulation cleavage defined by the segregation of muscovite and chlorite (M-domains) from quartz (Q-domains) and lithon structures defining S_1 foliation. S_2 is parallel to axial planes of D_2 folds.

Table 3.2 Characteristics of F_2 folds.

Structure	Break-Ridge syncline	Hoodoo anticline	Intrafolial folds
Orientation of axis	17→267	14→109	11→313
Wavelength	>400 m	>200 m	25-70 cm
Amplitude	>500 m	>140 m	5-20 cm
Tightness	Close (50° to 72° i.a.)	Close (approx. 60° i.a.)	Open(70° avg.i.a.)
Vergence	SSW	SSW	SSW
Foliation	Poorly developed	Poorly developed	Well developed
Rock units affected	Unit 1d (limestone)	Unit 1d (limestone)	Unit 1a (metaclastic)

On the area immediately to the north and west of the Ketz River deposit, second phase folds have NW-trending axes and fold (are younger than) regional thrust surfaces (Mortensen, 1982). Farther south, in the Indigo Lake area, a single event that produced NW-trending folds and NNE-directed thrusting of upper limbs was mapped by Gordey (1981). In the Ketz River area, large second-phase folds have E-W axes, and are cross-cut by (predate) thrusts (see later discussion). Smaller, S-verging intrafolial folds have NW-trending axes. F_2 axial trends varying from E-W (in large folds) to NW (in small folds) are interpreted to result from non-coaxial deformation.



Plate 3.6. Different lithologies within unit 1a develop foliations differently. The pelitic layer (below) has tight intrafolial folds, with S_1 nearly parallel to S_2 . Looking south.



Plate 3.8. A-c joints filled by later veins in the Gully Zone. Field of view is approximately 3.5 m. Looking northeast.



Plate 3.7. Outcrop of unit 1a with S_1 (bottom left to upper right), S_2 (subvertical, slightly folded), and S_3 (upper left to lower right). Looking west.

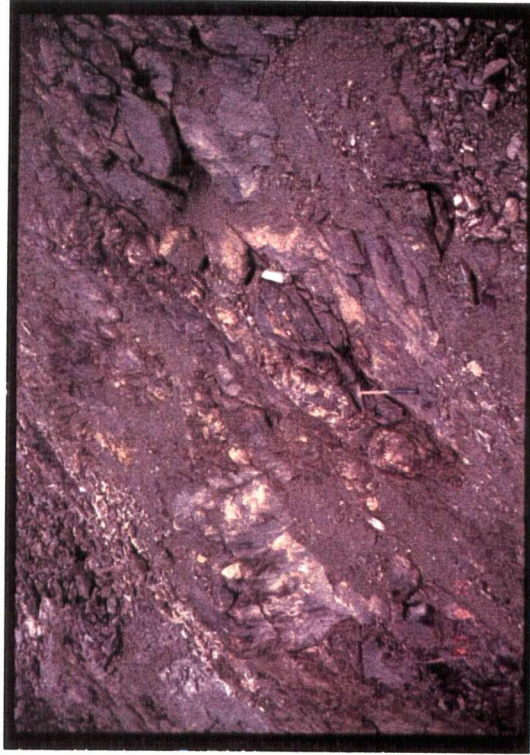


Plate 3.9. Older vein in the lower Shamrock Zone, boudinaged during D_1 . Looking northwest.

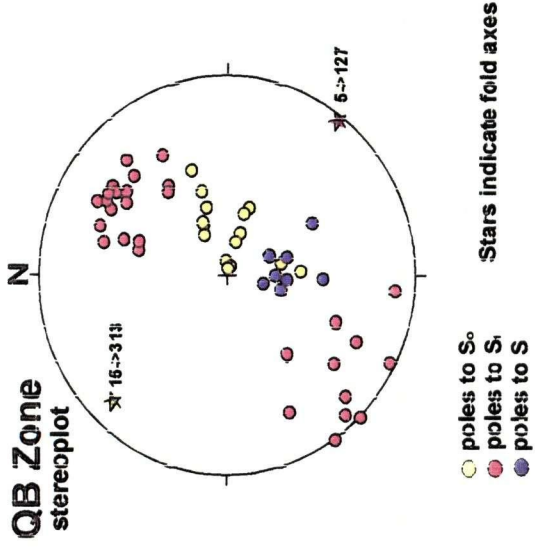


Figure 3.5. Lower hemisphere stereonet of small scale second phase intrafolial folds in the Gully zone.

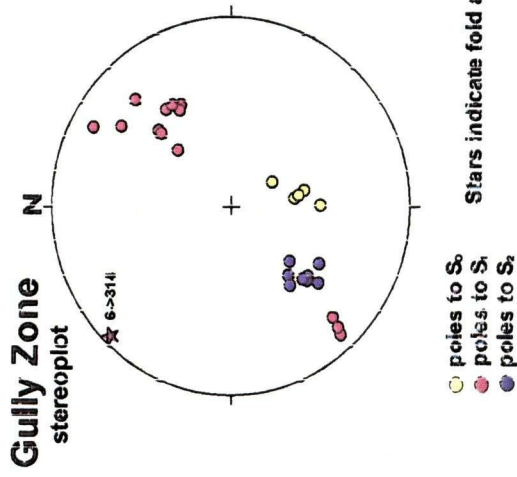


Figure 3.6. Lower hemisphere stereonet of small scale second phase intrafolial folds in the QB zone.

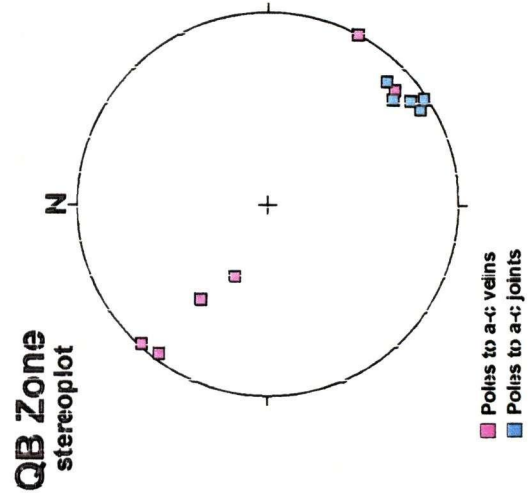


Figure 3.7. Lower hemisphere stereonet of shear joints on the Break-Ridge syncline.

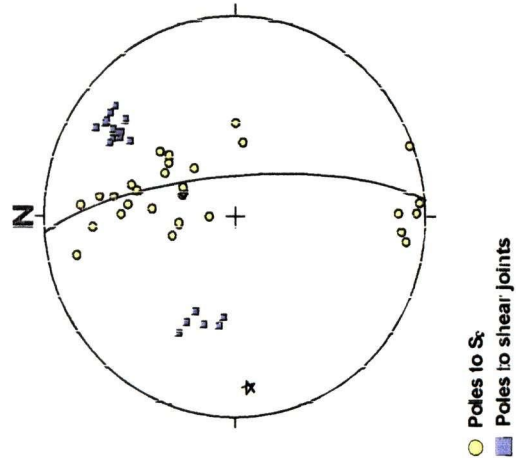


Figure 3.8. Lower hemisphere stereonet of a-c joints in the QB zone.

3.3 Faults

3.3.1 Thrusts

The third deformation event recognized in the area is characterized by imbricate thrust faulting. Rock units involved in thrusting (units 1a through 2a) young to the southwest, and thrust surfaces in the map area dip shallowly to the south. Immediately southwest of the map area, well exposed thrust surfaces (Plate 3.10) have pronounced NNE vergence.

The unexposed contact between units 1a and 1d at the south-central part of the map area (Figure 3.9) involves over 850 m of reverse displacement, and over 350 m of stratigraphic throw. In that area, rocks of unit 1a structurally overlie folded (F_2) rocks of units 1d and 1e, and the thrust fault cross-cuts the upper hinge of the Break-Ridge Syncline (F_2). Drill core correlations show that the fault plane is oriented at 100/18 (right hand rule). Farther to the west, three other thrust panels are dismembered by later, strike-slip and normal faults (Figure 3.11).

D_3 thrusts mapped in the Ketzka River area are interpreted to represent small scale equivalents of the N-directed thrusts described by Mortensen (1982) and Gordey (1981) in other areas of the Pelly Mountains. In the Ketzka River area however, thrusts are younger than and have opposite vergence to second phase folds, whereas elsewhere in the Pelly Mountains the thrust faults are folded and have the same vergence as folds. It is therefore uncertain whether two separate thrust faulting episodes occurred in the Pelly Mountains.

Local crenulation of S_2 was observed on the N-facing slope of the Shamrock zone. This fabric may be related to the first thrusting event.

3.3.2 Normal faults

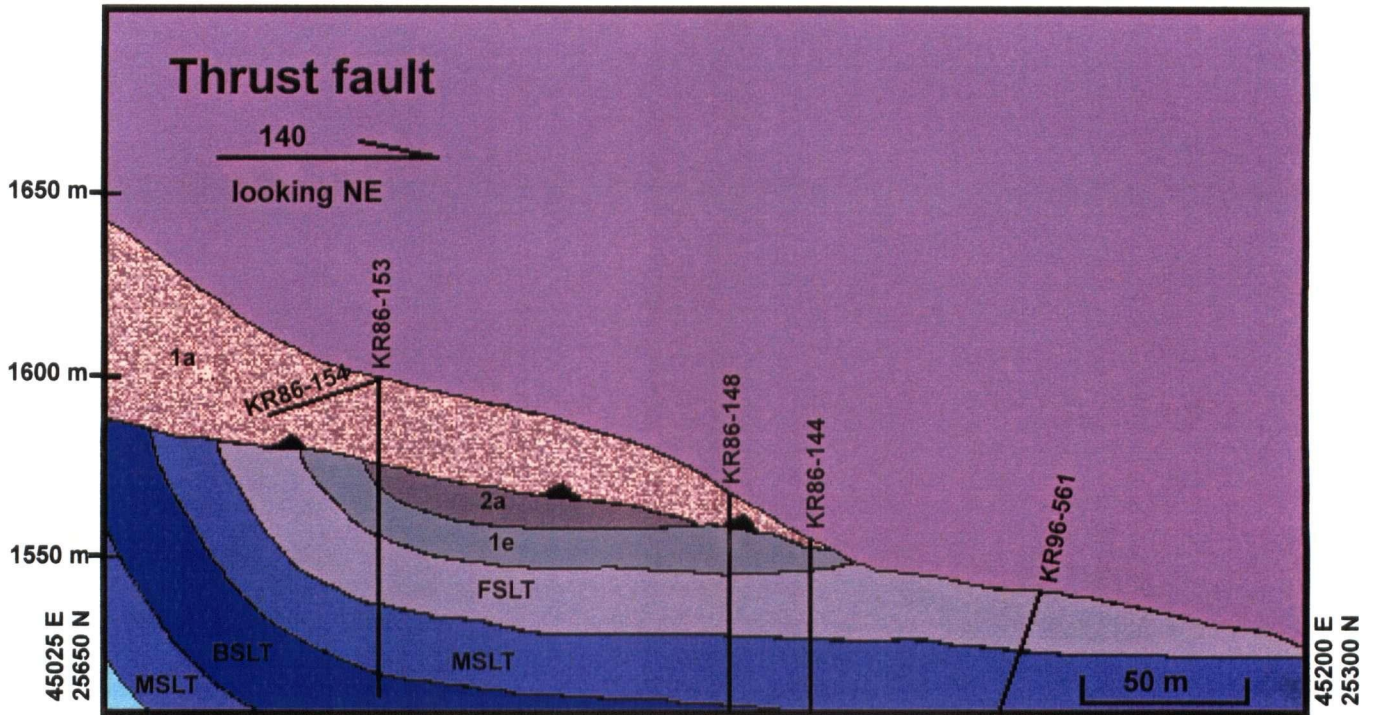


Figure 3.9. Cross-section E-E', showing a thrust fault cross-cutting a second phase fold.



Plate 3.10. Thrust faults with NNE-directed movement are exposed immediately outside the map area. Looking west.

The Peel Fault (Figure 3.13) divides the map area into two stratigraphic domains. The hanging-wall of the Peel Fault (southern part of the map area) consists of units 1d and younger rocks, whereas the footwall consists almost exclusively of rocks of unit 1a. The attitude of the Peel Fault is 067/74. Minimum normal displacement and stratigraphic throw on the Peel Fault are in the order of 200 m as measured from drill hole stratigraphic correlations. The westernmost portion of the Peel Fault is exposed on surface, and is displaced by younger listric normal faults, whereas the eastern two-thirds of the Peel Fault is concealed by a younger reverse fault. The Peel Fault cross-cuts the Break-Ridge Syncline. Mining cuts in the Ridge Pit (plate 3.15) expose brecciated limestone in the hanging wall of the Peel Fault.

The Cathedral syncline (Figure 3.10) is not a true flexural fold; rather it is a fault anticline, produced by juxtaposition of N-dipping beds on the 1a thrust sheet with S-dipping beds of the southern limb of the Peel anticline.

Subsequent to the development of the Peel Fault, normal faulting divided the study area into four structural domains (Figure 3.11 and plate 3.12). From west to east these include: Western Graben, Central Horst, Eastern Graben, and easternmost normal fault blocks.

The Western Graben structure occupies the southwestern portion of the map area. It is characterized by high angle listric normal faults that accommodated a cumulative offset of 15 to 35 m of vertical displacement, and up to 110 m lateral (predominantly sinistral) displacement. Separation between listric faults (or width of the individual fault blocks) varies from 35 to >150 m. The trend of the listric faults is 330° to 350°. Normal faults forming the Western Graben dismember D₃ thrusts.

The Central Horst is the area between the two graben structures. It is not the most uplifted block. In the southern portion of the map area, the Central Horst exposes the oldest thrust in the map

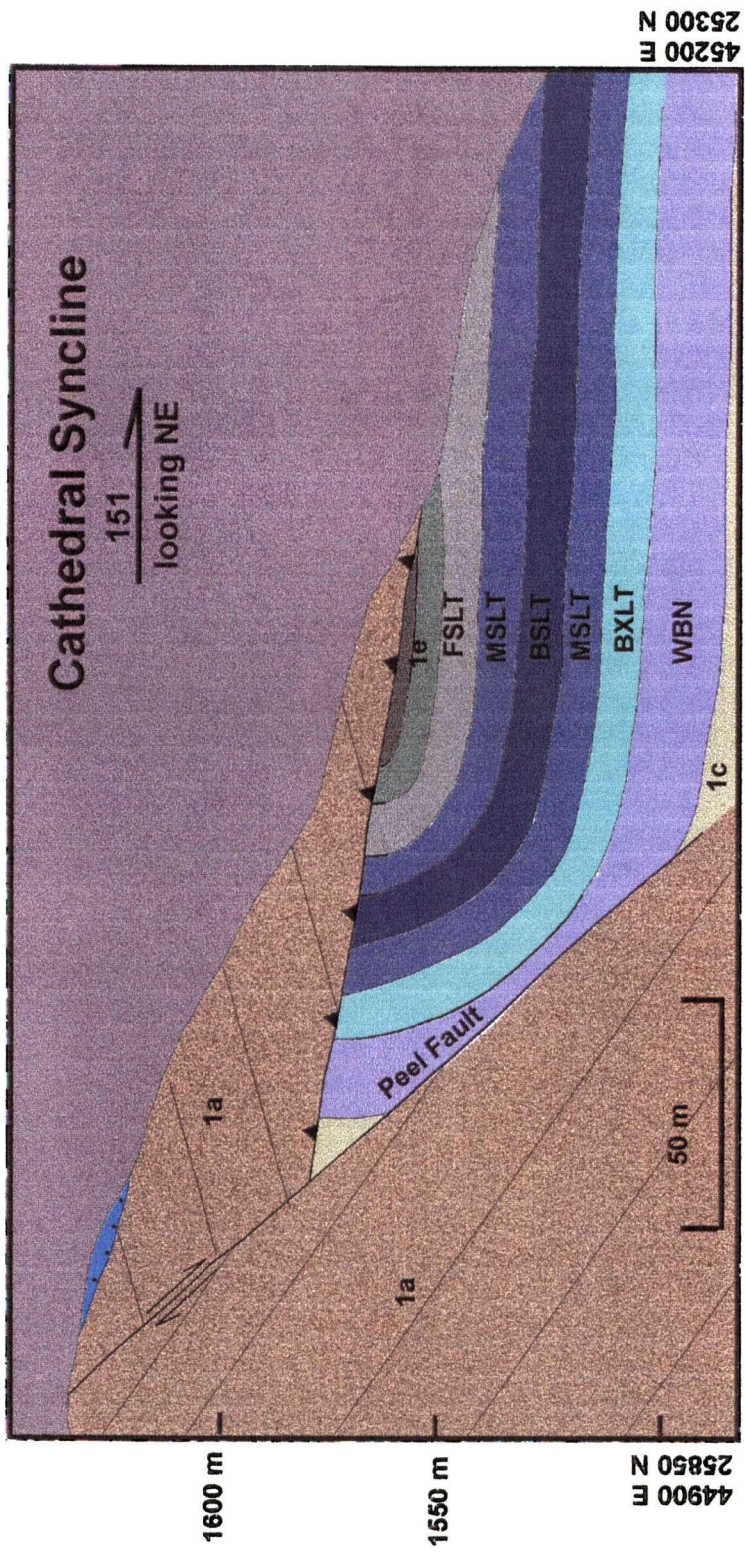


Figure 3.10. Cross-section F-F' showing cross-cutting relationships between the Break-Ridge Syncline (F), a NNE-directed thrust, the Peel Fault, and a NNW-trending normal fault.

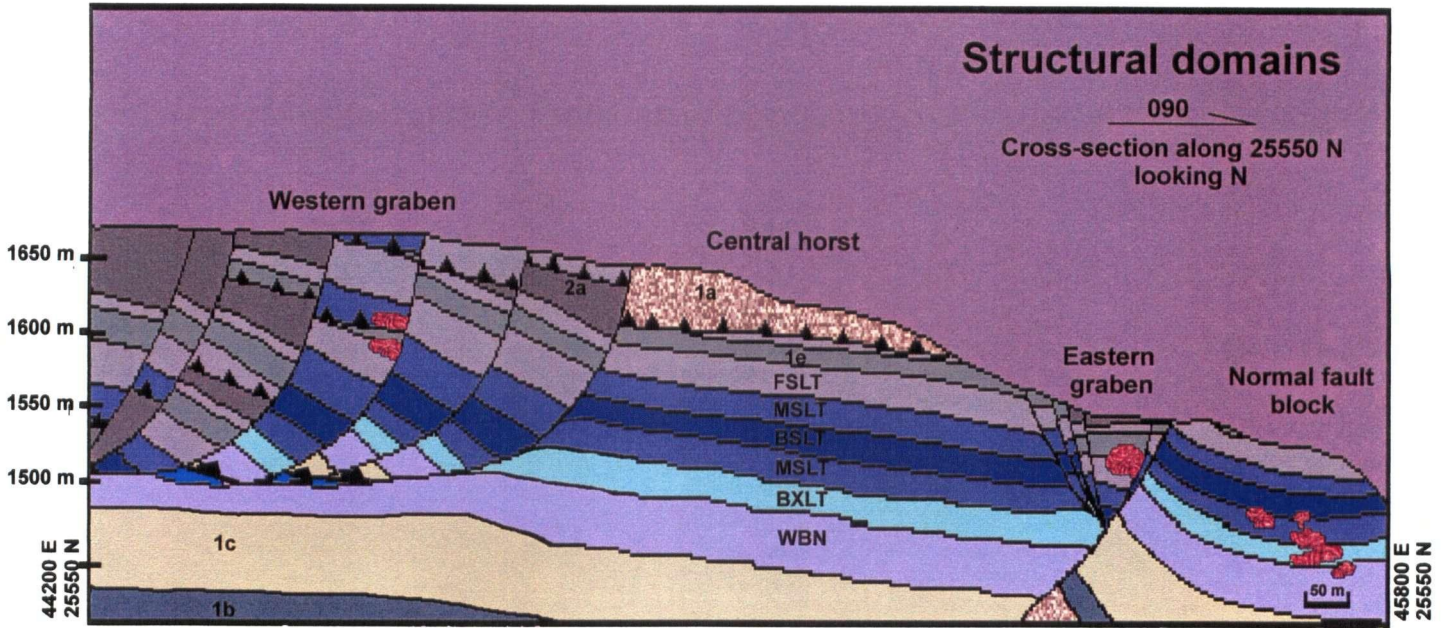


Figure 3.11. E-W cross-section (G-G') along the southern part of the map, showing the structural domains produced by normal faulting.

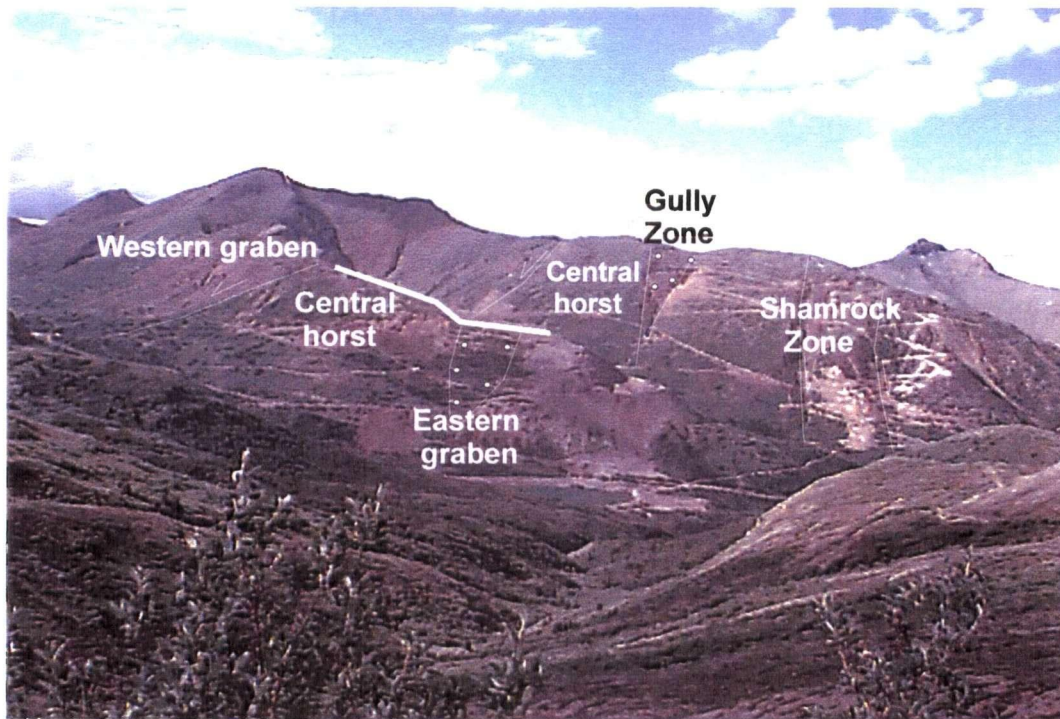


Plate 3.11. Topographic expression of the structural domains defined by normal faults. Looking north.

area (Figure 3.11), revealing the cross-cutting relationship between second phase folds and NNE-directed thrusts.

The Eastern Graben extends from the Ketzá manto zones (south) to the Shamrock (north) zones. It is characterized by high-angle, nearly planar bounding faults. The Gully zone (plate 3.12) is a topographic expression of the eastern graben. In the southernmost portion of the map area, the Eastern Graben downdrops rocks of units 2a and 1e into direct fault contact with rocks of unit 1d, and rocks of units 1b and 1c into direct fault contact with unit 1a. Vertical displacement along the graben-forming faults varies from 2 to 35 m, and minimum lateral displacement is 20 m. Widths of fault blocks vary from 15 to 90 m. The general axis of the graben trends 188° .

The NE part of the map is characterized by a series of high angle, planar normal faults. The amount of down-drop increases towards NE. Widths of fault blocks are 25 to 700 m. The general trend of the faults is 355° . Only the western-most fault block is exposed in the hangingwall of Peel Fault. This is the most uplifted block, and forms the centre of uplift. Three other fault blocks are exposed on the footwall of the Peel fault (Shamrock Zone). The easternmost of the fault blocks hosts oxidized mantos (Knoll Zone) in unit 2a limestone. Estimated downdrop along the Knoll fault is over 700 m.

The 1510 adit anticline (plate 3.13) is a large scale drag fold on the footwall of the Eastern Graben. The $9 \rightarrow 129$ axis of the 1510 adit anticline coincides with the axis of the graben, and with the normal faults in the Shamrock zone. A conspicuous set of calcite veins in extensional joints b-c-parallel to the drag anticline leads into, but does not cross-cut a massive sulphide orebody at the 1510 adit portal (plate 3.12).

The lack of regionally developed equivalents and the intimate relation between the apparent concentration of normal faults and mineralization in the Ketzá River area suggests that the normal faulting event represents uplift (along Peel Fault and NNW-trending faults) and collapse

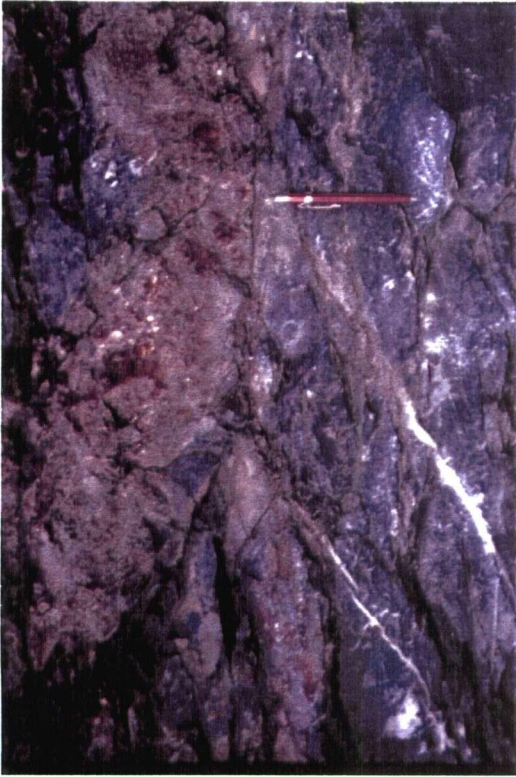


Plate 3.12. Massive sulphide along b-c-parallel calcite veins that lead into a mantle style orebody.

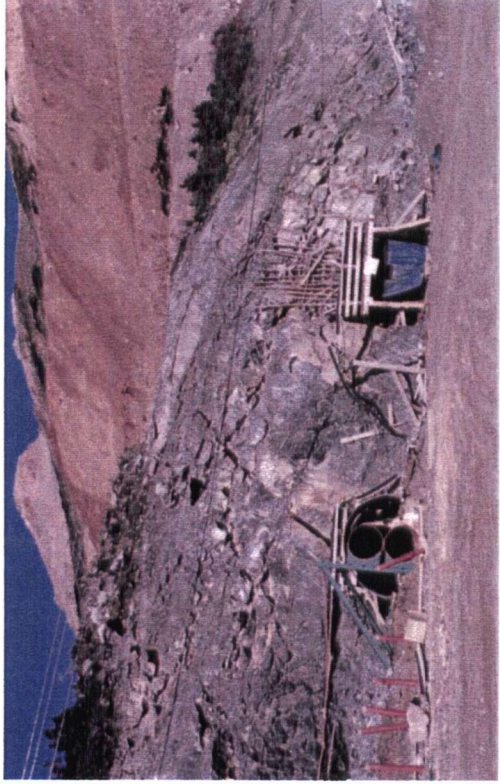


Plate 3.13. The 1510 anticline is a drag fold developed on the western footwall of the Eastern Graben. Calcite veins are a-c-parallel. Looking northwest.

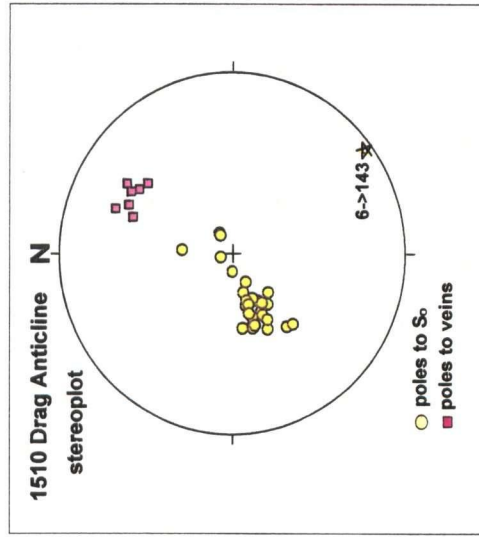


Figure 3.12. Lower hemisphere stereonet of the 1510 anticline and b-c-parallel calcite veins.

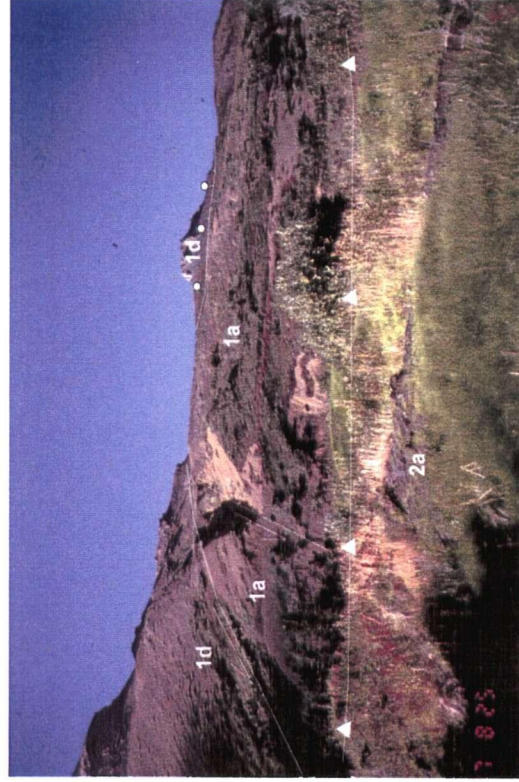


Plate 3.14. Structural complications produced by superimposed thrusting and normal faulting. Looking northwest.

(Central Graben) in response to the emplacement of a buried intrusion, as suggested by Abbott (1986).

3.3.3 Thrust

The latest structure recognized in the study area is a high angle, S-verging reverse fault that cross-cuts the Eastern portion of the Peel fault (Figure 3.13). The orientation of the reverse fault plane is 244/30. Movement along the fault was SE-directed, but total displacement cannot be quantified because marker beds are lacking on surface, and drill hole control is limited. No regional equivalent of this structure is reported.

3.4 Discussion

Two main folding events, followed by three episodes of faulting, affected the Ketzka River area. Cross-cutting relationships indicate the sequence in which the deformation events occurred. There are no absolute age constraints for deformation in the Ketzka River area thus far, or more regionally throughout the Pelly Mountains. Within the context of the Northern Canadian Cordillera, it is reasonable to assume that all, or most of the deformation took place from Jurassic to mid Cretaceous time. In spite of the proximity to the Tintina strike-slip fault system, none of the structures observed in the Ketzka River area appear to be related to the Tintina system.

F₁, F₂, and the first thrust events can be interpreted as progressive deformation events in the predominantly contractional regime that characterized the western North American margin during the Mesozoic. In the Ketzka River area, second phase folds have SSW vergence, which is opposite to that of the thrusts (third deformation event). Elsewhere in the Pelly Mountains, upright and N-verging folds are mapped. Gordey (1981) mapped a single event of N-verging folds and thrusts in the Indigo Lake area, approximately 60 km SW of the Ketzka River area. Mortensen (1982) mapped approximately 500 km² of an area of predominantly Upper Devonian

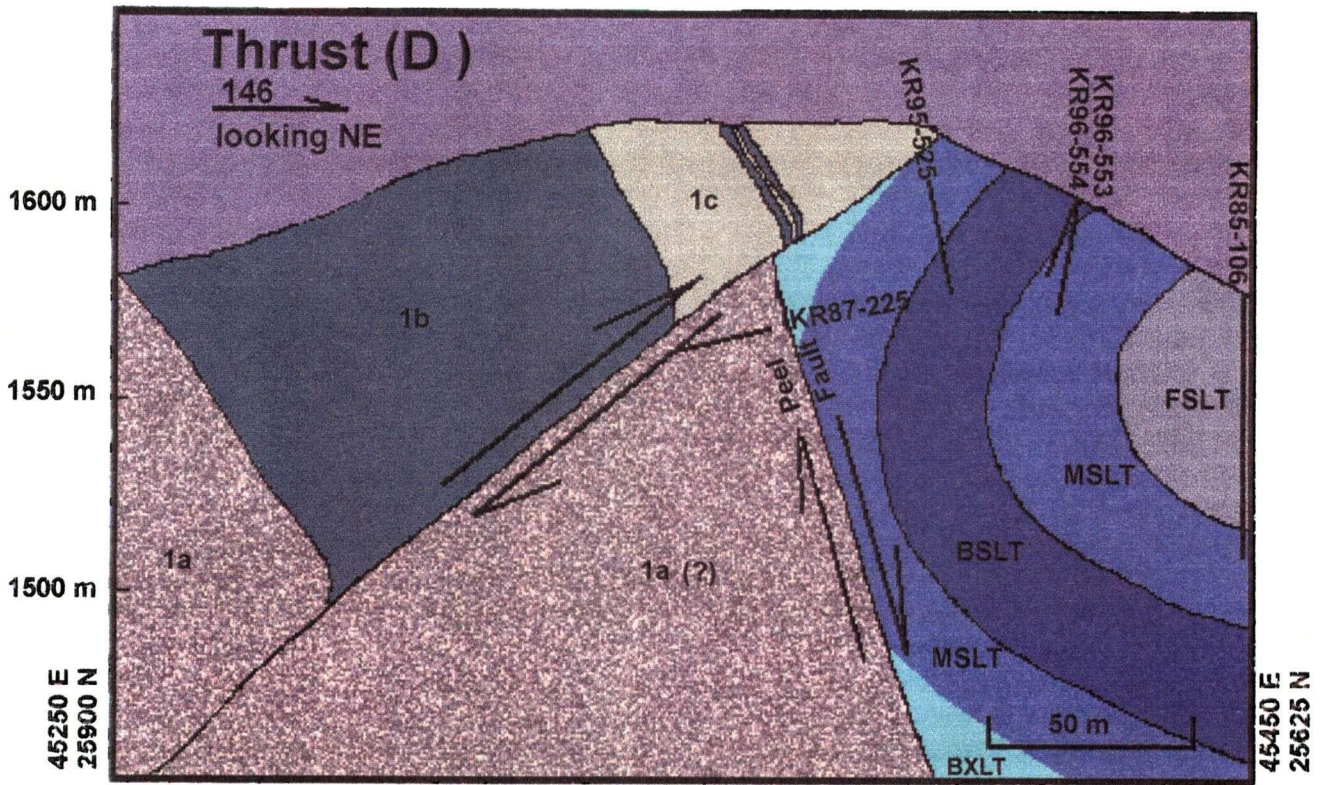


Figure 3.13. X-section showing D5 thrust fault concealing the Peel Fault (D4).

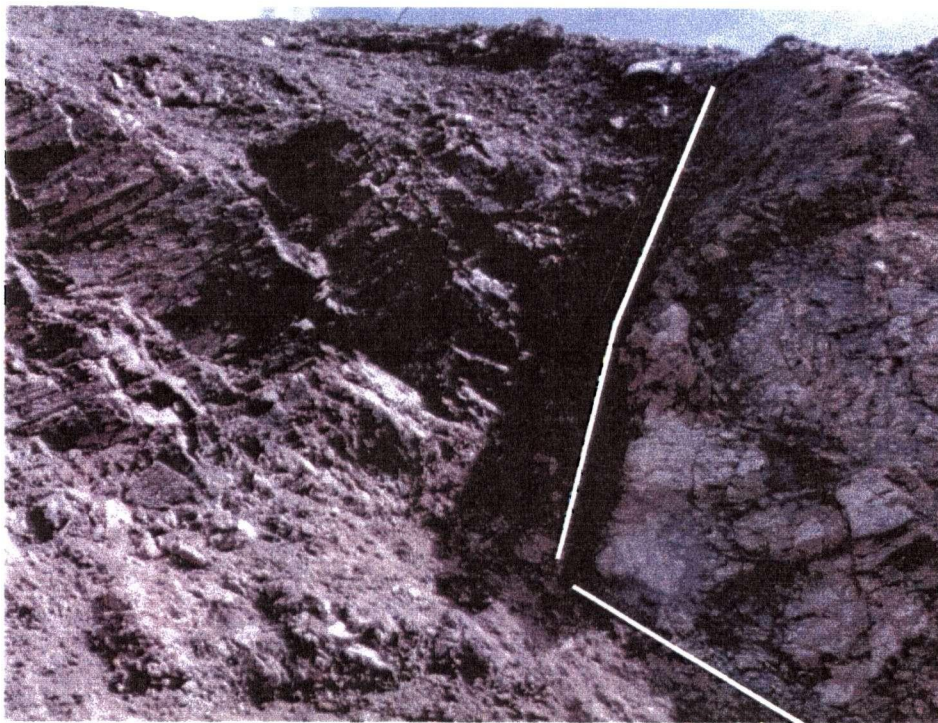


Plate 3.15. Mining cuts in the Ridge Pit expose the relationship between the D5 thrust and the Peel Fault. Field of view = approximately 12 m.

and Mississippian rocks in the central Pelly Mountains, and discerned two prominent phases of NW-trending folds. In the SW corner of his map area, thrust faults are folded along second phase axes. It is not clear if the opposite vergence of second phase folds and thrusts is a local feature, or if it is widespread but unmapped elsewhere in the Pelly Mountains. Folding and thrusting in the Pelly Mountains cannot be directly correlated with collisional events in the western North American margin.

The last two faulting events appear to be only locally developed. The geometry produced by normal faulting suggests doming and fracturing possibly as a result of emplacement of a buried pluton. In this scenario, listric normal faults and rotation of fault blocks in the Western graben and more planar faults of the Eastern Graben accommodated doming outside the areas of greatest uplift. Plutonic rocks of the 108 to 112 Ma Cassiar Suite that straddle the Ketz River area probably core the Ketz uplift. This is supported by an $^{40}\text{Ar}/^{39}\text{Ar}$ age from micas in a vein emplaced along a steeply dipping normal fault (see later discussion).

The latest thrust fault developed in the Ketz River area is a small-scale structure that may have resulted from local stresses. It cross-cuts the Peel Fault and mineralization in the Break Zone, and thus must be younger, and possibly unrelated to the first three compressional deformation events.

4 MINERALIZATION AND ALTERATION

4.1 Mineralization styles in the Ketzá River area

A study of the macroscopic mineralogy and ore petrography of the Ketzá River ores was undertaken to compare and contrast the different styles of mineralization. The main goal of this study was to search for evidence supporting or precluding the hypothesis that the different mineralization styles are the product of a single hydrothermal event driven by Mesozoic plutonism. Similar opaque and gangue mineralogy in carbonate hosted mantos and Fe-silicate alteration zones, and in metasedimentary rock hosted quartz-sulphide veins suggests a genetic relation between the different mineralization styles, and submicroscopic bismuth in all ore types suggests that hydrothermal activity was triggered by the emplacement of a pluton.

Preliminary cathodoluminescence studies were undertaken to define a microscopic hydrothermal stratigraphy that could be used to define the extent of hydrothermal alteration, and possibly to predict proximity to ore. Even though a hydrothermal signature was identified in cathodoluminescence, the study was not pursued due to lack of appropriate instrumentation.

4.1.1 Carbonate-hosted manto style mineralization

Au-rich carbonate hosted manto style massive sulphide orebodies and their oxidized equivalents are the best explored mineralization style in the Ketzá River area. Average Au contents in oxidized mantos is 13 g/t (Stroshein, 1997). Manto style orebodies (plates 4.1 and 4.2) are preferentially hosted by three limestone host facies of unit 1d: BXL T, MSL T, and WBN. The location of mantos is controlled by high-angle planar and listric normal faults, fold hinges, and by the location of the three favourable facies. Dimensions of the largest orebodies are in the order of 20 m in width, 80-100 m in length, and 20-25 m in thickness. Tables 4.1 and 4.2 summarize size, textural characteristics, relative abundance, and paragenetic relationships between opaque

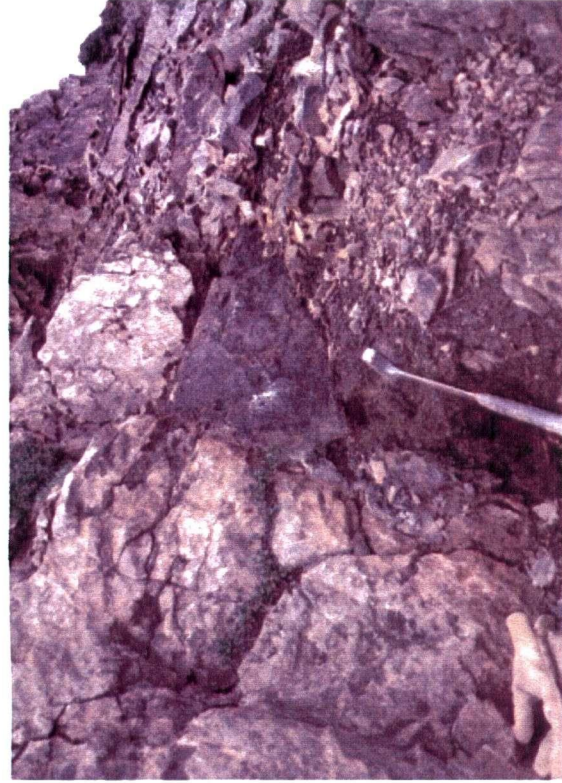


Plate 4.1. Small massive sulphide manto-style orebody in MSLT facies (unit 1d).



Plate 4.3. Fe-silicate alteration in core. Bladed texture is due to amphiboles. NQ core. Core diameter = 45 mm.

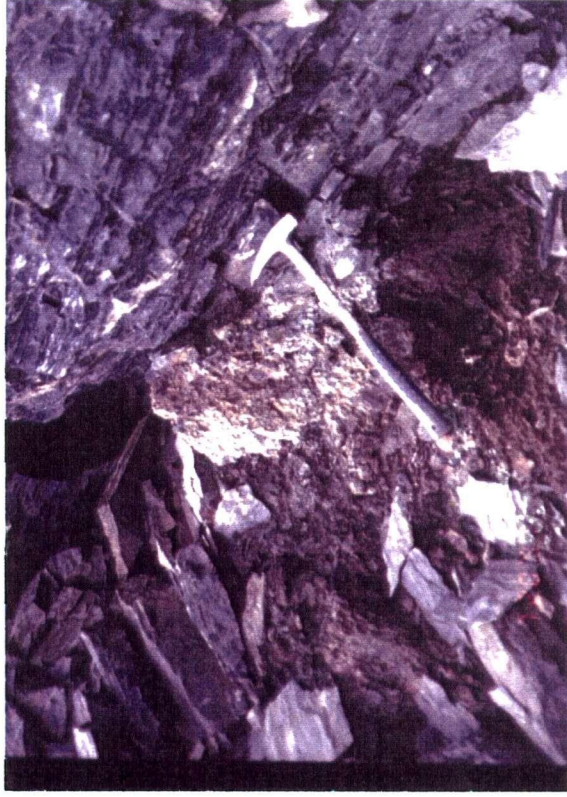


Plate 4.2. Small oxidized manto-style orebody in MSLT facies (unit 1d).



Plate 4.4. Oxide ore in core. HQ core. Core diameter = 61 mm.

and gangue minerals in the massive sulphide mantos. Principal sulphide mineralogy consists of pyrrhotite, pyrite, arsenopyrite, marcasite, and minor chalcopyrite. Galena and sphalerite are rare. Sulphide zones are invariably located beneath thrusts of the first fault generation. Oxidized mantos occur where thrust faults are completely eroded, allowing oxidized ground waters to reach the massive sulphide orebodies. Oxide mineralogy consists mainly of hematite and goethite (Appendix A). Distinctive Au-rich lustrous oxide aggregates have the field name "hissingerite". Massive sulphide zones include: Peel Sulphides, Peel East Sulphides, 1510 Portal, Lab, Bluff. Sulphide zones are invariably located beneath thrusts of the first fault generation. Oxide zones include: Peel Oxides, Break-Nu, McGiver, Chimney, Ridge, Fork, Deep, Hoodoo, and Knoll.

4.1.2 Au-rich Fe-silicate alteration

Au-bearing Fe-silicate alteration (plate 4.3), usually referred to as "skarn" by company geologists, is encountered mainly in the WBN and lower part of the BXLTL facies of unit 1d limestones, where it fringes the lower part of the Fork and Deep oxide zones (Figure 4.1). The major opaque mineralogy includes pyrrhotite, magnetite (plates 4.27, 4.28), pyrite, arsenopyrite, marcasite, and minor chalcopyrite. Gangue minerals include carbonates, Fe-amphibole (plates 4.37, 4.38), two generations of quartz, chlorite, and muscovite. Textures, relative timing of crystallization, and mineral proportions of opaque and gangue minerals are listed in table 4.3 and 4.2. XRD spectra of Fe-silicate minerals (Appendix B) match those of grunnerite-cumingtonite series amphiboles, but microprobe analyses are necessary for a conclusive identification of the amphibole species. The Fe-silicate alteration zones are interpreted to have formed by replacement of limestones that had a relatively high primary silt content. Locally, gold content in this ore type reaches 13 g/t.

4.1.3 Metasedimentary rock hosted quartz-sulphide veins

Quartz-sulphide veins and stockwork are ubiquitous in the Shamrock Zone, which is hosted within subunits LTG-PHYL, M-QZE₂, M-PHYL, M-QZE₁, and undivided unit 1a. Quartz-sulphide veins

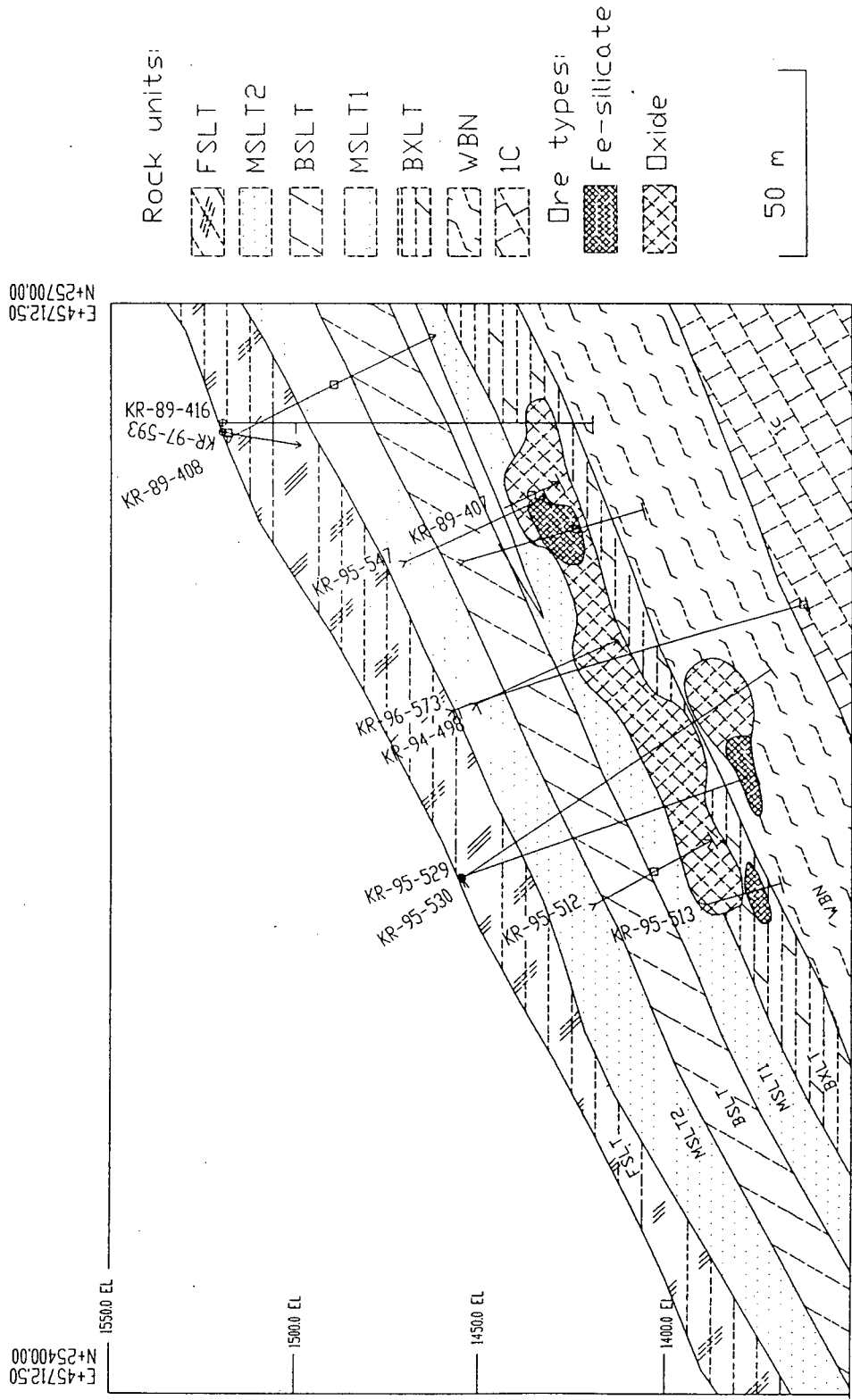


Figure 4.1. N-S Cross-section through the Fork and Deep zones, showing the location of Fe-silicate alteration with respect to oxidized mantos.

and massive sulphide veins typically occur within high-angle normal faults. Large quartz-arsenopyrite veins are the most conspicuous style of mineralization in the Shamrock Zone (plates 4.5 through 4.8), and may be up to 35 cm wide. Outcrops in the QB and 3M zones comprise brecciated milky quartz and scorodite. Gold content in these veins is generally <1 g/t. NNE-trending massive sulphide veins are found in the Gully Zone (plate 4.10) and in the E-W-trending Fred's Vein (map). Average gold contents in the Gully Zone is high (10 g/t), whereas samples from Fred's Vein yielded <1g/t Au. Quartz-sulphide stringer stockwork zones are present throughout the Shamrock zone and yield gold grades up to 7 g/t. Stringer stockwork zones are the main target of exploration for low grade, bulk minable gold mineralization in the area. Fred's Vein, and Lower Fred's Vein are Au-poor quartz-galena veins that parallel the E-W trend of the Peel Fault.

4.2 Mineralization styles outside the map area

Ag-rich galena-siderite veins at the Iona Silver Mine (approximately 7 km NE of the Ketz River area) are an important style of mineralization that were interpreted by Cathro (1992) as distal manifestations of the same hydrothermal system that produced the Ketz River deposit. Manto style mineralization in the Oxo Zone (approximately 5 km southeast of the Ketz River area) resembles the Ketz River mantos, but is Pb rich, and therefore distinct from the almost exclusively Fe-sulphide, low base metal content mineralization in the Ketz River ores.

4.3 Alteration

4.3.1 Dolomitization and decalcification

Dolomitization and decalcification of carbonate rocks (plates 4.14 through 4.18) are the only visible alteration effects associated with the manto-style mineralization. Dolomitization of ooids in MSLT facies or in oolitic lenses within other facies are good indicators of lateral proximity to ore. Weak to moderate dolomitization of ooid cores is common up to 5-7 m away from ore



Plate 4.5. Brecciated quartz veins.

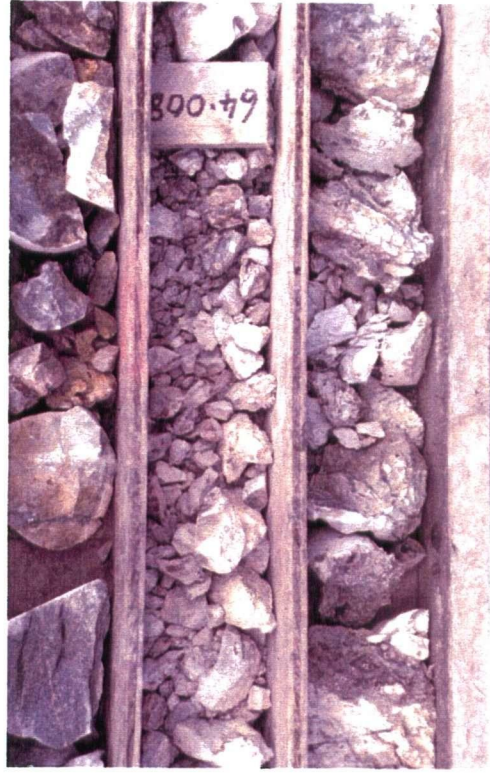


Plate 4.6. Brecciated quartz vein in core. HQ core. Core diameter = 61 mm.



Plate 4.7. Quartz-arsenopyrite vein hosted in metasedimentary rocks (unit 1a). HQ core. Core diameter = 61 mm.



Plate 4.8. Quartz-arsenopyrite vein along a syn-D2 a-c joint.



Plate 4.10. Massive sulphide boulders and quartz vein in the Gully Zone.



Plate 4.12. Mineralized quartz-sulphide vein in calcareous quartzite. HQ core. Core diameter = 61 mm.



Plate 4.9. Quartz-galena-pyrite vein. HQ core. Core diameter = 61 mm.



Plate 4.11. Au-bearing quartz-pyrite stringer stockwork hosted in M-PHYL (unit 1a). HQ core. Core diameter = 61 mm.

(laterally), and up to 2 m above or beneath ore, whereas intense decalcification is only observed immediately adjacent to ore. Removal of calcite and ankerite, and reprecipitation of iron in magnetite produce a dull orange-brown colour in the limestone. Plate 4.16 shows a sample with intense decalcification (oids are voids) and dolomitization.

A preliminary survey of hydrothermal effects in the alteration envelope around manto style ore was done using cathodoluminescence and SEM methods. Cathodoluminescence is the emission of visible light by a sample excited by a beam of electrons. In general, the emission process involves a transition from an excited state to a lower energy state. Typically, manganese is a cathodoluminescence activator, whereas iron is an inhibitor. Thus, dolomite is normally weakly luminescent, whereas calcite has variable luminescence.

Cathodoluminescence observations of ooids in weakly to pervasively altered MSLT samples resulted in the identification of three luminescence patterns: a) ooids with weakly luminescent dolomite surrounded by strongly luminescent intraclast calcite cement (plate 4.21); b) ooids formed by strongly luminescent calcite only (plate 4.23); c) weakly luminescent dolomitized ooids without intraclast calcite cement (plate 4.25). Plates 4.21, 4.23, and 4.25 show that the transmitted light microscopy is not appropriate to discern hydrothermal effects in MSLT, whereas cathodoluminescence patterns are more distinctive. SEM observations of the samples separated into the three cathodoluminescence patterns (plates 4.22 and 4.24) showed that weakly luminescent dolomite rhombs are overgrown by strongly luminescent calcite cement, and sub-microscopic magnetite occupies the interstitial space left by the calcite. Magnetite is also observed along fissures and veinlets (plate 4.26). Dolomitization and decalcification are typically early alteration stages that precede metal deposition. Dolomitization is accompanied by a volume decrease that enhances porosity. It is not clear if the precipitation of magnetite surrounding dolomite rhombs immediately followed the formation of dolomite, or it represents a late alteration effect, analogous to the retrograde reactions that are typical of skarn ores.



Plate 4.13. Dolomitized oolitic lens in FSLT facies.



Plate 4.14. Moderate dolomitization of ooids in MSLT HQ core.
Core diameter = 61 mm.

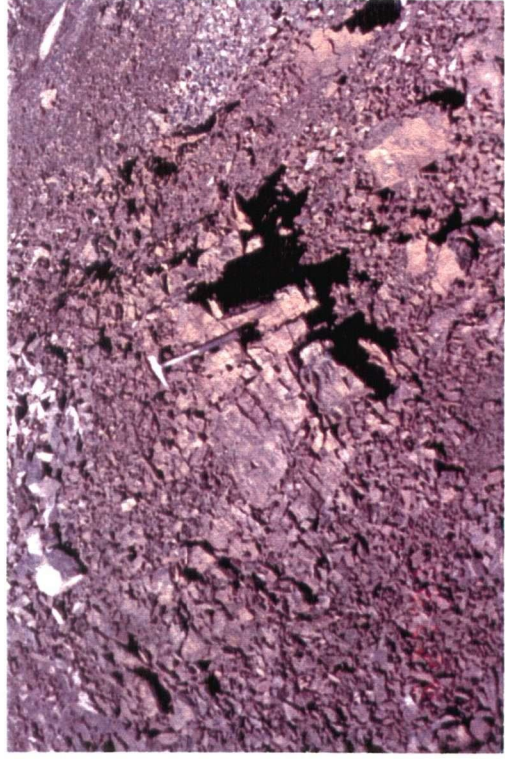


Plate 4.15. Strongly dolomitized MSLT outcrop.



Plate 4.16. Strong decalcification (porous core) and dolomitization.
HQ core. Core diameter = 61 mm.

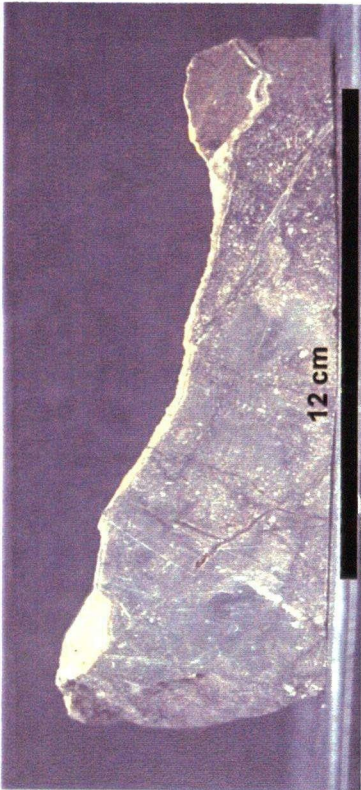


Plate 4.17. Moderate dolomitization in BXL.



Plate 4.18. Pervasive dolomitization and initial oxidation in MSLT. HQ core. Core diameter = 61 mm.



Plate 4.19. Bleaching of metasedimentary rock (unit 1a) next to quartz-sulphide vein.

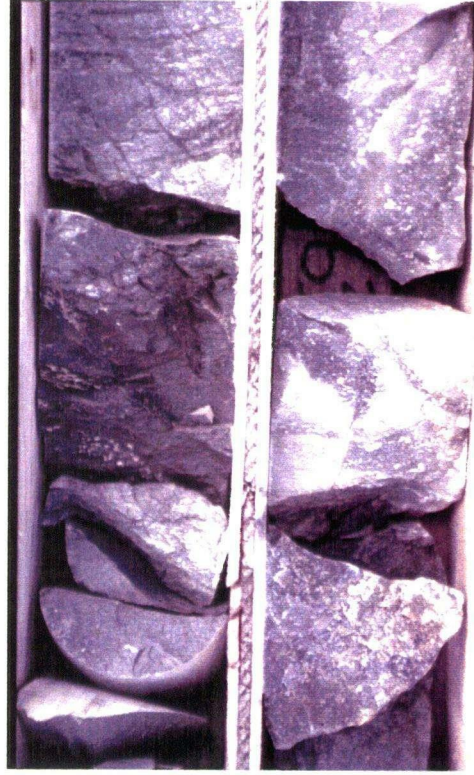


Plate 4.20. Silicified quartzite (unit 1a) hosting quartz-sulphide stringer stockwork.

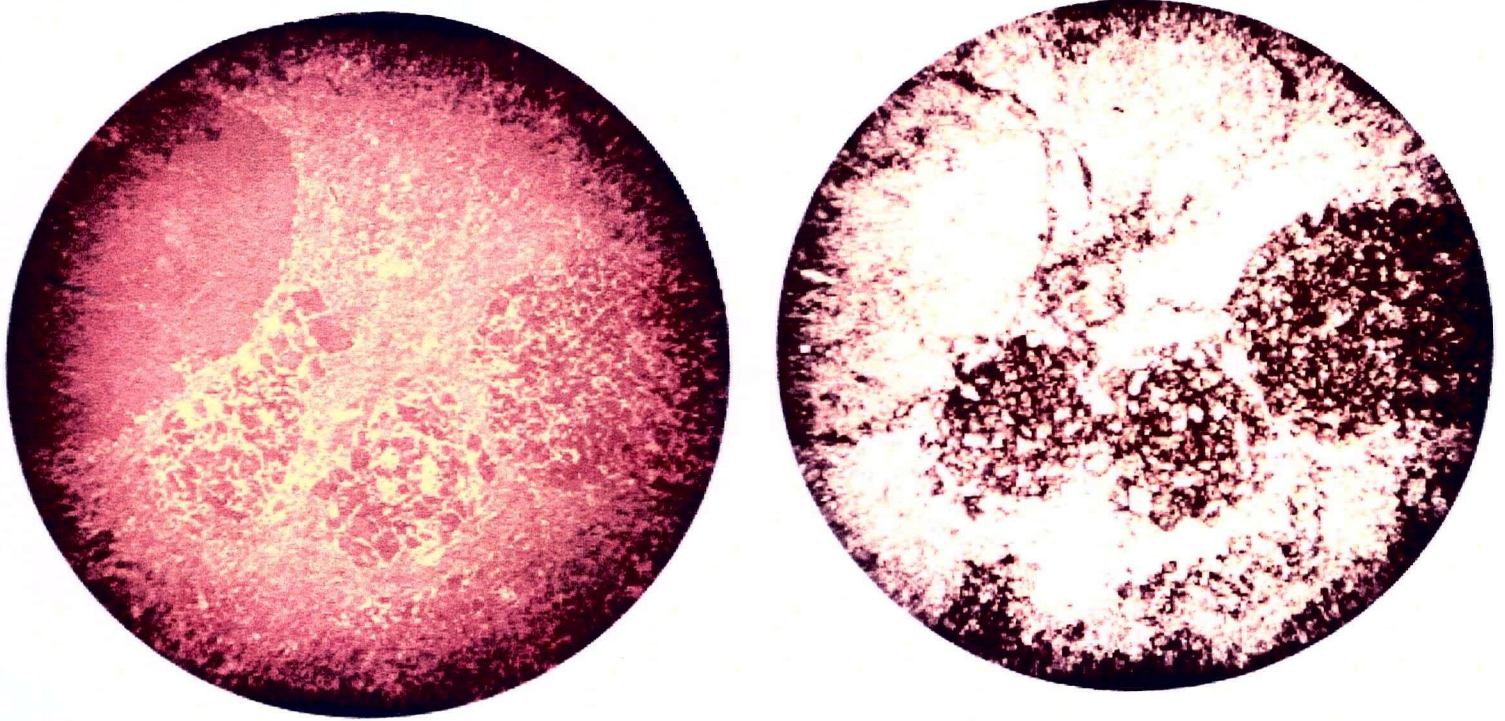


Plate 4.21. Cathodoluminescence signature of invisible hydrothermal dolomitization, characterized by strongly luminescent calcite surrounding dark dolomite rhombs.
 Left: cathodoluminescence; Right: transmitted plane polarized light.

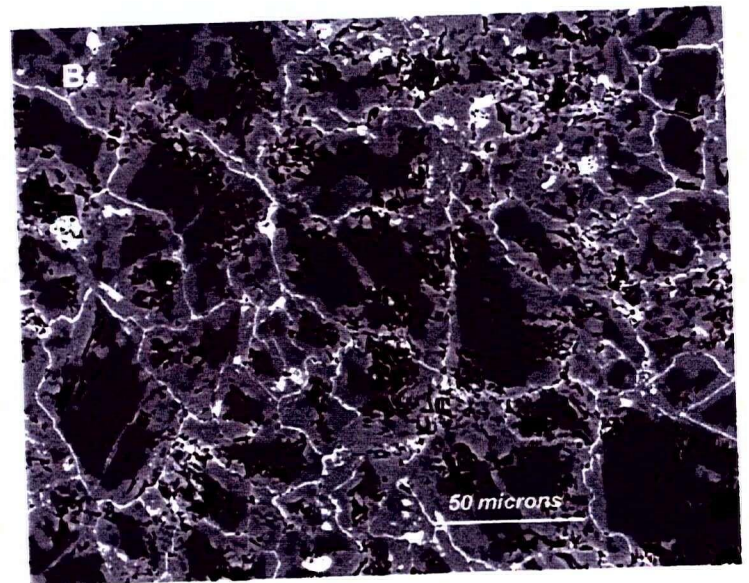
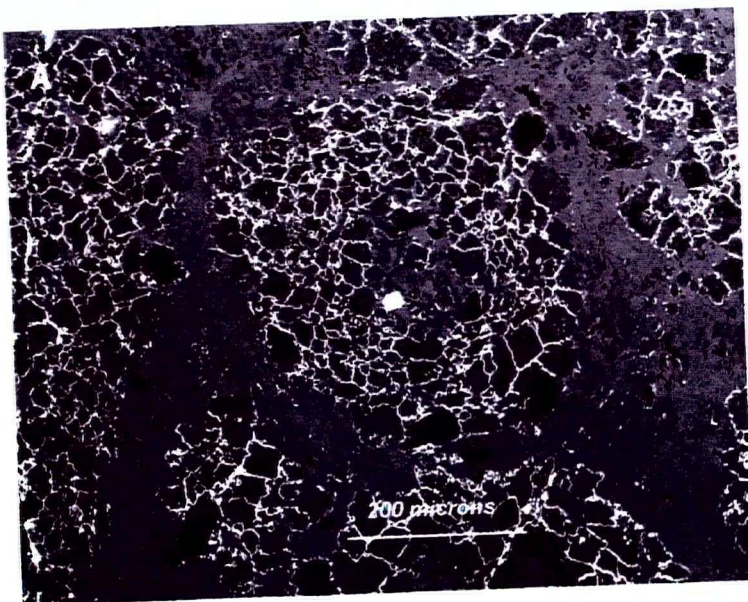


Plate 4.22. SEM image of dolomitization inside an ooid. Dark rhombs are dolomite, medium gray is calcite, and white is magnetite.

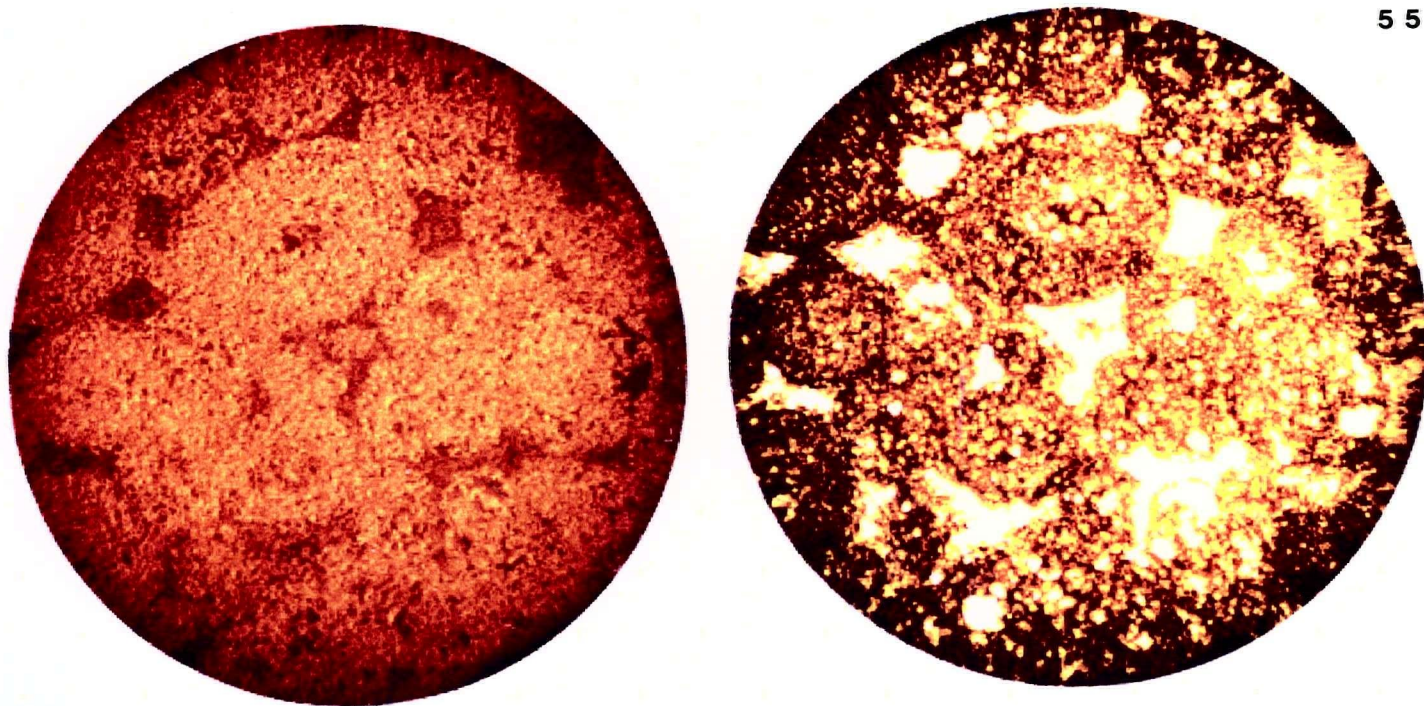


Plate 4.23. Bright yellow cathodoluminescent calcite, indicative of hydrothermal alteration. Left: cathodoluminescence; Right: transmitted plane polarized light.

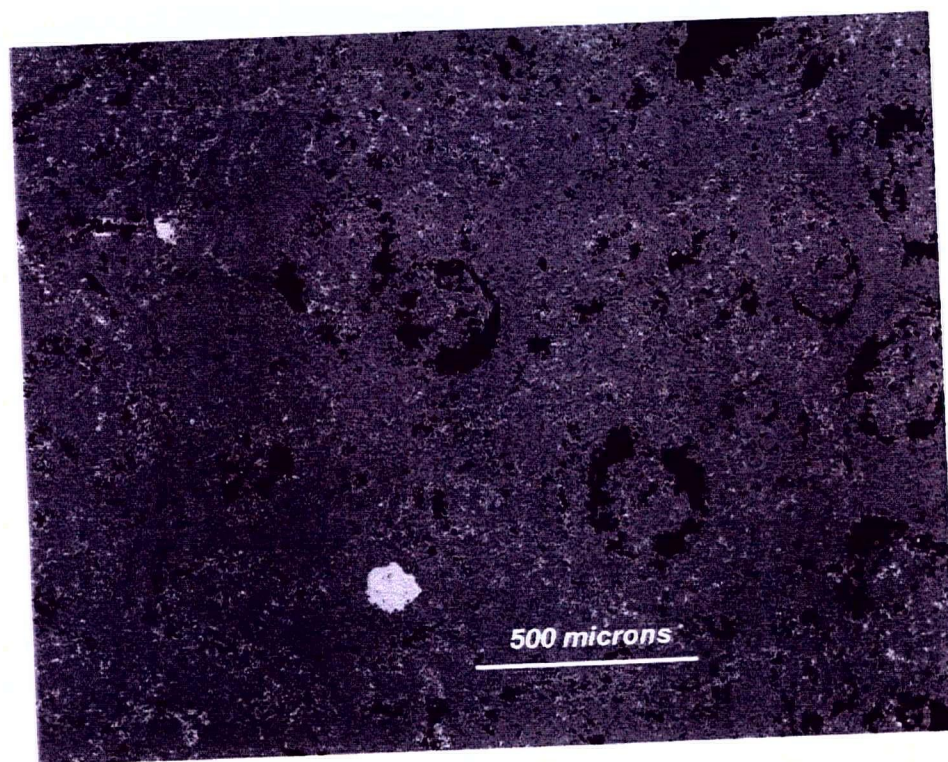


Plate 4.24. SEM image of ooids that have emit bright yellow cathodoluminescence. Gray is calcite, and interstitial white is magnetite. Large light gray grain at bottom centre is apatite.

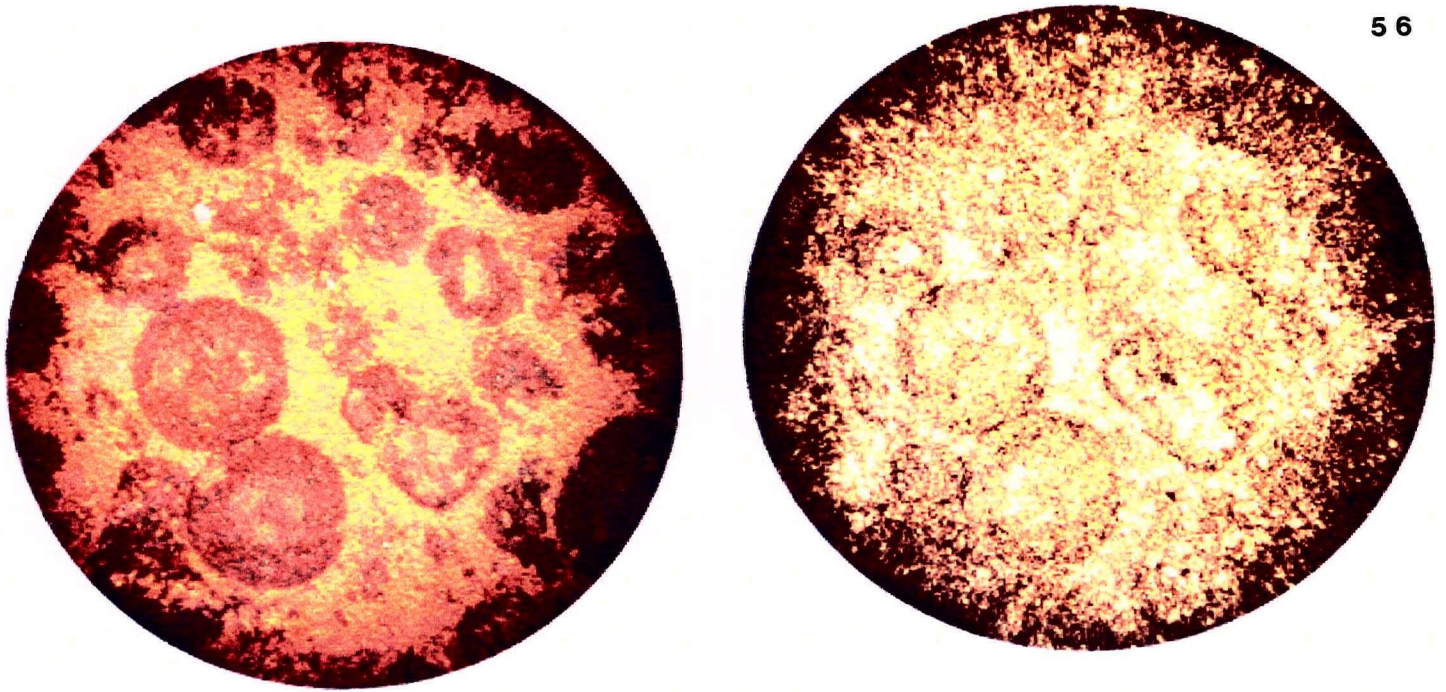


Plate 4.25. Cathodoluminescence pattern showing dolomitization of ooids, but no evidence of hydrothermal alteration (no bright yellow calcite).
Left: cathodoluminescence; Right: Transmitted plane polarized light.

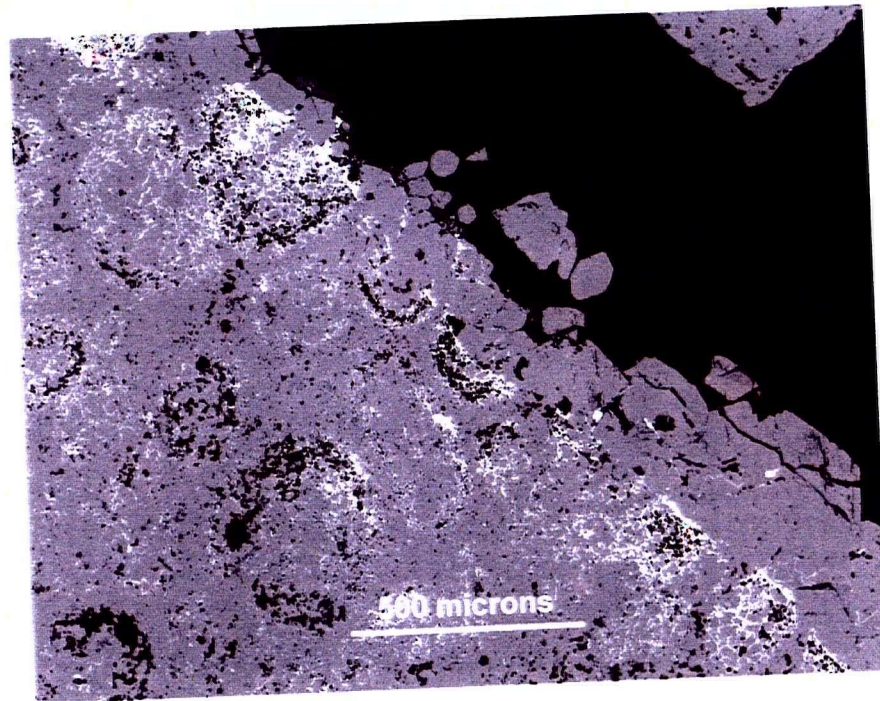


Plate 4.26. SEM image showing typical hydrothermal signature enhanced along fissures.

4.3.2 Other alteration effects

Other hydrothermal alteration effects observed in the area include bleaching and silicification. Bleaching of meta-sedimentary rocks adjacent to veins is the result of sericite alteration within 2 m of large quartz-sulphide veins, and within < 1 cm of small veins. Silicification is locally associated with stringer stockwork mineralization hosted in metasedimentary rock, but it is also encountered away from any form of gold mineralization.

4.4 Ore petrography

The different styles of mineralization in the Ketz River deposit share similar ore mineralogy, consisting mainly of pyrrhotite, pyrite, and arsenopyrite, with minor late marcassite and chalcopyrite, and rare (usually submicroscopic) native bismuth, sphalerite, and galena. Cataclastic texture in arsenopyrite and pyrite (plate 4.31) healed by quartz, muscovite, and chalcopyrite in orebodies localized along normal faults is significant because it suggests that faults were active at least during late stages of mineralization. Figure 4.2 shows the paragenetic relationships between opaque minerals in mantos, Fe-silicate alteration zones, and quartz-sulphide veins. Gangue mineralogy consists mainly of carbonate (calcite and ankerite) and quartz, with local white mica and chlorite. Amphiboles are present only in Fe-silicate alteration.

4.4.1 Opaque and gangue mineralogy in carbonate hosted ores

Cathro (1992) conducted a detailed petrographic study of the manto-style massive sulphide orebodies in the Ketz River area. Tables 4.1 to 4.4 are compilations of new petrographic observations on manto-style massive sulphide and associated Fe-silicate ores resulting from the present study.

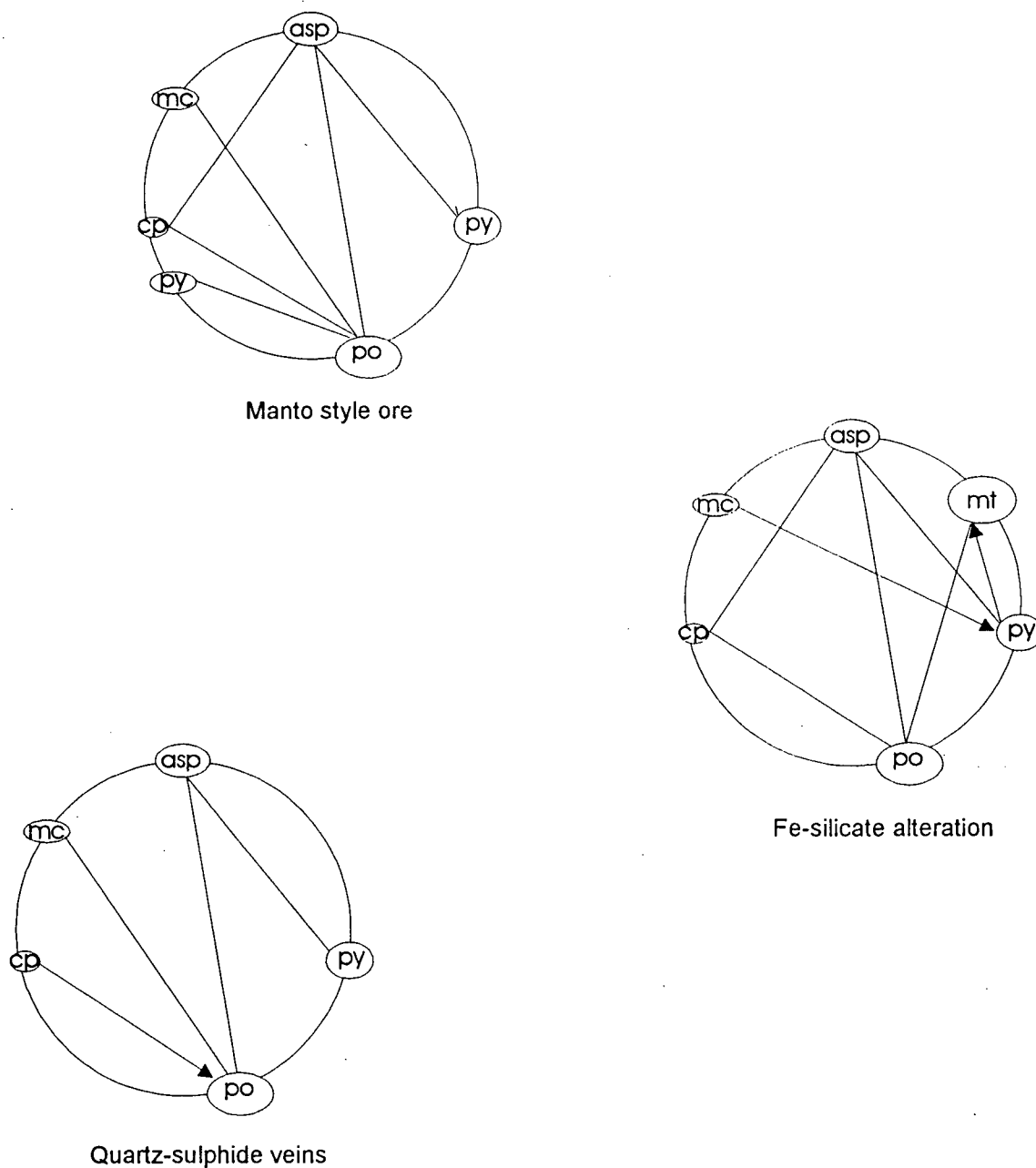


Figure 4.2. Paragenetic diagrams illustrating major opaque mineralogy in the three mineralization styles of the Ketz River deposit. Paragenetic sequence starts at the top and proceeds clockwise. The size of ellipses represents relative abundances. Interconnecting lines indicate mutual contacts. Arrows point to minerals that are replaced. Mineral abbreviations: asp = arsenopyrite; py = pyrite; mt = magnetite; po = pyrrhotite; cp = chalcopyrite; mc = marcasite.

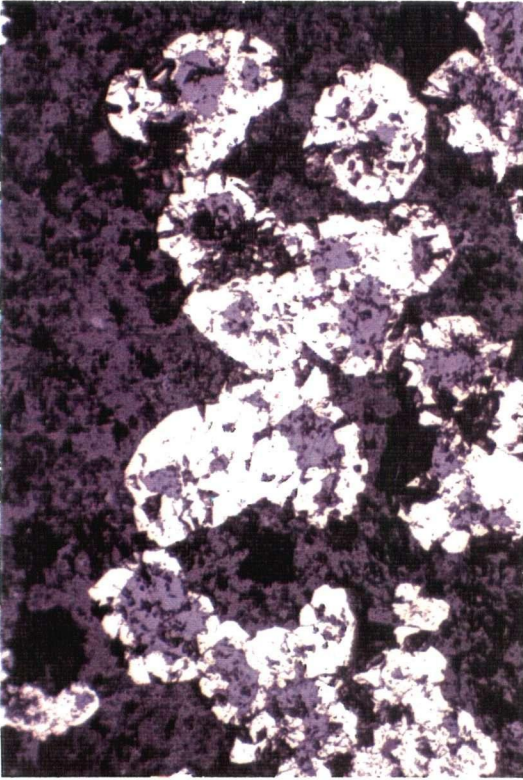


Plate 4.27. Euhedral magnetite (gray) surrounded by later, euhedral pyrite (yellow). Field of view = 2 mm.

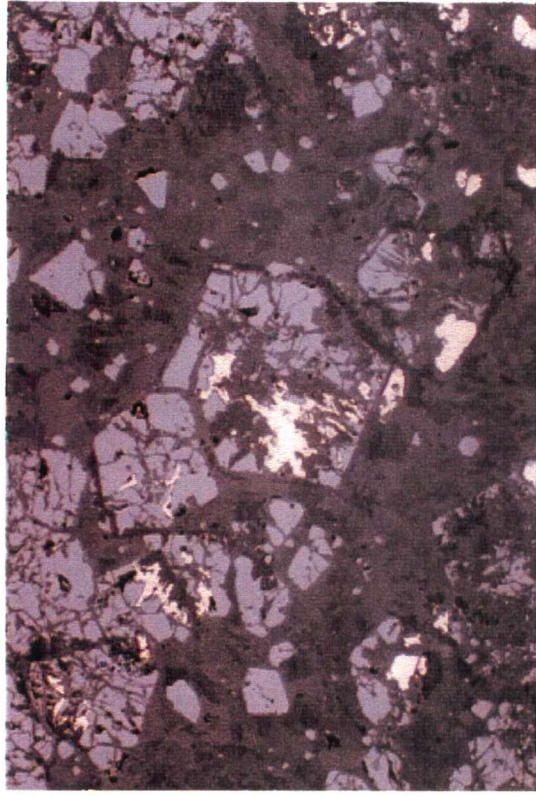


Plate 4.28. Euhedral magnetite (gray) replaced by pyrite (yellow), and cross-cut by quartz and muscovite (dark gray). Field of view = 1 mm.



Plate 4.29. Early, euhedral arsenopyrite (white) cross-cut by quartz and muscovite (dark gray). Field of view = 2 mm.

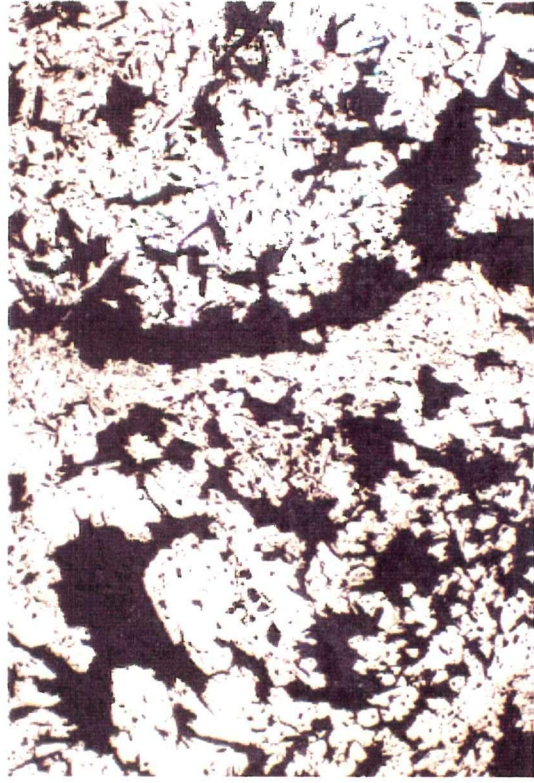


Plate 4.30. Late pyrite. Bladed texture is due to filling of open spaces around Fe-silicate needles. Field of view = 2mm.

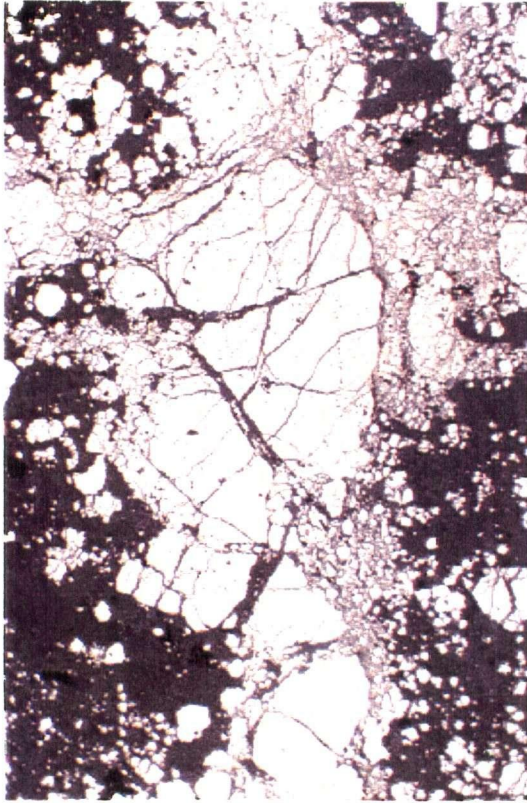


Plate 4.31. Cataclastic pyrite occurs locally along mineralized normal faults, and is indicative that those faults were active at the time of mineralization. Field of view = 2 mm.

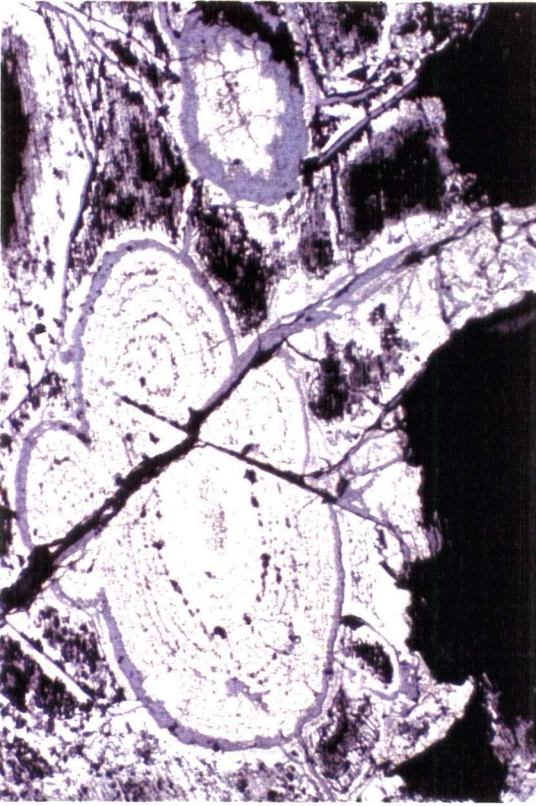


Plate 4.32. Late, colloform marcasite. Field of view = 2 mm.

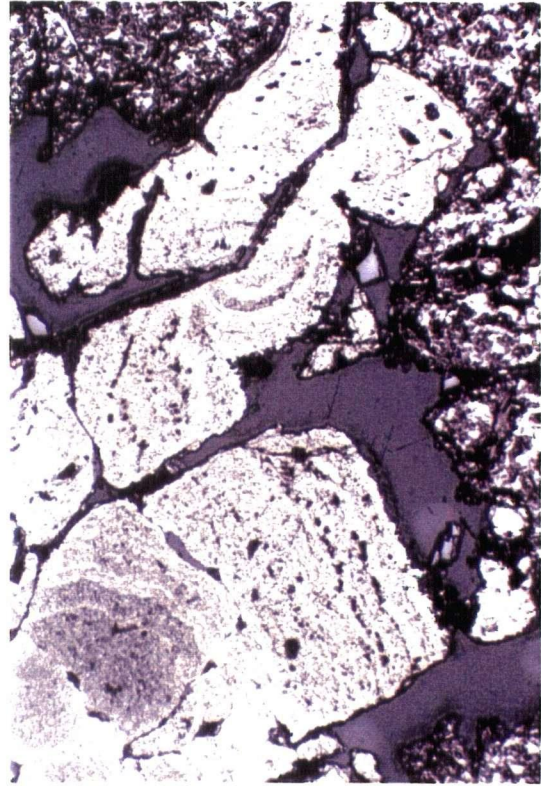


Plate 4.33. Late, colloform marcasite replacing pyrite cubes. Field of view = 2 mm.

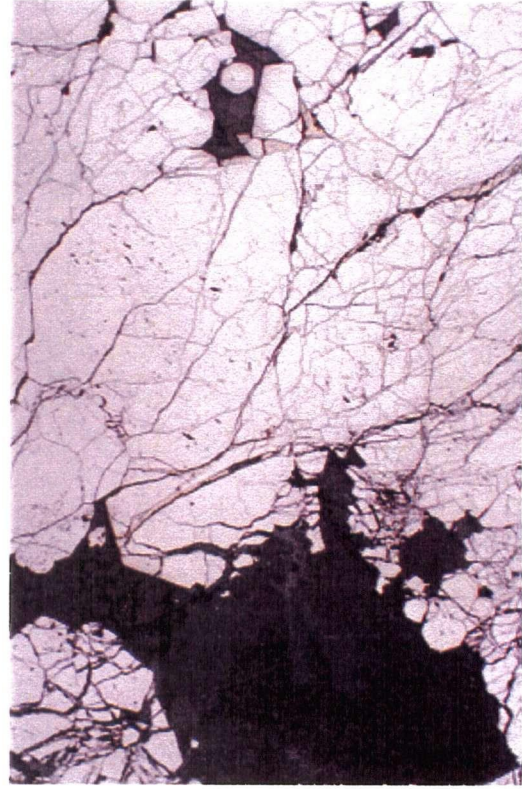


Plate 4.34. Late chalcopyrite (bright yellow veins) cross-cutting arsenopyrite (white). Field of view = 2 mm.

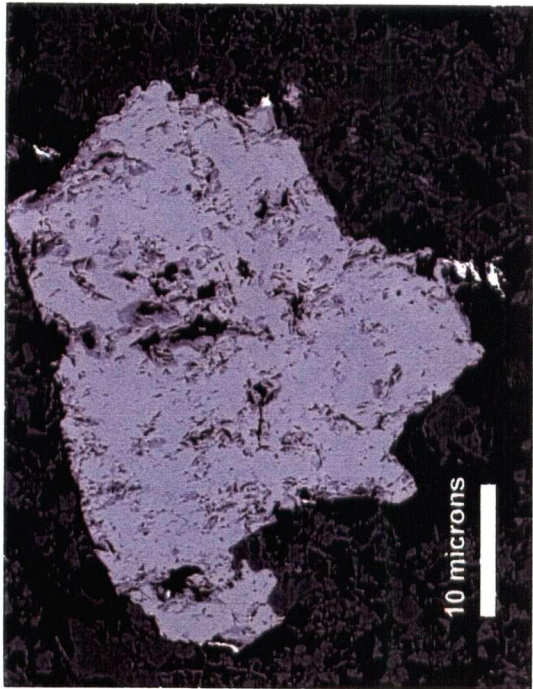


Plate 4.35. SEM image of arsenopyrite (large, gray), and native bismuth (small, bright white).



Plate 4.36. Fine-grained muscovite (light gray) intergrown with quartz (dark gray) and pyrrhotite (yellow). Field of view = 10 mm.



Plate 4.37. Fe-amphibole needles intergrown with magnetite (black). Field of vies = 2 mm.

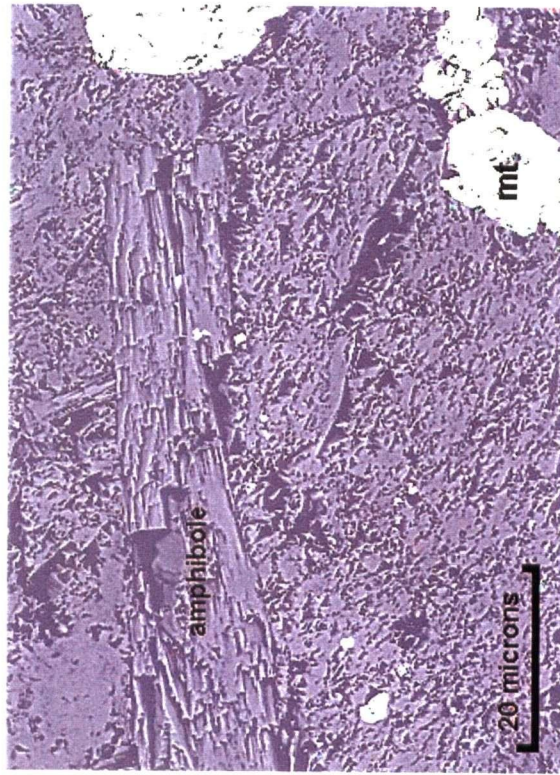


Plate 4.38. SEM image of Fe-amphibole (gray, elongated), calcite (gray), and magnetite (white).

Table 4.1 Opaque mineralogy in massive sulphide mantos. Minerals listed in order of abundance.

mineral	abundance	stage	crystal form	crystal size
pyrrhotite	>85% of opaques	intermediate	Anhedral masses	
early pyrite (plate 4.31)	1-5% of opaques locally >70%	early	Euhedral cubes and other cubic forms, locally cataclastic.	<5 mm
arsenopyrite (plate 4.29)	<10%	early	Euhedral prisms with bipyramidal termination, locally cataclastic.	<4 mm
marcasite (plate 4.33)	1-10% of opaques	latest	Colloform masses	<0.5 mm
late pyrite	<3% of opaques	late	Anhedral cores of colloform marcasite masses and fissure fillings in pyrrhotite and arsenopyrite	
chalcopyrite	<1%, local	late	Anhedral masses (ocasionally replacing pyrrhotite) and fissure fillings	<0.5 mm
sphalerite	Trace Locally >35%	intermediate	Anhedral masses	
galena	Trace Locally >10%	intermediate	Subhedral inclusions in arsenopyrite (early) Anhedral masses (late)	<0.2 mm
native bismuth (plate 4.35)	trace	intermediate	Anhedral masses surrounding or filling fissures in arsenopyrite	<0.02 mm

Table 4.2 Gangue mineralogy in massive sulphide mantos. Minerals listed in order of abundance.

mineral	abundance	stage	crystal form	crystal size
carbonate (calcite and ankerite)	<15% of ore	early to late	Euhedral rhombs (early) Pressure shadows (open space filling) surrounding sulphides (late)	<0.3 mm
quartz	5-35% of ore	early to late	Euhedral prisms (early) Subhedral to anhedral grains (late)	<2 mm
muscovite (plate 4.36)	Trace Locally >5%	intermediate	Subhedral platy prisms	<0.1 mm

Table 4.3 Opaque mineralogy in Fe-silicate alteration. Minerals listed in order of abundance.

mineral	abundance	stage	crystal form	crystal size
pyrrhotite	Most abundant 35-98% of opaques	intermediate	Anhedral masses	
magnetite (plates 4.27, and 4.28)	Variable <1-98%	early	Euhedral octahedra	0.13-28 mm
arsenopyrite	2-16% of opaques	early	Euhedral Prisms with bipyramidal terminations	>3mm
marcasite (plate 4.32)	3-15% of opaques	latest	Colloform nodules Associated with pyrrhotite	>0.5 mm
pyrite (plates 4.27, 2.28, and 4.30)	1-5% of opaques locally up to 30- 40% of opaques	early and late	Euhedral to subhedral (early) crystals Anhedral masses and fissure fillings (late)	>2mm (early crystals)
chalcopyrite (plate 4.34)	Locally 1-2%	late	Anhedral masses and fissure fillings	<3mm
native bismuth	Ubiquitous, but submicroscopic	intermediate	Anhedral masses surrounding or filling fissures in arsenopyrite	>0.02 mm
galena	trace	intermediate	Inclusions in arsenopyrite	>0.02 mm
sphalerite	trace	intermediate	Inclusions in arsenopyrite	>0.02 mm

Table 4.4 Gangue mineralogy in Fe-silicate alteration. Minerals are listed in order of abundance.

mineral	abundance	stage	crystal form	crystal size
carbonate (calcite and ankerite)	12-25% of ore	early to late	Euhedral to anhedral	<0.2 mm
Fe-amphibole (plates 4.37 and 4.38)	Locally <25% of ore	early	Euhedral, radiating acicular to prismatic crystals	<0.5 mm
quartz (early)	1-12% of ore	early	Euhedral to subhedral clusters of prisms	<0.3 mm
chlorite	<2%	early	Subhedral radiating flakes	<1mm
quartz (late)	<1% of ore	late	Anhedral, filling spaces between pyrite grains, and along stylolites	>0.7 mm
muscovite	Trace Locally >1% of ore	intermediate	Subhedral tabular prisms	>0.1 mm

4.4.2 Opaque and gangue mineralogy in veins hosted by meta-sedimentary rocks (unit 1a)

Opaque and gangue mineralogy of quartz-sulphide veins and stockwork is summarized in tables 4.5 and 4.6.

Table 4.5 Opaque mineralogy in quartz-sulphide veins in metasedimentary rock. Minerals listed in order of abundance.

mineral	abundance	stage	crystal form	crystal size
pyrrhotite	>80% of opaques	intermediate	Anhedral masses	
pyrite	10-70% of opaques	early and late	Euhedral cubic forms (early) Anhedral clear crystalline cores surrounded by marcasite (late) Anhedral replacement of pyrrhotite (late)	<4mm (early cubic crystals)
arsenopyrite	30-100% of opaques	early	Euhedral to subhedral prisms with bipyramidal terminations	<3 mm
marcasite	<12% of opaques	latest	Colloform masses along fissures in pyrrhotite	<0.2 mm
chalcopyrite	<1% of opaques, local	late	Anhedral replacement rims and fissure fillings associated with pyrrhotite	<0.4 mm
galena	Trace	early	Euhedral cubes and inclusions in arsenopyrite	<0.02 mm
sphalerite	Trace	intermediate	Anhedral masses	<0.02 mm
native bismuth	Trace	intermediate	Anhedral masses filling fissures and rimming arsenopyrite	<0.04 mm

Table 4.6 Gangue mineralogy in quartz-sulphide veins in metasedimentary rock. Minerals listed in order of abundance.

mineral	abundance	stage	crystal form	crystal size
quartz	75-95% of vein	early	Anhedral, milky, often brecciated	<0.3 mm
calcite	<10%	early	Euhedral to subhedral rhombs	<0.3 mm
sericite	trace	early	Subhedral, tabular prisms	<1 mm
chlorite	trace	early	Subhedral, radiating prisms	<0.3 mm

4.4.3 Summary of ore mineralogy and paragenetic sequence

Opaque mineralogy and paragenetic sequence in mantos, Fe-silicate alteration zones, and quartz-sulphide veins is similar, and is depicted in figures 4.2 and 4.3. Early stage minerals

include arsenopyrite and euhedral pyrite in all ore types, and magnetite in Fe-silicate alteration zones. Native bismuth, galena, and sphalerite fill fissures in arsenopyrite, and represent an intermediate stage of sulphide deposition. Pyrrhotite also precipitated during the intermediate stage, but the fact that it is not associated with native bismuth, galena, and sphalerite suggests that it is immediately later than those three minerals. The intermediate stage is followed by late pyrite and chalcopyrite, both replacing and filling fissures in arsenopyrite and pyrrhotite. Marcassite is the latest opaque phase. Marcasite forms open-space fillings in pyrrhotite, and replaces early pyrite.

Gangue mineralogy is dominated by coarse-grained carbonates (calcite and ankerite), and quartz. Quartz and carbonates (in all ore types) and Fe-amphibole (in Fe-silicate alteration zones) started to precipitate during the early stage, and continued precipitating into the intermediate stage. Micas cross-cut early sulphide, and are therefore later.

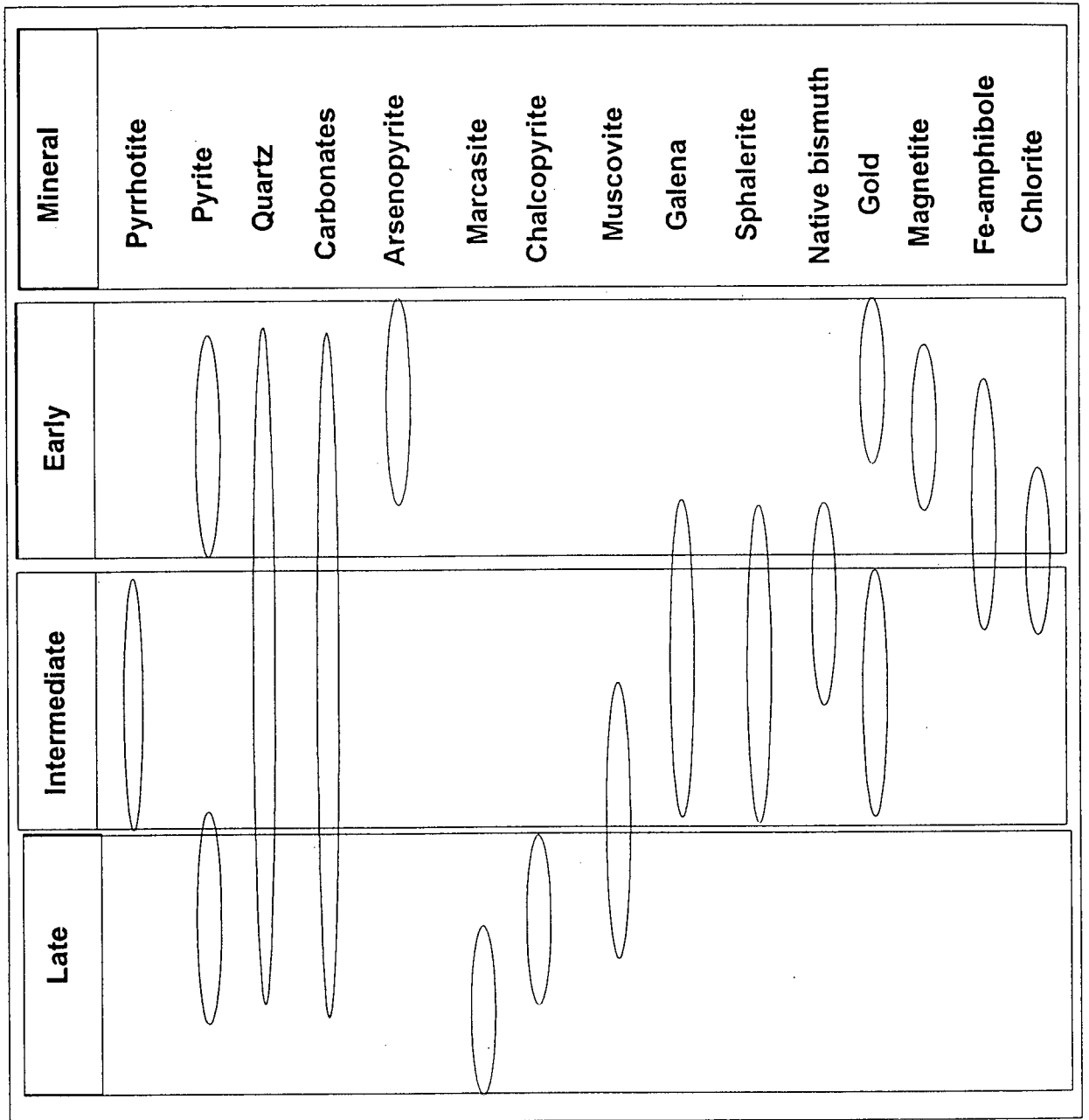


Figure 4.3. Paragenetic diagram showing relative timing of deposition of opaque and gangue minerals. Paragenetic sequence is similar for the different styles of mineralization. Magnetite, Fe-amphibole, and chlorite are part of the Fe-silicate assemblage only.

5 GEOTHERMOMETRY

Arsenopyrite geothermometry was undertaken in an attempt to determine temperatures of deposition of sulphides in manto, Fe-silicate alteration zones, and vein mineralization in the Ketza River area, and to compare depositional temperatures along different mineralized faults in order to determine where a thermal centre would have been. The final results provide maximum temperature estimate only, and because of limitations of the method, a comparison between temperatures along different mineralized structures was not possible. The maximum temperature estimate was critical for the interpretation of geochronological data (see discussion in the following chapter).

5.1 Arsenopyrite geothermometry

The arsenopyrite geothermometer (Kretschmar and Scott, 1976) was developed for estimating temperatures of deposition of arsenopyrite, as a function of sulphur abundance. Sulphur abundance can be estimated based on the iron sulphide assemblage in equilibrium contact with arsenopyrite, and composition can be measured with an electron microprobe. Sharp et al. (1985) compared temperature estimates from arsenopyrite geothermometry to temperature data from other thermometric methods and concluded that typically wide compositional ranges of arsenopyrite composition in hydrothermal ores renders the arsenopyrite geothermometer inappropriate for temperature estimation, unless external supporting geothermometric data exists. More recent studies (e.g., Newberry et al., 1995; McCoy et al., 1997) show that temperature estimates from arsenopyrite geothermometry applied to hydrothermal ore deposits are comparable to those obtained from fluid inclusions, as long as microprobe analyses are run strictly along pyrite contacts (McCoy, in prep.).

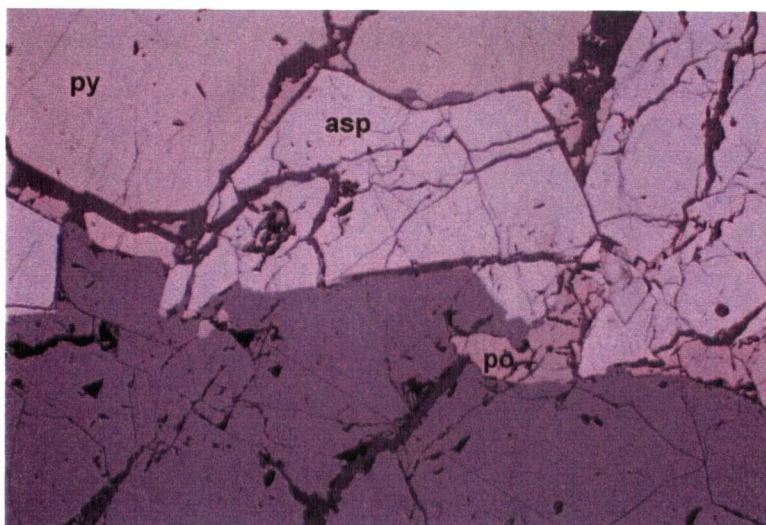


Plate 5.1. Arsenopyrite geothermometry assemblage, with early euhedral arsenopyrite and pyrite, and late anhedral pyrrhotite.

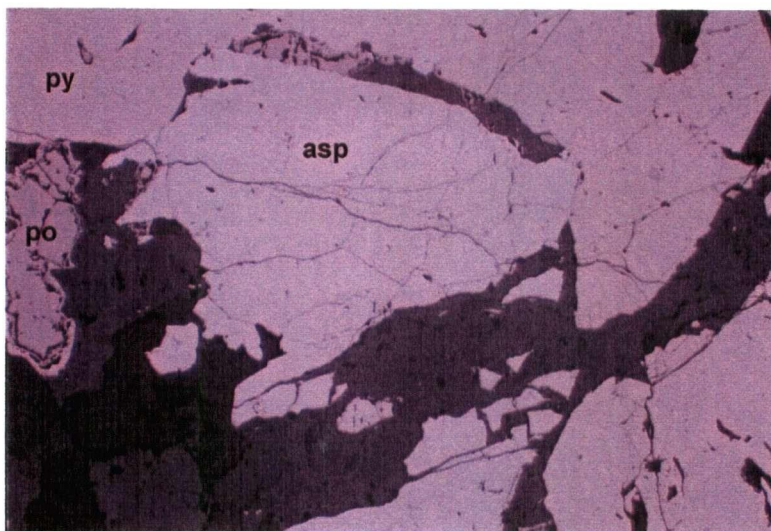


Plate 5.2. Arsenopyrite geothermometry assemblage, with early euhedral arsenopyrite and pyrite, and later anhedral pyrrhotite.

A preliminary optical microscopy survey of samples containing arsenopyrite, pyrite and pyrrhotite in the same polished thin section resulted in the selection of eleven samples in which arsenopyrite occurs in direct contact with pyrite and pyrrhotite, or in direct contact with pyrite only, but where pyrrhotite is found in the vicinity of the arsenopyrite grains. Samples in which pyrite showed evidence of being a later phase (e.g., cross-cutting relationships with arsenopyrite and pyrrhotite) were rejected. Plates 5.1 and 5.2 show the typical sulphide assemblage used for the geothermometer. Pyrite and arsenopyrite form early, euhedral crystals, whereas pyrrhotite forms later anhedral masses. The later character of pyrrhotite suggests that it was not in equilibrium with pyrite and arsenopyrite at the time of deposition. Fe-As-S stability fields in which pyrite and arsenopyrite (but not pyrrhotite) are in equilibrium correspond to low temperature reactions (Figure 5.2).

5.2 Techniques

Major (As, S, Fe) and minor (Mn, Co, Ni, Cu, Zn, Sb) element analyses of arsenopyrite crystals were performed using a Cameca SX-50 electron microprobe at the University of British Columbia. The analyses were carried out using asp200 (natural homogeneous S-rich arsenopyrite from the Lucie Pit, Helen siderite mine, Ontario) for the calibration of As, S, Fe, and as a working standard for periodic checks on the calibration. Standards used in the calibration of minor elements, and analytical parameters are listed in table 5.1. In most cases, 3 to 5 points were analyzed on each arsenopyrite grain, immediately adjacent to pyrite contacts. Five 10-second counts were performed for each data point. Corrections for dead time and background were followed by ZAF corrections (corrections for matrix effects regarding atomic number, absorption, and fluorescence). Weight percent and atomic percent calculations for individual elements, and statistics for each analysis were performed by the X-Mas software.

Table 5.1. Microprobe calibration standards and analytical parameters.

a) Calibration standard

Standard number	mineral	elemens calibrated	crystal
s418	arsenopyrite(asp57)	As (La)	TAP
s418	arsenopyrite (asp57)	S (Ka)	PET
s418	arsenopyrite (asp57)	Fe (Ka)	LIF
s311	native Mn	Mn (Ka)	LIF
s313	native Co	Co (Ka)	LIF
s314	native Ni	Ni (Ka)	LIF
s289	tennantite	Cu (Ka)	LIF
s141	sphalerite	Zn (Ka)	LIF
s288	tetrahedrite	Sb (La)	PET

b) Analytical parameters

Beam current:	20 nA	Tilt angle:	0°
Accelerating voltage:	20 kV	Azimuth angle:	0°
Take off angle:	40°	Analyses:	5 sets of 10 second counts

5.3 Temperature estimates from arsenopyrite geothermometry

Arsenopyrite is an early, euhedral phase in the Ketz River massive sulphide mantos. Relatively closely clustering temperatures of deposition were anticipated, as arsenopyrite is considered to have precipitated during a single, early depositional event.

Preliminary comparisons between atomic % As data for rim and core of arsenopyrite crystals in contact with pyrite and pyrrhotite showed a significant difference in atomic % As between rim and core. This substantial difference invalidated the use of core data points for the geothermometer, as the temperatures for the cores are not constrained by equilibrium reactions. Figure 5.1 is a histogram of atomic % As, showing the difference in composition measured on the rim and on the core of arsenopyrite crystals in the same sample, with higher atomic % As in cores.

Atomic % As measured on arsenopyrite rims only have modes ranging from 29.1 to 29.7. The equilibrium phase diagram of Kretschmar and Scott (1976) lacks experimental data at the low atomic % As end. By extrapolating from the existing calibration data, and assuming that low temperature reactions mimic the pattern observed for higher temperature syntheses,

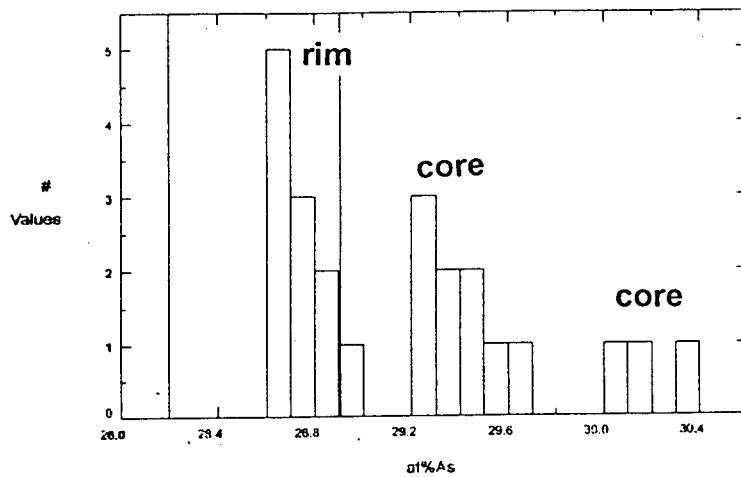


Figure 5.1. Atomic % As measured along rims and cores of arsenopyrite crystals in contact with pyrite show a bimodal distribution.

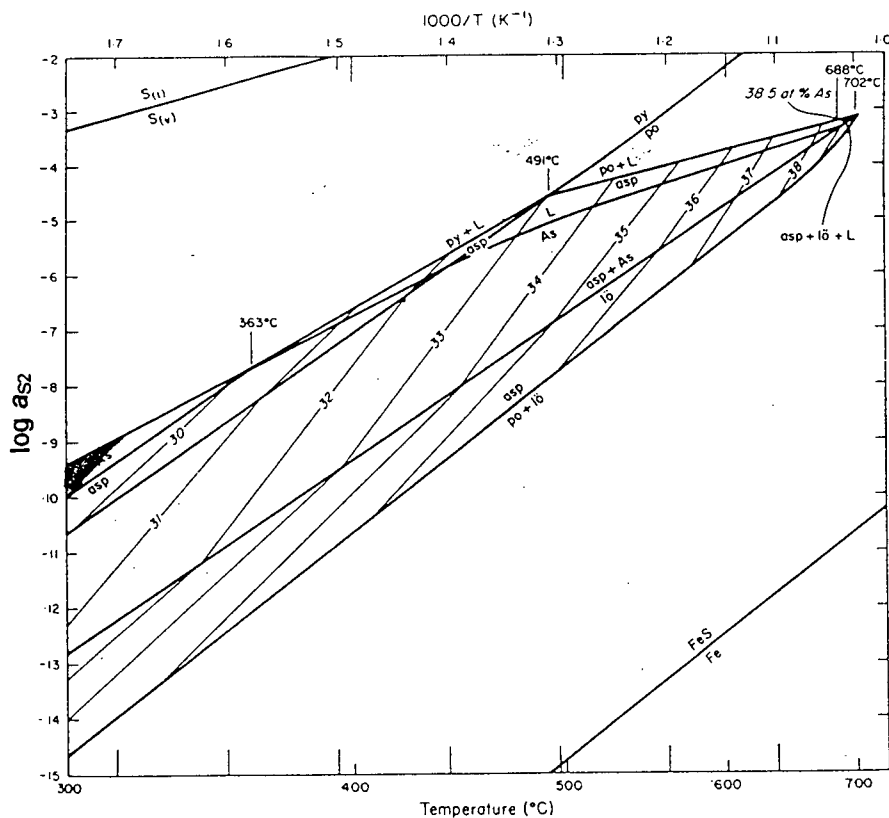


Figure 5.2. Activity of S_2 - temperature projection of the stability field of arsenopyrite, contoured in atomic % arsenic. All assemblages include vapour. From Kretschmar and Scott (1976).

temperatures <330° C can be tentatively estimated for the Ketz River ores. This extrapolation is reasonable, since mineral assemblage stability fields shown in Figure 5.2 are rather continuous, and the spacing between isopleths decreases gradually to the left (lower temperature field).

Table 5.2. Summary statistics and brief description of samples.

Sample #	mode	Atomic % As			st dev	n	ore type
		mean	min	max			
4425	29.6	29.4	29	29.8	0.21	15	massive sulphide manto
4426	29.4	28.2	27.8	30	0.43	43	massive sulphide manto
4427	29.3	29.4	28	30.7	0.45	64	massive sulphide manto
4447	29.1	29.2	27.6	30.5	0.53	57	massive sulphide manto
4448	29.7	29.3	28.3	30	0.46	36	massive sulphide manto
4449	29.3	28.9	27.5	29.7	0.57	24	massive sulphide manto
5353	28.7	29.2	28.5	30.5	0.55	22	massive sulphide manto
5354	29.1	27.4	28.3	30.3	0.46	61	massive sulphide manto
5375	28.8	28.4	27.2	29.6	0.49	94	sphalerite-galena-rich manto
5376	28.8	28.7	27.4	29.8	0.52	39	sphalerite-galena-rich manto

Figure 5.2 is a log $a(\text{S}_2)$ versus temperature diagram showing arsenopyrite isopleths contoured in atomic %. The isopleths for 28 and 29 at% As are beyond the range of this diagram, but they would intercept the py+L+asp curve at temperatures well below 330°C. The py+As+asp curve would be intercepted at slightly lower temperatures. No native arsenic was observed in SEM examinations, but it is possible that native arsenic was initially in equilibrium with pyrite and arsenopyrite, but was subsequently removed by late stage hydrothermal fluids.

Appendix C shows atomic percentages calculated from microprobe analyses produced during this study. Sample locations are indicated in Figure 5.3. Histograms of atomic % As in arsenopyrite rims along pyrite contacts from samples from different areas are presented in figure 5.4.

5.4 Fluid inclusion thermometry

Homogenization temperatures from fluid inclusions provide minimum temperature estimates that can be compared with maximum temperature estimated from arsenopyrite geothermometry. Minimum temperatures recorded for vein quartz in the QB Zone (metasedimentary rock hosted

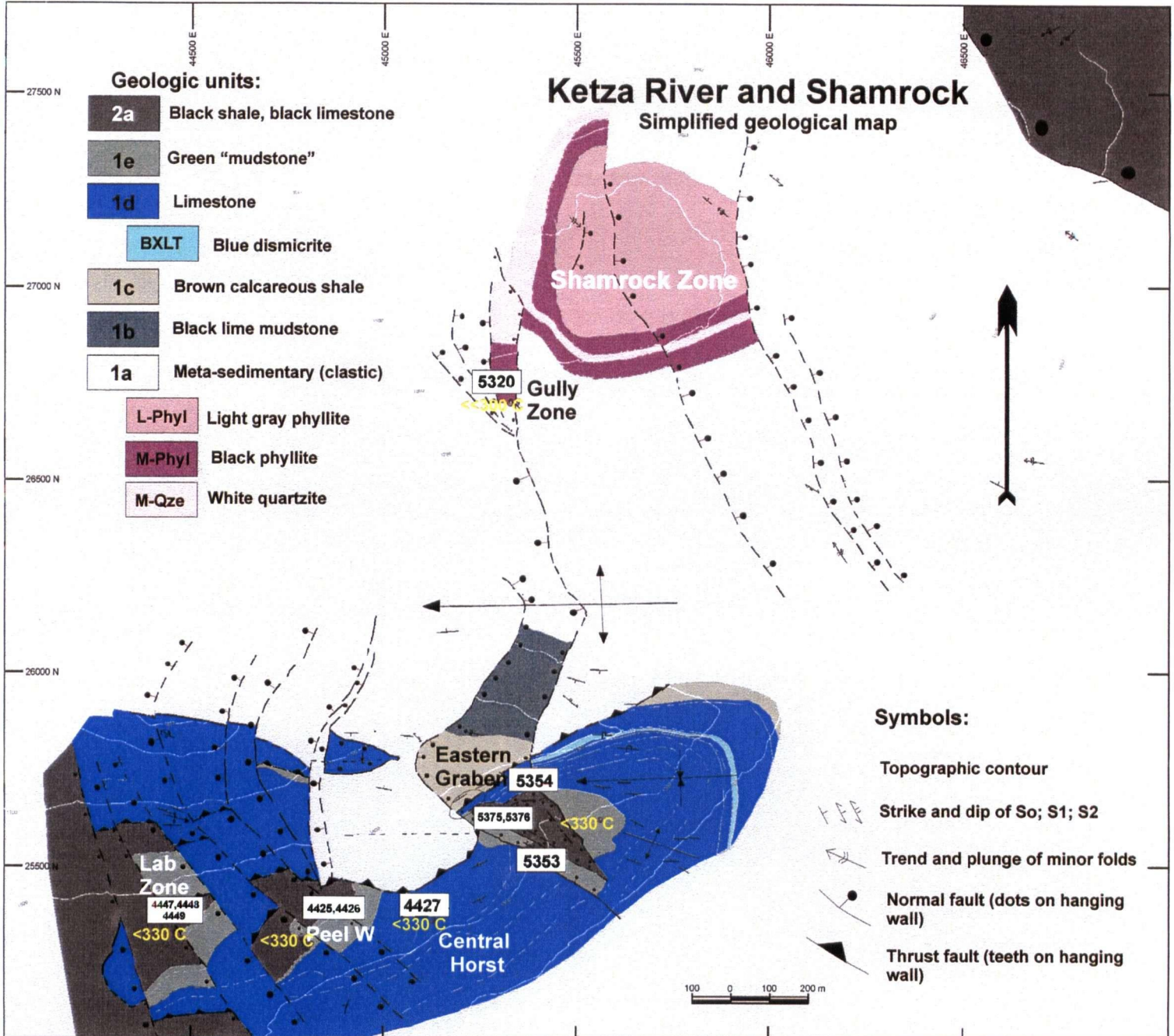


Figure 5.3. Geologic map of the Ketz River area showing arsenopyrite geothermometry sample locations and estimated temperatures of ore deposition for each zone or structural domain.

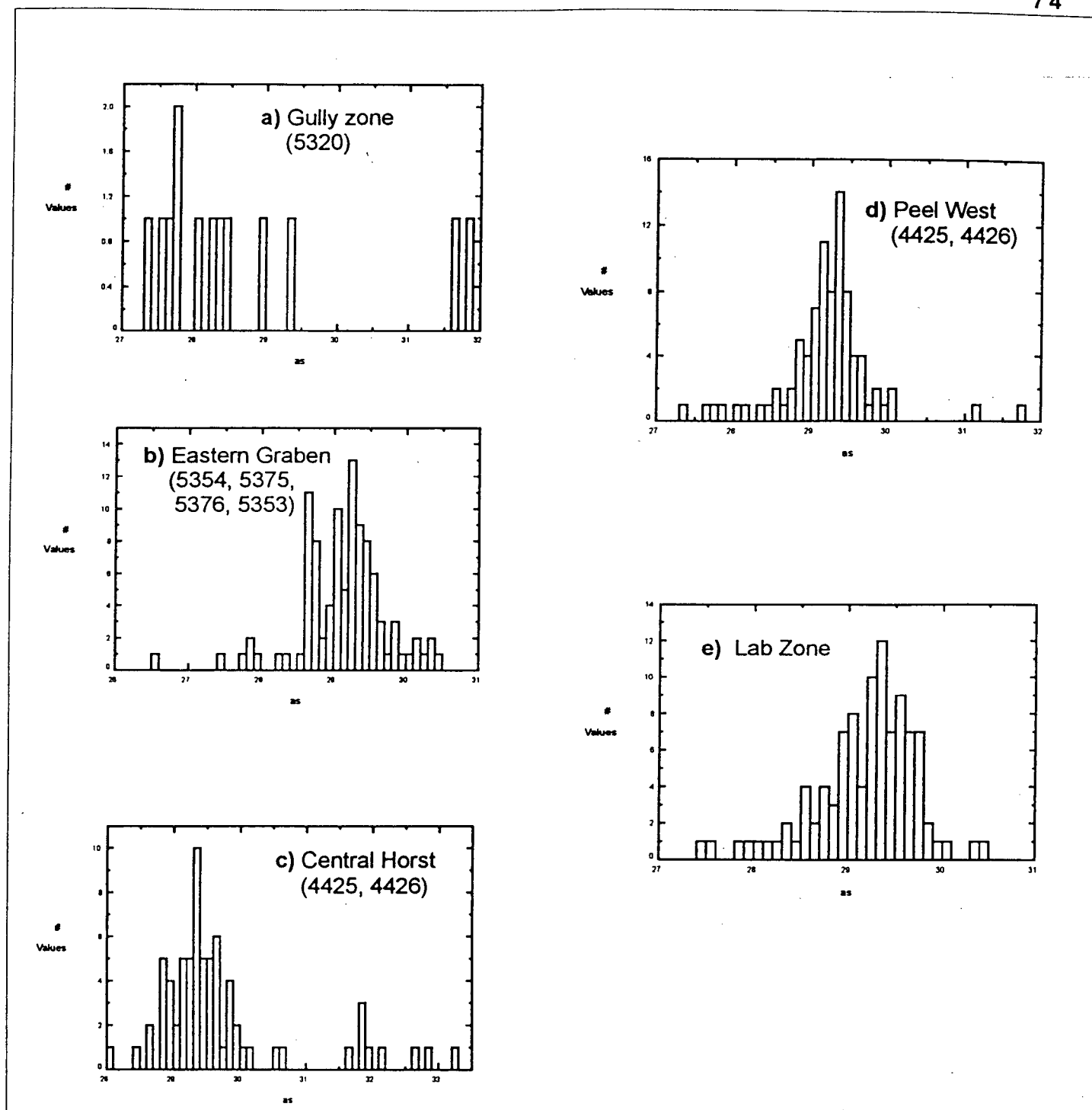


Figure 5.4. Histograms of atomic % As in arsenopyrite for the various zones or structural domains with pyrite-arsenopyrite-pyrrotite assemblage in ore.

quartz-sulphide veins) are consistent with maximum depositional temperatures estimated from the arsenopyrite geothermometry.

Staveley (1992) conducted fluid inclusion studies in vein quartz from six localities in the Ketza River area. In most cases, the nature (primary or secondary) of the inclusions studied was not ascertained. Furthermore, some of the quartz veins (particularly those from the Peel and Oxo zones) used in that study may be from a pre-D₂ generation of barren, deformed quartz veins. Complete descriptions of the vein material analysed are lacking. Temperature estimates reported by Staveley (1992) are: 256-324° C (Peel Zone); 231-316° C (QB Zone); 220-243° C (Mount Fury, NW of the present study's map area); 245-280° C (Next Valley, W of map area); 304-402° C (Oxo, SE of map area). The relatively consistent volume percentage of H₂O observed by Staveley (1992) suggests that boiling did not occur. In that case homogenization temperatures represent minimum trapping temperatures. However, Staveley (1992) proposed that the amount of data is insufficient for concluding whether boiling occurred or not.

6 DATING AND LEAD ISOTOPE STUDIES

Dating was undertaken in order to relate the hydrothermal event that produced the different mineralization styles of the Ketz River deposit to regional plutonic suites.

6.1 Previous work

A sample of hornfelsed metasedimentary rock (unit 1a) was dated by whole rock K-Ar method at the UBC geochronology laboratory. Cathro (1992) reports that the sample was collected within 100 m of a large quartz-sulphide vein in the Shamrock Zone. However, coordinates reported in the UBC K-Ar database correspond to an area immediately north of the Lab Zone, where unit 2a black shale is exposed on the Western Graben.

The sample yielded an age of 101 +/- 8 Ma. Given the error associated with this age, it coincides with the age of emplacement of the Cassiar suite of plutonic rocks that straddle the location of the Ketz River deposit.

6.2 $^{40}\text{Ar}/^{39}\text{Ar}$ dating

The purpose of $^{40}\text{Ar}/^{39}\text{Ar}$ analyses was to determine the age of mineralization in the Ketz River area, to test possible age correlations between the mineralization and granitic plutonism in the region, and to confirm the K-Ar age mentioned above. Two mica separates were analysed in the Geochronology Laboratory at the University of Alaska Fairbanks. The samples were run against standard Mmhb-1 (513.9 Ma age), and processed using standards of Steiger and Jäger (1977). Errors are quoted at a 1sigma error level. Data from step heating are presented in Appendix D.

6.2.1 $^{40}\text{Ar}/^{39}\text{Ar}$ age of mica from a quartz-sulphide vein

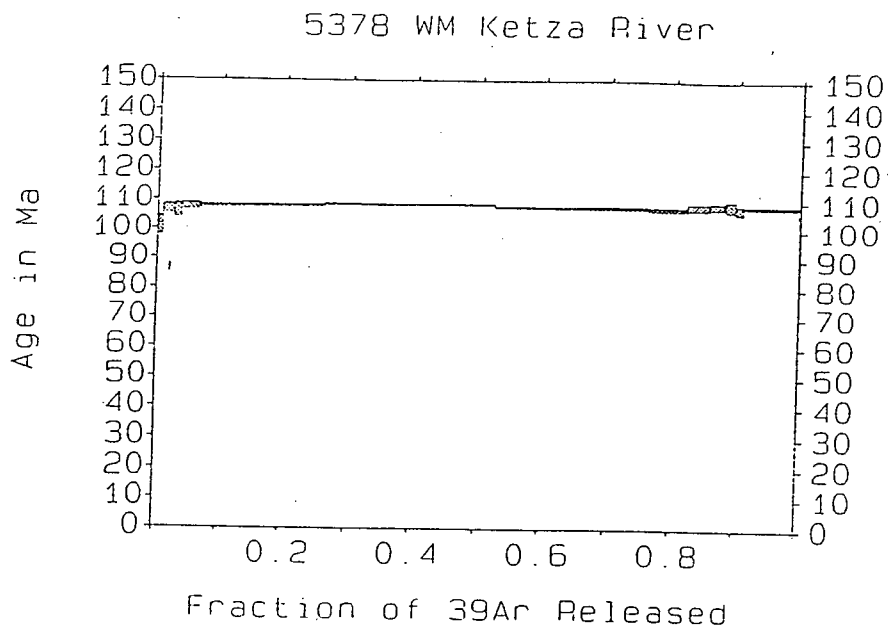


Figure 6.1. Plateau shaped (undisturbed) age spectrum for muscovite in quartz-sulphide vein from the Shamrock zone (sample 5378).

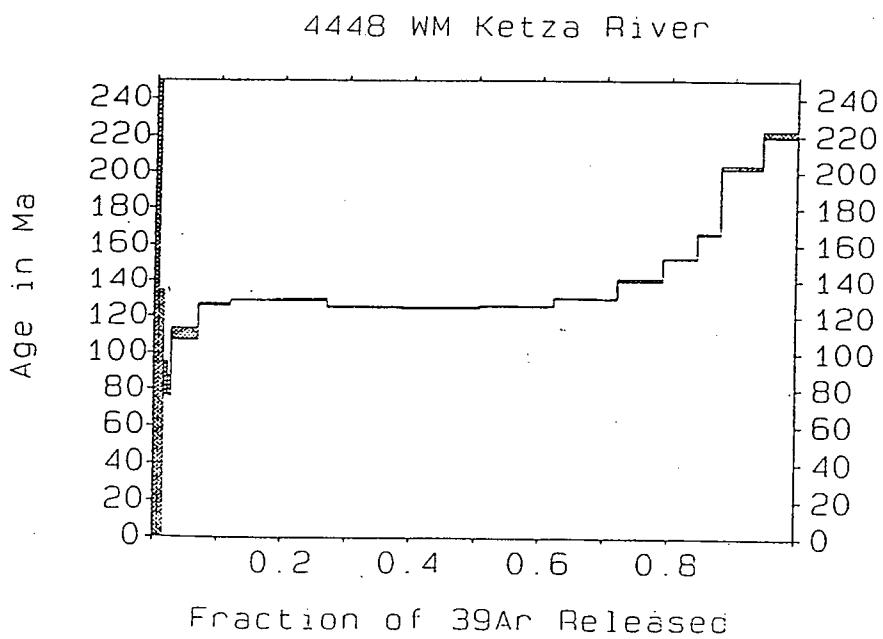


Figure 6.2. Saddle shaped age spectrum indicative of excess argon contamination, for muscovite in carbonate hosted manto style mineralization (sample 4448).

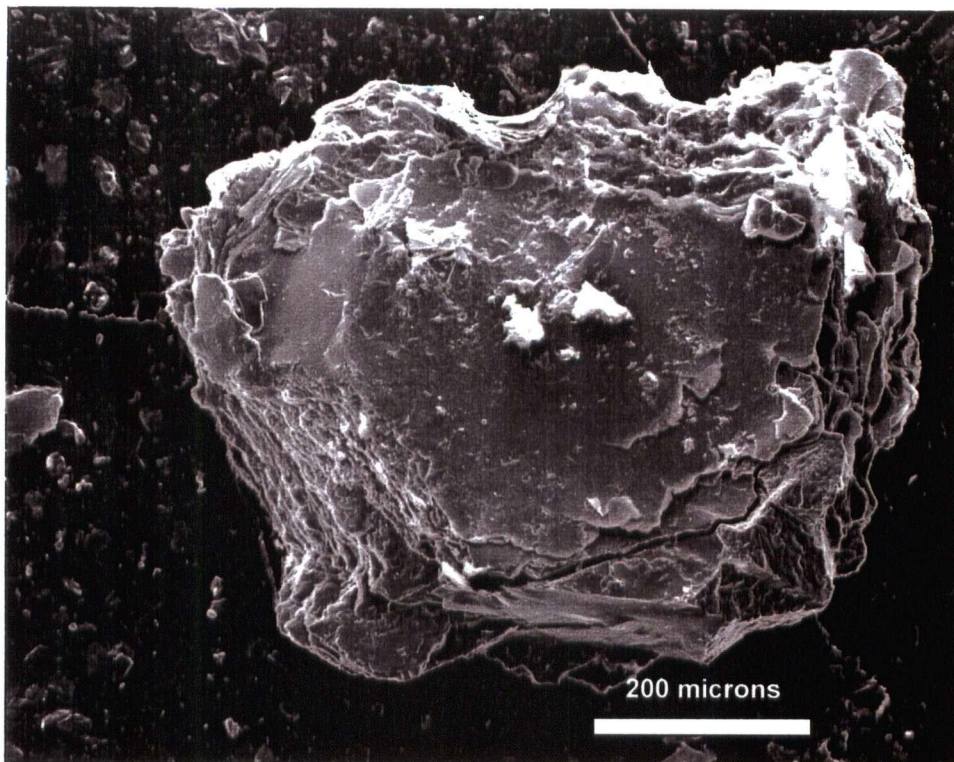


Plate 6.1. SEM image of clean muscovite from sample 5378.



Plate 6.2. SEM image of fine-grained muscovite (intermediate gray) intergrown with quartz (black) and sulphides (white) in carbonate hosted manto style mineralization. Sample 4448.

Sample 5378 is white mica from a quartz-sulphide vein hosted in metasedimentary rocks of the Shamrock Zone. Plate 6.1 is an SEM image of a mica crystal from sample 5378. Average grain size is >500 microns. SEM observations showed that the mineral separate consists of clean white mica.

Sample 5378 (Figure 6.1) yielded a very flat plateau at 108 +/-0.3 Ma, with no evidence for significant argon loss or excess. This plateau age is interpreted as the age of crystallization of the mica.

6.2.2 $^{40}\text{Ar}/^{39}\text{Ar}$ age of mica from a manto style orebody

Sample 4448 consists of black, fine-grained mica intergrown with sulphides from a manto style orebody in the Lab Zone. Plate 6.2 is an SEM image of micas separated for $^{40}\text{Ar}/^{39}\text{Ar}$ analysis. Average grain size is <100 microns. SEM observations showed that the micas are finely intergrown with sulphides and quartz. The mica separate was impure.

The age spectrum of sample 4448 (Figure 6.2) is complex. An intermediate saddle/plateau centered at 125.3 +/- 0.5 Ma corresponds to 35% of argon released during step heating. Higher temperature fractions ascend to older ages, reaching 221 +/- 2.0 Ma. Lower temperature fractions show some argon loss. The mixed age pattern yielded by sample 4448 requires careful interpretation. The 125 Ma plateau/saddle can be interpreted in three ways: a) 125.3 +/-0.5 Ma represents the age of formation of metamorphic micas during D_2 ; b) 125.3 +/-0.5 Ma represents the minimum age of formation of metamorphic micas, and minimum age of D_2 ; c) 125.3 +/-0.5 Ma represents the age of formation of hydrothermal micas, and hence the age of mineralization. Typically in this type of spectra, climbing ages represent an inherited component, and the maximum age of the highest temperature fraction is significantly younger than the true age of the inherited component.

Three lines of evidence suggest that neither 125 Ma or 221 Ma represent the age of mineralization.

- a) Field relations suggest that limestone hosted manto-style and metasedimentary rock hosted quartz-sulphide vein mineralization were emplaced along the same set of structures (D_4 normal faults), and were not subsequently deformed.
- b) Textures observed by optical microscopy suggest that the micas may be residual, and not a product of the mineralizing event. Similar, but less concentrated micas occur in unaltered and unmineralized carbonate rocks, especially along stylolites.
- c) Neither 125 Ma or 221 Ma coincide with known ages of emplacement of magmatic rocks that could drive hydrothermal activity in this area.

6.3 Pb isotopic data

The principal objective of this portion of the study was to use Pb isotopes to determine if carbonate hosted mantos, the associated Fe-silicate alteration zones, metasedimentary rock hosted quartz-sulphide veins (Shamrock Zone), and Pb-Ag veins of the Iona Silver Mine area have a similar Pb isotopic signature and may therefore share the same metal source. Lead isotopic composition for samples from Mississippian (?) dykes and from unaltered carbonate rock were also measured and plotted with those from sulphide ore. Calculations of secondary isochrons were carried out to investigate the potential of carbonate rocks of unit 1d (approximate age of 550 Ma), and local basement rocks (assumed age of 1.85 Ga) as the major Pb isotope (and metal) source.

Lead isotopes are a valuable geochemical tracer for determining metal sources of ore deposits, as they record the U/Pb and Th/U ratios of the source at the time when metals were extracted and deposited in sulphide minerals. Lead isotopic compositions from syngenetic shale-hosted (SEDEX-type) deposits have been used to construct model growth curves for the upper and lower crust, that are specific to the tectonostratigraphic terrane which hosts those deposits. Growth

curves constructed using Pb isotopic compositions of shale hosted syngenetic base metal (SEDEX) deposits with known ages can be subsequently used to determine approximate Pb isotope model ages of SEDEX deposits of unknown age in a given terrane. The "shale curve" of Godwin and Sinclair (1982), which is constructed specifically for the miogeocline of western North America in western Canada, is one of the best calibrated model growth curves for the upper crust. Use of the "shale curve" is restricted to the North American miogeocline, however, and an error of at least +/- 50 Ma should be applied to its model ages (Mortensen, 1998).

Epigenetic deposits, generally have Pb isotopic compositions that represent a mixture of two or more reservoirs. For many magmatic-hydrothermal deposits, one reservoir is a magmatic source, and other reservoirs are the various rock units through which magma and/or hydrothermal fluids passed prior to deposition of sulphide minerals. Because of this complex relationship between Pb isotopic compositions of mineralizing fluids and wallrock, single model growth curves cannot be used to determine the age of epigenetic ore deposits. Mixing line isochrons have been used to estimate the age of epigenetic deposits based on mixing of Pb isotopes from two sources (e.g., Andrew et al., 1984). The "Bluebell curve" of Andrew et al. (1984) was interpreted to represent an approximation of Pb isotopic evolution in the lower crust. The "Bluebell curve" has been used in conjunction with the "shale curve" to represent mixing of lead from an upper and a lower crustal source, and thus determine an approximate age for the mineralization.

Indirect dating using Pb isotopes is possible if the source of Pb isotopes is known, and the age of this source can be determined by an independent method (e.g., $^{40}\text{Ar}/^{39}\text{Ar}$, U-Pb). For instance, the age of a pluton that has similar Pb isotopic composition to that of the ore minerals and is in close spatial association to the mineralization is likely to represent the age of the mineral deposit.

6.3.1 Techniques

Lead isotope measurements were carried out on a modified VG54R thermal ionization mass spectrometer. Samples were run at temperatures of 1200 to 1300° C using the silica-gel phosphoric acid technique (Childe, 1997). Replicate analyses of National Bureau of Standards sample NBS-981 and blanks show a reproducibility of sample analyses of about 0.03 percent at one standard deviation.

Minerals analyzed include pyrite, pyrrhotite, arsenopyrite, chalcopyrite, galena, marcasite, and sphalerite. Analytical procedures for sulphide dissolution and trace Pb separation are reported in Appendix E. Different sulphide minerals were run from three samples and these data may be used to compare Pb isotopic ratios within different sulphide species.

6.3.2 Pb isotopic composition of samples from the Ketza River deposit

Lead isotopic compositions were determined for 33 sulphide samples from the carbonate hosted mantos and Fe-silicate zones, and quartz-sulphide veins hosted in metasedimentary rocks. Two sulphide samples from Mississippian(?) dykes outside the map area, and six samples of fresh and apparently unaltered carbonate rock were analyzed, and their trace Pb isotopic composition is compared with those of the ore sulphides. Table 6.1 shows the common lead data for sulphides and carbonates analyzed for this study. Analyses of marcasite (sample 5408) yielded significantly more radiogenic values than pyrrhotite from the same sample. Textural relationships show that marcasite is the latest sulphide phase, and it is interpreted to be a late stage of the mineralizing event, possibly containing Pb from a separate source from that of the other sulphides.

Table 6.2 shows Pb isotopic data from a suite of samples from the Iona Silver Mine area (outside the study area) reported by Godwin et al. (1982). Figure 6.3 shows the location of samples collected within the map area, and Figure 6.4 shows the approximate location of samples from the Iona Silver deposit area. Figures 6.5 and 6.6 are plots of Pb isotopic composition and % error

Table 6.1. Common lead data for sulphides and carbonate rock. Absolute errors quoted. Values are corrected for instrument fractionation by normalization based on replicate analyses of standard NBS-981. Mineral abbreviations: py=pyrite; asp=arsenopyrite; po=pyrrhotite; gn=galena; cp=chalcopyrite; mc=marcasite; sp=sphalerite; cb=carbonate.

sample	ore type	mineral	blocks	206/204Pb error	207/204Pb error	208/204Pb error	207/206Pb error	208/206Pb error
518@53.8	whole rock	cb	5	26.286 0.019	15.894 0.011	38.253 0.023	0.605 0.016	1.455 0.012
518@58.3	whole rock	cb	4	26.704 0.090	16.114 0.090	38.810 0.091	0.603 0.010	1.453 0.005
AF109	whole rock	cb	4	20.009 0.026	15.762 0.019	39.269 0.027	0.788 0.018	1.963 0.006
AF243	whole rock	cb	4	19.118 0.085	15.751 0.085	39.580 0.085	0.824 0.006	2.070 0.006
AF261	whole rock	cb	4	19.127 0.004	15.766 0.003	39.577 0.004	0.824 0.002	2.069 0.002
BX3	whole rock	cb	6	19.823 0.013	15.776 0.011	39.322 0.015	0.796 0.006	1.984 0.007
4432	manto	py	9	19.574 0.008	15.787 0.008	39.904 0.009	0.807 0.002	2.039 0.004
4435	manto	gn	4	19.636 0.004	15.768 0.003	39.790 0.006	0.803 0.003	2.026 0.004
4448	manto	cp,py	5	20.156 0.790	15.833 0.788	40.537 0.791	0.790 0.078	2.011 0.050
5331	manto	po	5	21.162 0.147	15.953 0.148	39.833 0.148	0.754 0.013	1.882 0.014
5331	manto	po	5	21.024 0.047	15.842 0.044	39.490 0.050	0.754 0.017	1.878 0.018
5354	manto	po	5	19.610 0.221	15.734 0.215	39.832 0.236	0.802 0.054	2.031 0.080
4448b	manto	cp,py	5	19.475 0.170	15.652 0.165	39.396 0.180	0.804 0.037	2.023 0.060
4448c	manto	cp,py	5	19.806 0.206	15.923 0.203	40.096 0.207	0.804 0.037	2.024 0.015
AF-46-A	manto	py	7	20.002 0.157	15.866 0.144	39.703 0.163	0.793 0.062	1.985 0.045
Oxo-1	manto	gn	5	19.525 0.004	15.740 0.003	39.731 0.004	0.806 0.002	2.035 0.002
Oxo-4	manto	gn	4	19.541 0.007	15.753 0.005	39.777 0.009	0.806 0.005	2.036 0.006
oxo-low	manto	po	8	19.504 0.034	15.834 0.030	39.159 0.036	0.802 0.017	2.008 0.011
sulph_2	manto	asp	7	19.802 0.005	15.736 0.005	39.652 0.006	0.803 0.003	2.023 0.003
sulph-2	manto	po	5	19.532 0.044	15.579 0.043	39.066 0.045	0.798 0.009	2.000 0.008
SN DK	Miss intr	py,po	5	19.737 0.007	15.746 0.006	40.252 0.008	0.798 0.002	2.039 0.005
91	Miss intr	py,po	5	18.649 0.269	15.428 0.266	38.111 0.273	0.827 0.042	2.044 0.042
4442	Fe-silicate	asp	9	19.606 0.045	15.747 0.044	39.747 0.045	0.803 0.008	2.027 0.006
537@91.7	Fe-silicate	po	7	19.567 0.034	15.696 0.033	39.428 0.037	0.802 0.008	2.015 0.014
542@20.36	Fe-silicate	po,asp	8	19.681 0.018	15.764 0.011	39.845 0.021	0.801 0.014	2.025 0.012
6538 mt sk	Fe-silicate	po	7	19.838 0.270	15.641 0.268	38.766 0.273	0.788 0.029	1.954 0.042
5138	vein	asp	4	19.246 0.074	15.466 0.072	38.933 0.074	0.804 0.014	2.023 0.009
5317	vein	asp	9	19.717 0.132	15.857 0.131	40.024 0.132	0.804 0.010	2.030 0.008
5320	vein	asp	3	19.539 0.050	15.771 0.049	39.860 0.055	0.807 0.012	2.040 0.022
5372	vein	asp	4	19.619 0.031	15.795 0.028	39.904 0.033	0.805 0.013	2.034 0.011
5378	vein	gn	4	19.561 0.010	15.739 0.005	39.790 0.014	0.805 0.009	2.034 0.009
5379	vein	asp	6	19.615 0.016	15.789 0.014	39.855 0.018	0.805 0.008	2.032 0.007
5381	vein	gn	4	19.632 0.004	15.757 0.003	39.767 0.004	0.803 0.002	2.026 0.002
5385	vein	gn	4	19.629 0.005	15.763 0.005	39.781 0.005	0.803 0.001	2.027 0.002
5389	vein	py	5	19.611 0.028	15.759 0.017	39.752 0.037	0.804 0.022	2.027 0.024
2579@76.1	vein	mc	6	20.309 0.104	15.782 0.104	41.729 0.106	0.777 0.010	2.055 0.020
3576@99	vein	po	7	19.699 0.172	15.807 0.170	40.075 0.173	0.802 0.025	2.034 0.022
4579@76.1	vein	po	8	19.478 0.073	15.633 0.070	39.746 0.074	0.803 0.019	2.041 0.016
576@99	vein	mc	7	19.774 0.041	15.828 0.039	40.147 0.043	0.800 0.012	2.030 0.012
579@76.1	vein	mc	6	20.314 0.090	15.802 0.090	41.804 0.090	0.778 0.008	2.058 0.005
582@107.8	vein	asp	6	19.635 0.046	15.789 0.046	39.889 0.047	0.804 0.008	2.032 0.007
F VN_E	vein	gn	4	19.558 0.032	15.760 0.024	39.687 0.039	0.806 0.021	2.029 0.022
Fred's vn	vein	gn	8	19.585 0.008	15.773 0.006	39.803 0.009	0.805 0.005	2.032 0.003
575@46.5	vein	po	5	19.493 0.264	15.723 0.094	39.606 0.288	0.807 0.247	2.032 0.115

Table 6.2. UBC lead isotopic composition data for galena from the Iona Silver mine (Godwin et al., 1982). Values are corrected for Instrument fractionation by normalization based on replicate analyses of standard NBS-981. Percent errors in small print beneath the isotopic ratios.

sample #	Pb206/204	Pb207/204	Pb208/204	Pb207/206	Pb208/206
10081-001	19.502 0.018	15.731 0.028	39.765 0.076	0.80663	2.03902
10081-001	19.392 0.037	15.745 0.044	39.873 0.156	0.81193	2.05616
10081-003	19.516 0.020	15.74 0.030	39.694 0.111	0.80652	2.03392
10081-004	19.478 0.018	15.725 0.028	39.621 0.079	0.80732	2.03414
10081-005	19.481 0.021	15.729 0.025	39.673 0.087	0.8074	2.0365
10081-006	19.451 0.018	15.718 0.028	39.679 0.079	0.80808	2.03995
10081-007	19.468 0.019	15.726 0.031	39.77 0.111	0.80779	2.04284
10081-008	19.469 0.018	15.71 0.024	39.655 0.079	0.80692	2.03683
10081-009	19.482 0.016	15.726 0.030	39.632 0.052	0.80721	2.03429
10081-010	19.468 0.021	15.756 0.028	39.7 0.079	0.80933	2.03924
10081-011!	19.366 0.012	15.618 0.027	39.432 0.059	0.80646	2.03615
10081-012	19.44 0.019	15.733 0.022	39.636 0.079	0.80931	2.03889

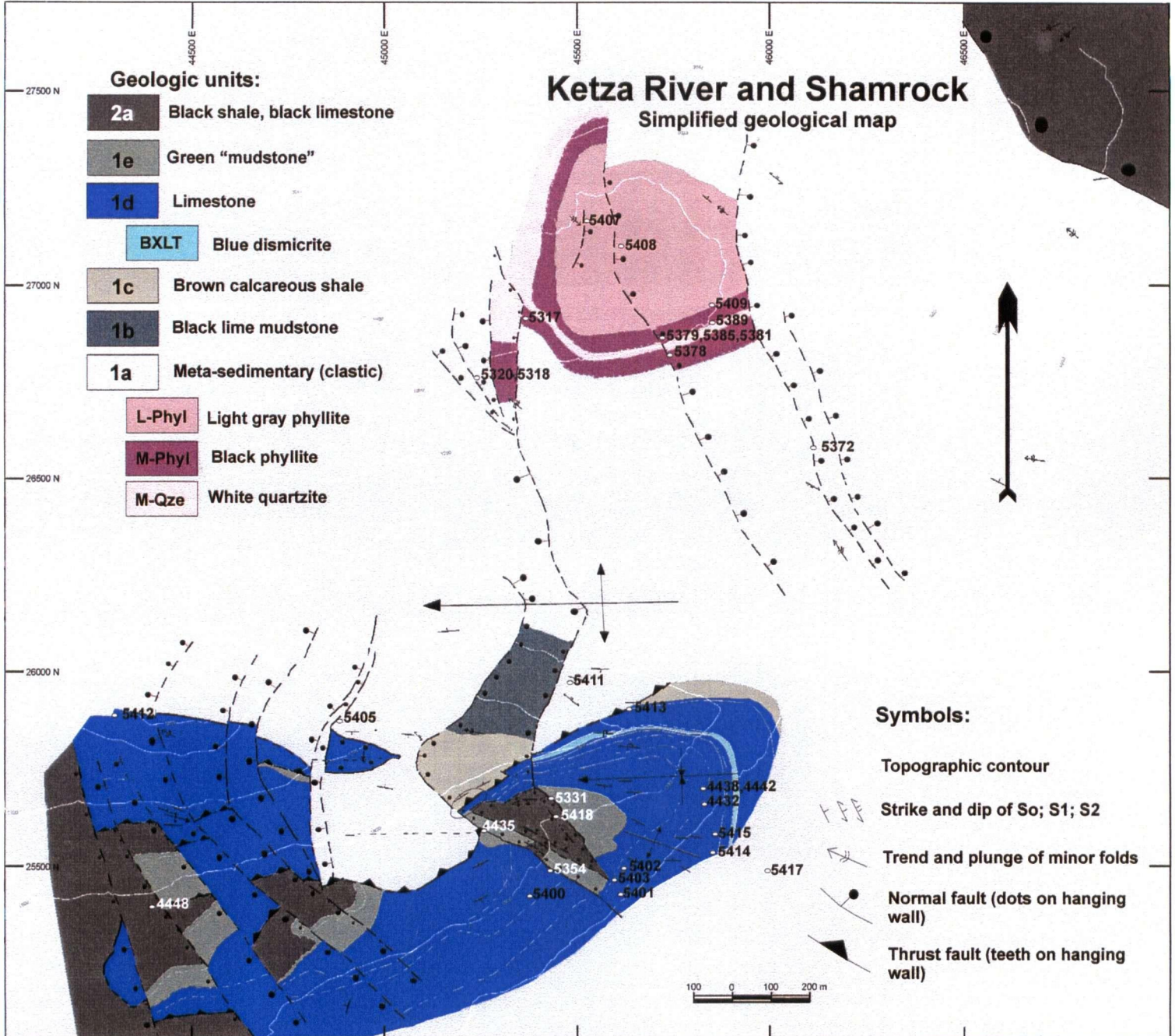


Figure 6.3. Geological map of Ketzá River and Shamrock zone, showing the surface projection of Pb-Pb sample locations.

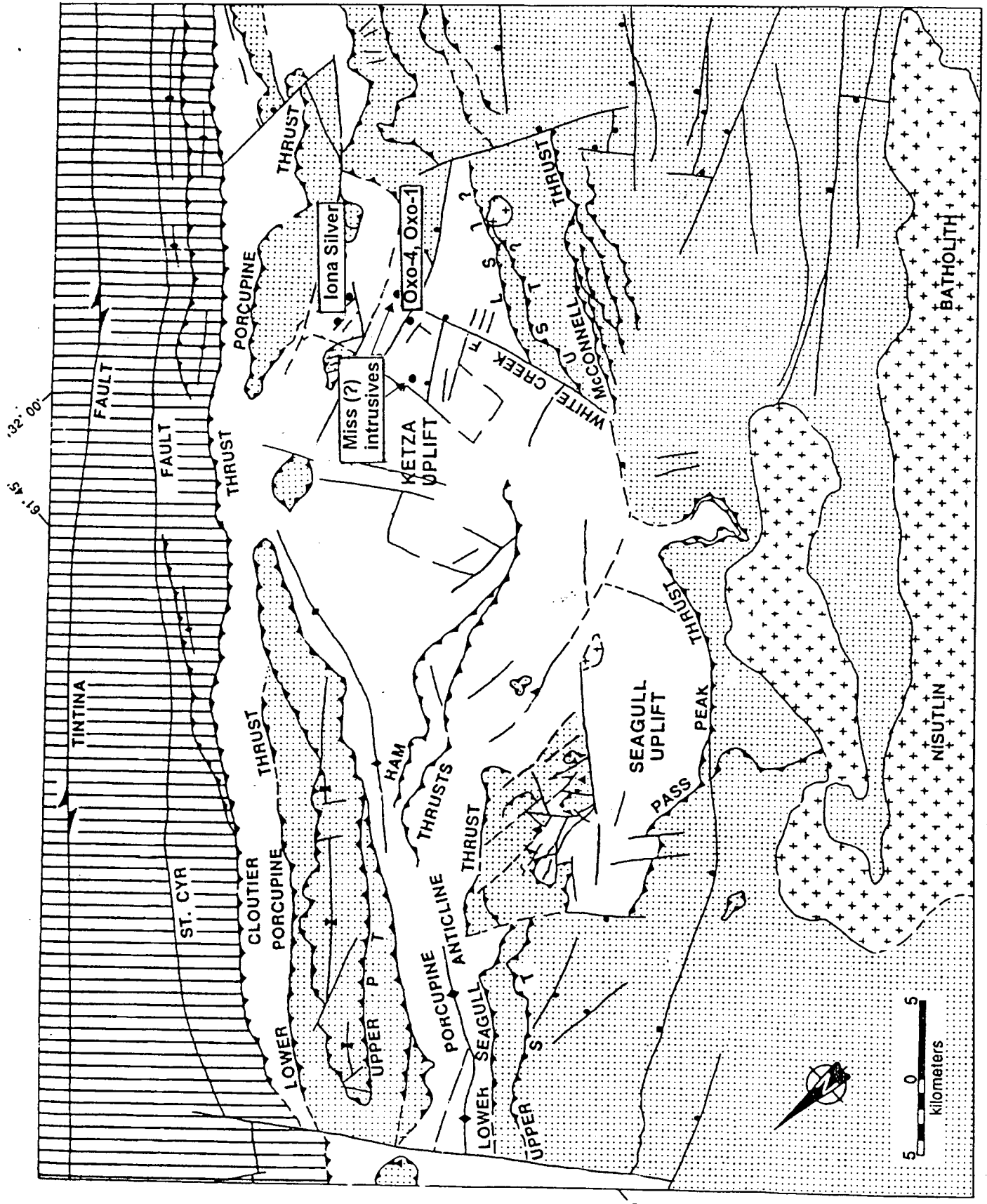


Figure 6.4. Geological map of the Ketzal-Seagull uplift (Abbott, 1986) showing approximate location of Pb-Pb samples collected outside the map area.

for samples analysed during this study and samples from Godwin et al. (1982) (errors plotted when available). The "shale curve" of Godwin and Sinclair (1982) is plotted for reference.

6.3.3 Discussion

At elevated temperatures of hydrothermal metal deposition, there is relatively rapid isotopic exchange between fluids and host rock, resulting in a complex relationship between isotopic composition of fluid and rocks (Farmer and DePaolo, 1997). Such high temperature exchange is not to be expected in the Ketz River ores, however, arsenopyrite geothermometry and fluid inclusions (see discussion in previous section) studies suggest that ore deposition took place at temperatures lower than 330° C.

The data presented in Figures 6.5 and 6.6 shows an evolution from radiogenic and relatively tightly clustered values for Pb-Ag (Iona Silver) and quartz-sulphide (Shamrock) veins to more radiogenic and variable values in carbonate hosted Fe-silicate alteration zones and manto samples. The overlap of lead isotopic composition between veins, Fe-silicate alteration zones, and manto mineralization in the Ketz River area suggests that metals in the different mineralization styles were derived from similar sources. Tightly clustered isotopic compositions from vein samples either reflect the isotopic composition of a single metal source, or are a result of well homogenized Pb derived from multiple reservoirs. The broad spread of isotopic values of carbonate hosted ores is likely to be a result of slow reaction rates involved in the replacement of limestone by sulphides, allowing for greater isotopic exchange between the mineralizing fluids and carbonate host rocks of different uranium and thorium composition.

Trace Pb isotopic compositions from carbonate rocks are scattered. The two samples with less radiogenic ratios are from CCLT facies, whereas the two samples with more radiogenic ratios are from MSLT and BXLT facies. This spread may be due to hydrothermal or metamorphic effects that are not visible, or to variable Pb isotopic compositions in different limestone facies. As

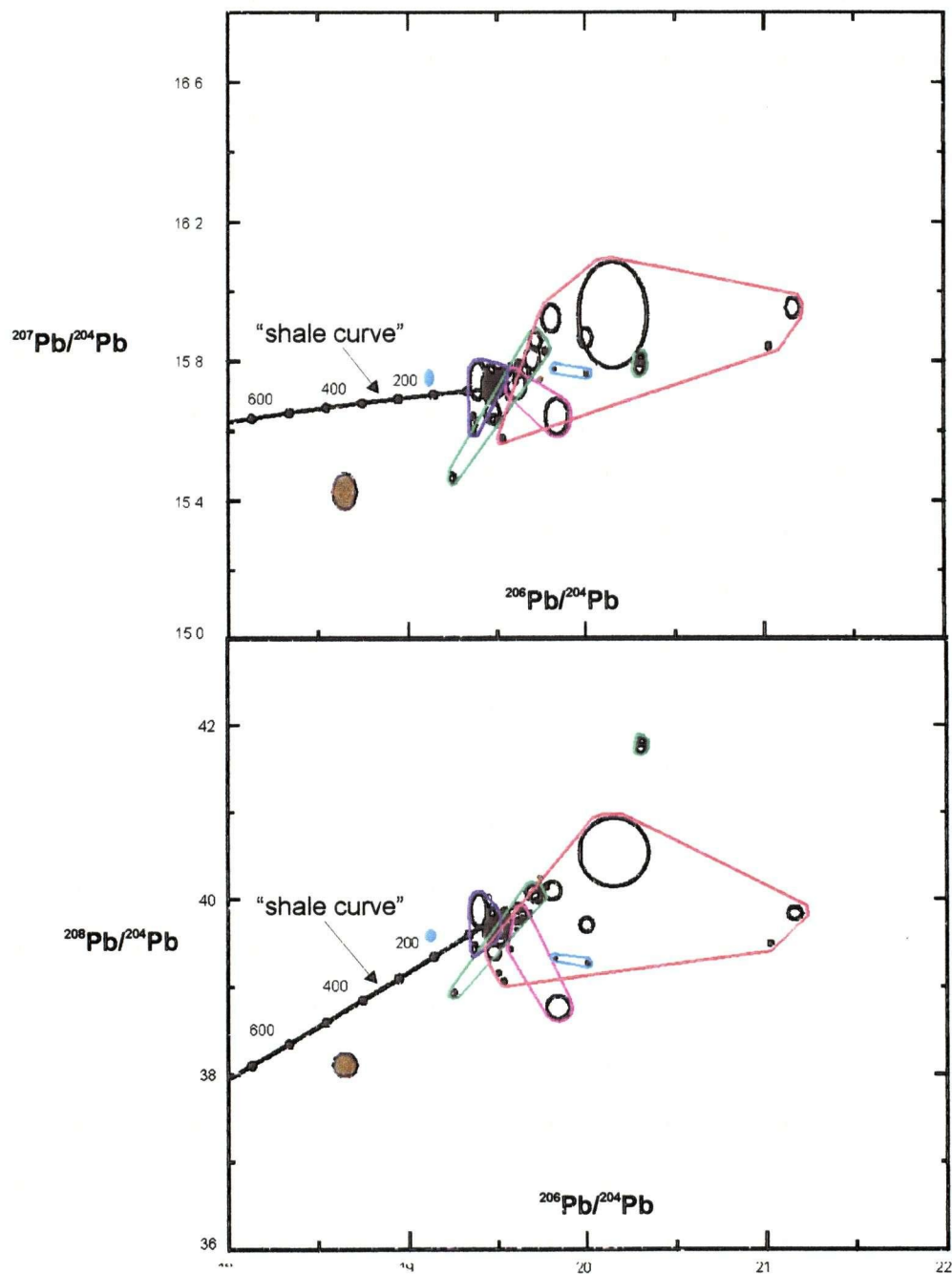


Figure 6.5. Plots of $^{207}\text{Pb}/^{204}\text{Pb}$ versus $^{206}\text{Pb}/^{204}\text{Pb}$ and $^{208}\text{Pb}/^{204}\text{Pb}$ versus $^{206}\text{Pb}/^{204}\text{Pb}$ for sulphides from carbonate hosted mantos (red) and Fe-silicate alteration (magenta), metasedimentary rock hosted quartz-sulphide veins (green) and Ag-Pb-rich veins (blue), Mississippian (?) intrusives (brown), and carbonate host rock (cyan). Size of ellipses corresponds to analytical errors.

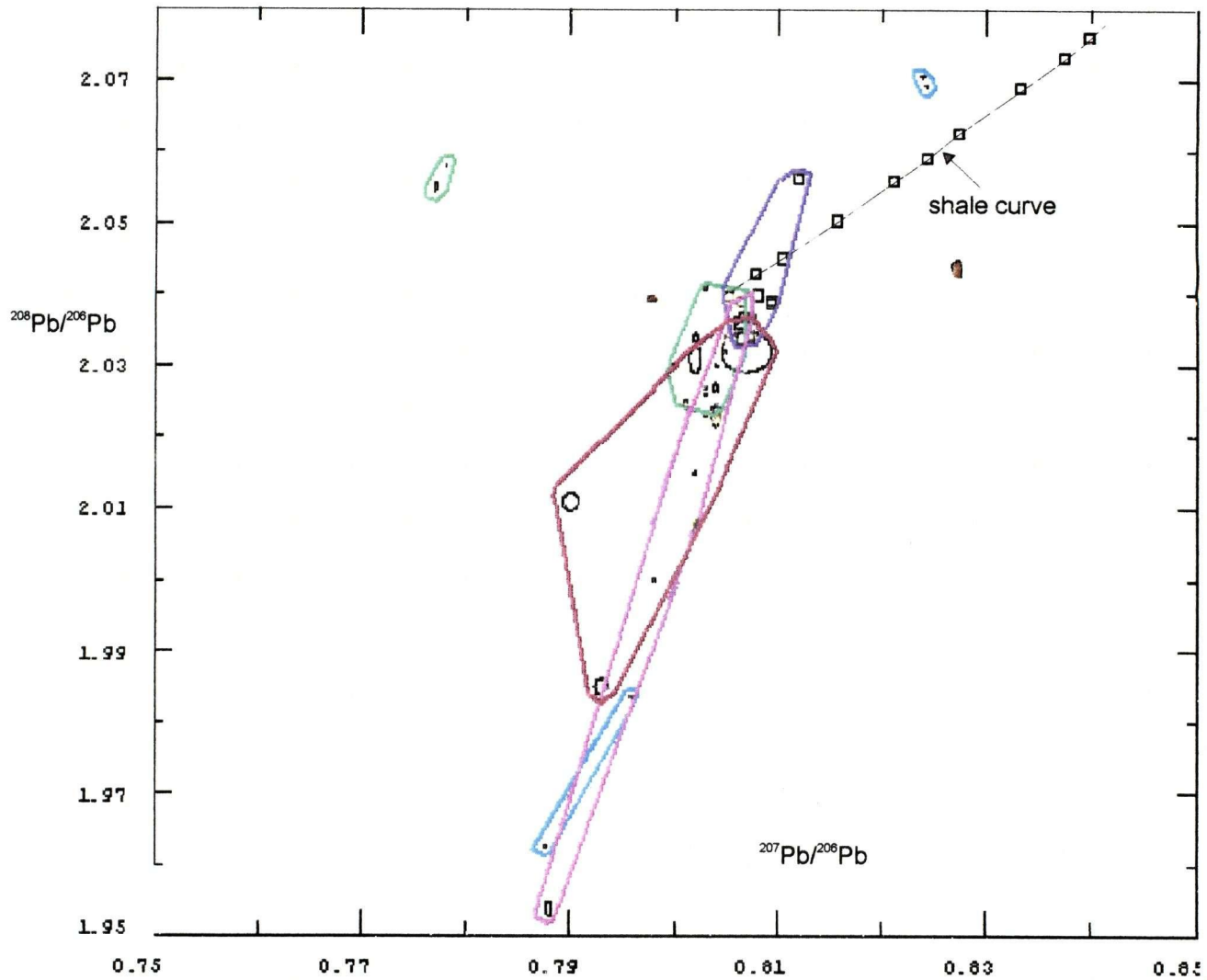


Figure 6.6. Plot of $^{208}\text{Pb}/^{206}\text{Pb}$ versus $^{207}\text{Pb}/^{206}\text{Pb}$ for sulphides from carbonate hosted mantos (red) and Fe-silicate alteration (magenta), metasedimentary rock hosted quartz-sulphide veins (green) and Pb-Ag-rich veins (blue), and Mississippian (?) Intrusives (brown). Trace lead from host carbonate in cyan.

different limestone facies are differently affected by hydrothermal and metamorphic effects, both factors may be important.

All galena and trace Pb analyses correspond to future ages, when compared against the shale curve of Godwin and Sinclair (1982). This suggests a model lead source enriched in ^{238}U . Calculations of μ values for a secondary isochron starting at $t_1=550$ Ma (approximate age of Early Cambrian archeocyathid bearing limestone that hosts manto and Fe-silicate styles of mineralization) yielded an unreasonably high average calculated μ value (see Appendix F) of 17.33. High μ values are to be expected in the ancient North America miogeocline, as demonstrated by the high μ value of the "shale curve", but this anomalously high value is indicative of significant Pb evolution at high μ values before 550 Ma, suggesting that the Early Cambrian limestone is not the exclusive source of Pb in the Ketz River ores. Calculations of average μ value for a Pb evolution curve starting at $t_1=1.85$ Ga (best approximation to the sedimentary basement age) yielded an average μ of 12.89, which is more realistic. However, a ~ 100 Ma isochron fit to the data array was not possible, implying that basement rocks are also not the exclusive reservoir from which Pb of the Ketz River ores was extracted.

Upper crust, lower crust, and mantle model Pb growth curves were plotted against trace Pb isotopic ratios from sulphide minerals from the Ketz River ores, to investigate the possibility that the data spread may represent simple mixing of two Pb sources. Figures 6.7 and 6.8 are plots of $^{207}\text{Pb}/^{204}\text{Pb}$ against $^{206}\text{Pb}/^{204}\text{Pb}$ for trace Pb in samples from mantos, Fe-silicate alteration, quartz-sulphide veins (Shamrock zone), and Ag-Pb-rich veins (Iona Silver). In Figure 6.7, the shale curve of Godwin and Sinclair (1982) and the lower crust and mantle curves of Zartman and Doe (1981) are used to construct a mixing line isochron at approximately 100 Ma. Data from the various styles of mineralization in the Ketz River area do not correspond to the 100 Ma mixing line isochron. Figure 6.8 shows the shale curve of Godwin and Sinclair (1982) and a curve of high μ as calculated in Appendix F. Pb compositions of ore minerals from Ketz River do not correspond to simple mixing line isochrons between these two curves.

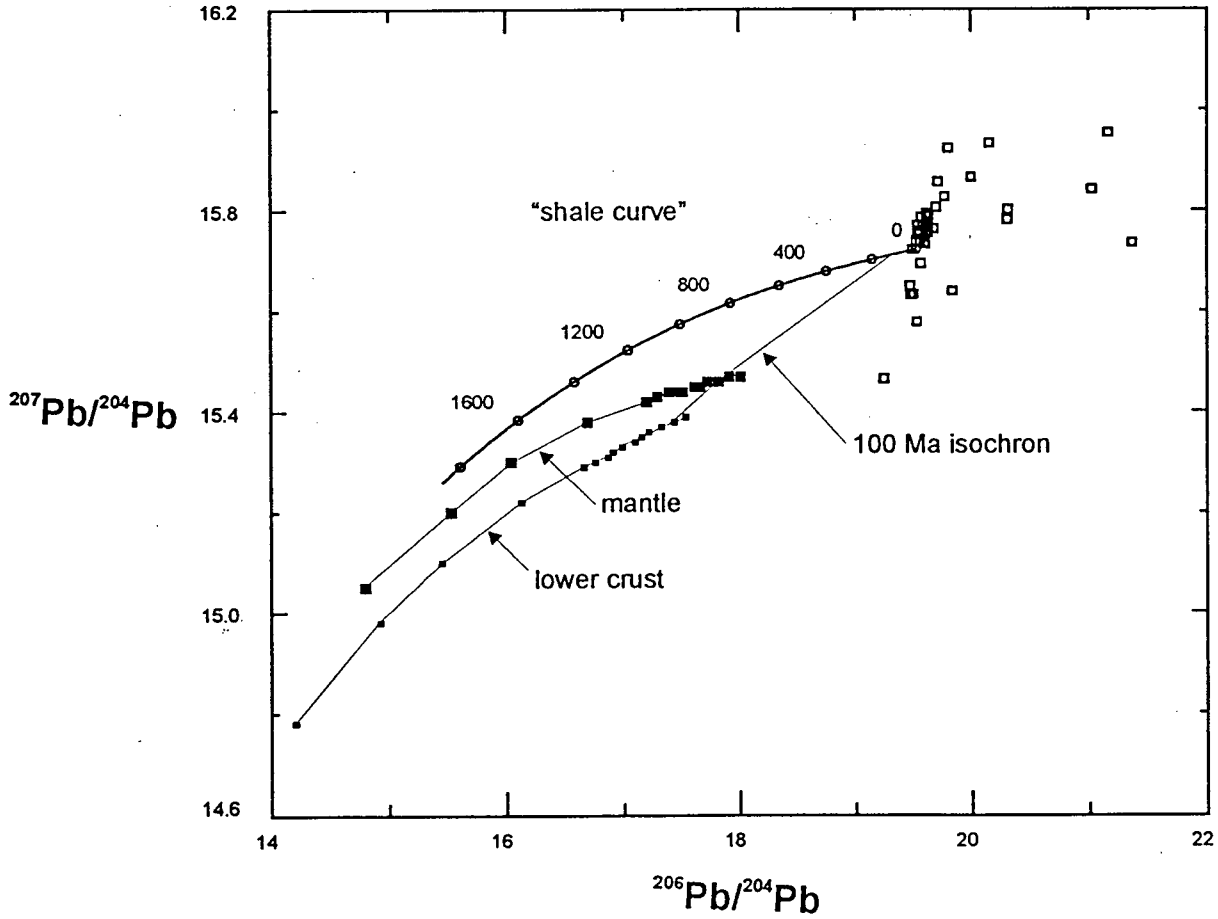


Figure 6.7 Lead isotopic ratios of all sulphide mineralization plotted against a ~100 Ma isochron between model growth curves for the lower crust and mantle (data from Zartman and Doe, 1981), and the shale curve (Godwin and Sinclair, 1982). Isotopic ratios from the Ketz River ores do not plot along the 100 Ma isochron.

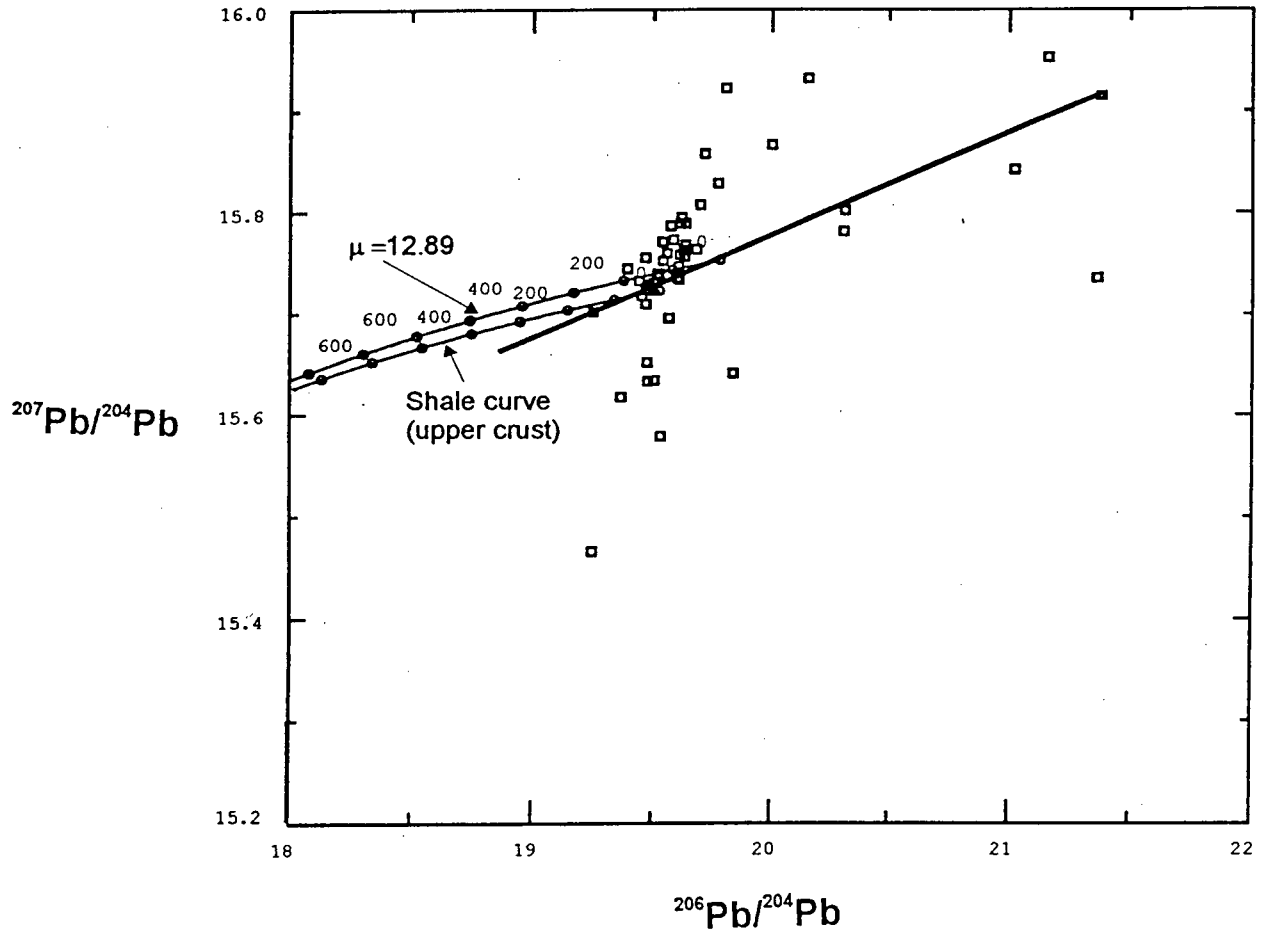


Figure 6.8. A regression line through all data from the Ketz River ores does not correspond to a simple mixing line between model growth curves for the upper crust ("shale curve" of Godwin and Sinclair, 1982) and a curve with higher mu value (mu value calculated based on a 2.2 Ga basement source).

The spread displayed by the isotopic compositions of the various ores is best explained in terms of mixing between Pb isotopes from a likely magmatic source, hydrothermal fluids, and various reservoirs represented by different limestone facies and other rock units through which the mineralizing fluids migrated.

7 SUMMARY AND DISCUSSION

7.1 Introduction

The principal reason why I investigated the Ketz River deposit is that in spite of this deposit being the site of extensive mineral exploration, structural and stratigraphic controls on the location of orebodies and the mechanism driving hydrothermal activity were poorly understood. The results of this research provide good constraints on structural and stratigraphic controls. The mechanism driving hydrothermal activity, however, remains unresolved, but a significant amount of evidence suggests that a mid-Cretaceous pluton is buried underneath the Ketz River deposit.

Ketz River Mine produced 97,976 troy ounces of gold (Cathro, 1992). Current resources of oxide and sulphide ore from manto style mineralization in the Ketz River deposit are estimated at 230,000 metric tonnes with 10.9 g/t Au (R. Stroshein, pers. comm., 1997). The deposit contains manto and Fe-silicate mineralization in Early Cambrian archeocyathid-bearing limestones, and quartz-sulphide vein and stockwork mineralization hosted in Late Proterozoic to Early Cambrian metasedimentary (clastic) rocks. Ketz-Seagull district is underlain mainly by early to mid Paleozoic rocks, and has been interpreted as a domal uplift above a Cretaceous intrusion (Abbott, 1986). No igneous rocks have been identified this far near the orebodies. The igneous rocks closest in age in the area are Mississippian (?) dykes and stock, that show evidence of pre-dating the mineralization, and a small quartz-monzonite stock approximately 12 km southeast of the mine.

7.2 Stratigraphy

Four marker beds are mapped in the Late Proterozoic to early Cambrian metasedimentary rock sequence (unit 1a): M-QZE₁, M-PHYL, M-QZE₂, LTG-PHYL. M-PHYL is the most conspicuous of the marker beds in unit 1a, due to its dark gray to black colour and intense phyllitic sheen.

Early Cambrian archeocyathid-bearing limestones (unit 1d) are subdivided into six distinct mappable facies (from oldest to youngest): WBN, BXLT, MSLT₁, BSLT, MSLT₂, FSLT. Amongst these facies BXLT, MSLT₁, and WBN are the most important ore hosts. BXLT is the most distinctive facies in outcrop and drill core, because of its coarse crystalline character, light blue colour, and well developed joint pattern. Well developed joints and fractures enhanced porosity of the BXLT horizon, making it the most favourable ore host. MSLT₁ is recognized by its oolitic character. Oolitic porosity makes MSLT₁ the second most favourable ore host. Hydrothermal dolomitization of ooid cores within few metres of ore is the only form of alteration associated with the Ketz River mantos, and is most conspicuous in MSLT₁. WBN is a massive, medium to coarse crystalline facies, with moderate fracture porosity. It hosts the deepest mantos.

7.3 Structural geology

Five phases of deformation are recognized and their relative ages are well constrained. The first three phases of deformation can be correlated to deformation mapped elsewhere in the Pelly Mountains, whereas the last two are local.

Two phases of folding (F₁ and F₂) have E-W to WNW trending axes and well developed, penetrative foliations. Folding resulted in enhanced fracture porosity of favourable stratigraphic limestone horizons.

Folding was followed by thrust faulting. From regional analogies and from relationships immediately outside the map area, thrusts are interpreted to have NNE-directed movement. Thrust faults appear to have formed an impermeable layer to meteoric fluids, and manto orebodies beneath thrust faults that have not been eroded are generally unoxidized.

An extensional event post-dated thrust faulting. This extensional event produced horst and graben structures, with the greatest uplift in the Shamrock Zone. High angle planar and listric normal faults are associated with vein and manto styles of mineralization.

The latest deformation event produced only one thrust fault that truncates parts of one manto oxide orebody, without producing any penetrative structures.

7.4 Mineralization and alteration

Three styles of mineralization occur in the Ketz River map area: massive sulphide and oxidized mantos, Fe-silicate alteration, and quartz-sulphide vein/stockwork. The different styles of mineralization have similar sulphide mineralogy, and contain native bismuth. A fourth style occurs outside the map area: Pb-Ag veins. Sulphide mantos and veins are undeformed and unmetamorphosed.

Major and trace opaque mineralogy in mantos, Fe-silicate alteration, and quartz-sulphide veins consists of (in order of decreasing abundance): pyrrhotite, pyrite, arsenopyrite, marcasite, chalcopyrite, galena, sphalerite, native bismuth, and gold.

The most common forms of alteration associated with manto style mineralization is dolomitization and decalcification. Bleaching, sericitization, and local silicification occur adjacent to quartz-sulphide veins and stockwork.

7.5 Temperature of mineralization

Maximum mineralization temperature estimates from arsenopyrite geothermometry and from fluid inclusion studies by Staveley, (1992) are comparable. Arsenopyrite geothermometry analyses yield low atomic percent arsenic in arsenopyrite crystals from various locations in the deposit,

corresponding to temperatures in the order of 330° C and lower. Limited fluid inclusion homogenization temperatures by Staveley (1992) yield mineralizing temperatures in the order of 280° to 340° C for quartz-sulphide veins.

7.6 Relative and absolute ages of mineralization

Two mica separates were dated by the $^{40}\text{Ar}/^{39}\text{Ar}$ method. Coarse mica from a quartz-sulphide vein yielded a 108 +/- 0.3 Ma plateau age. Mica from a massive sulphide manto yielded a mixed age $^{40}\text{Ar}/^{39}\text{Ar}$ spectrum with a saddle/plateau centred at 125.3 +/- 0.5 Ma, and ascending ages that reach 221 +/- 2.0 Ma. Given that similar micas are found in unmineralized and unaltered limestone, the mixed age spectrum is thought to reflect a residual (metamorphic) origin of the micas, whereas the simple plateau age of 108 +/- 0.3 Ma is interpreted as representing the age of the mineralizing event that produced the different styles of mineralization. A whole-rock K-Ar age of 100 +/- 3 Ma (Cathro, 1982) has uncertain interpretation, and is probably related to Ar loss subsequent to mineralization.

Trace Pb analyses of sulphides from the different mineralization styles plot in overlapping fields, suggesting that they were derived from a common source or sources, and supporting the idea of a single mineralizing event. A wide spread in Pb isotopic ratios in carbonate hosted ores reflects complex isotopic mixing between mineralizing fluids and wallrock, and precludes the use of secondary model growth curves to define possible Pb sources.

7.7 Discussion

7.7.1 Deposit model

Synthesis of field and analytical data allows for the development of a genetic model that encompasses the different styles of mineralization, and speculates on the source of heat, fluids,

and metals for mineralization in the Ketzá River area. Figure 7.1 is a simplified schematic model for the formation of the Ketzá River ores.

In mid-Cretaceous time (approximately 108 Ma), emplacement of a blind intrusion produced doming and uplift of the Ketzá River area. The doming was accommodated by a combination of listric and planar normal faults. A relatively flat, S-dipping fault (Peel Fault) formed, and was followed by the development of a series of NNW-trending normal faults. A collapse graben (Eastern Graben) formed to the west of the most uplifted block. As the buried pluton cooled, hydrothermal fluids ascended using normal faults as major conduits. Once the fluids reached limestone units with enhanced fracture or oolitic porosity, they migrated laterally along D_2 joints and through microfractures. Hydrothermal fluids incorporated and re-concentrated the most insoluble residual minerals, such as mica, altered the composition of the wallrock, and precipitated gold and sulphides at temperatures around 240 to 330° C. Local cataclastic microtextures healed by late stage sulphide and gangue minerals in sulphides deposited along high-angle normal faults suggest that those faults were active at the time of mineralization or immediately later. Manto style deposits consisting predominantly of Fe-sulphides formed in the most porous limestone units. Fe-amphiboles crystallized in alteration zones adjacent to mantos, where the limestone had high clay content. Hydrothermal fluids ascending along normal faults in 1a (silica-rich) lithology dissolved quartz from the country rock and reprecipitated it as veins and stockwork, along with sulphides, Au, and rare mica. Subsequently to mineralization, erosion of parts of pre-mineralization thrust panels allowed meteoric water to penetrate into the limestones and oxidize manto orebodies.

7.7.2 Comparisons with other manto-style deposits

The manto ores at Ketzá River are an example of gold-rich, base metal-poor carbonate replacement ores, whereas most manto style deposits are base metal-rich and gold-poor.

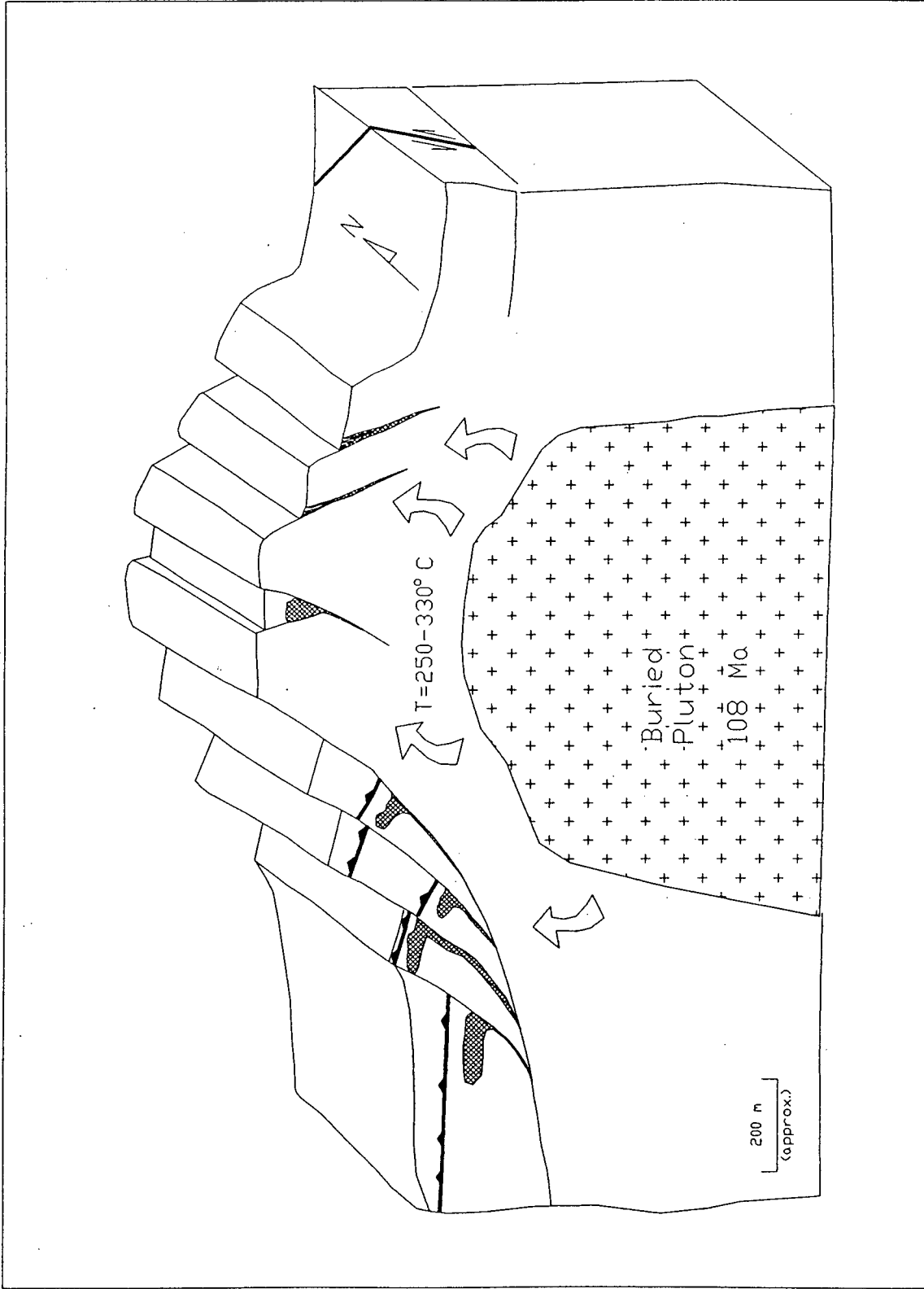


Figure 7.1. Schematic diagram of the interpreted model for the origin of the Ketzal River deposit. The buried pluton is inferred to have been the source of heat, and possibly fluid, metal, and sulphur. Meteoric fluids produced oxidation of mantos where overlying thrust faults were eroded.

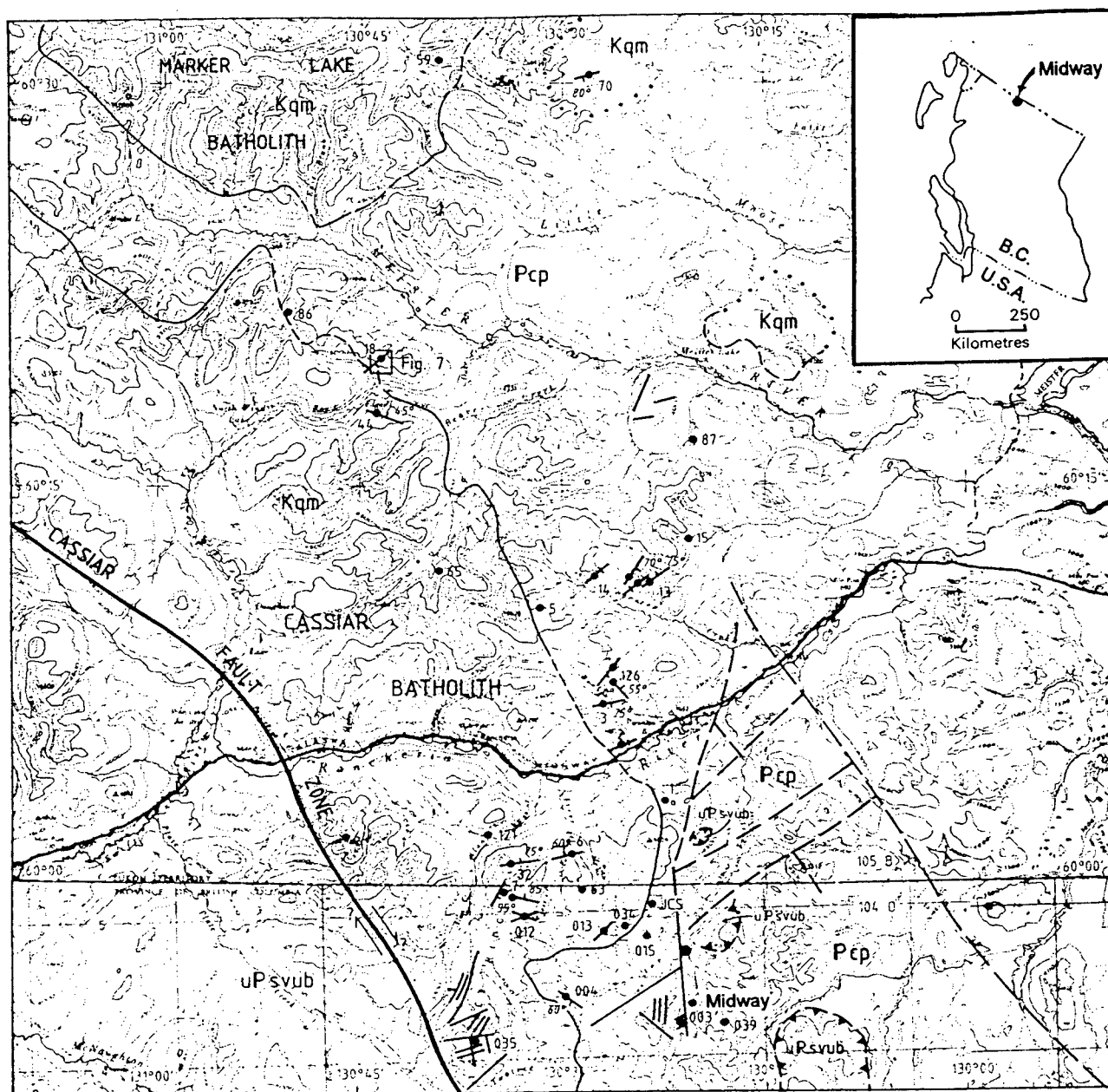
Relatively few carbonate replacement deposits in the North American Cordillera are well studied. Two examples are briefly summarized below.

7.7.2.1 Midway

The Midway silver-lead-zinc manto deposit of the Rancheria District, British Columbia (Figure 7.2), has close similarities to the Ketz River deposit. At Midway, mantos are localized at the upper contact of the mid-Devonian McDame limestone unit with the overlying pelitic (impermeable) Earn Group rocks. The main orebodies are localized along the hinge of an anticline (Bradford, 1987). There are local collapse breccias with open space filling by sulphides, but overall, sulphide orebodies typically show replacement textures. Lewis (1997) stresses that intersections of normal faults and hanging wall deformation control the location of manto orebodies in the Silvertip Zone. Abbott (1986) lists a variety of other base and precious metal occurrences in the Rancheria district, mentioning a few occurrences of Au-rich quartz-sulphide veins that may be similar to those in the Shamrock Zone of Ketz River.

Similarly to Ketz River, no intrusive rocks that could be pointed as the source of metals, fluids, or heat are present at Midway. Bradford (1988) reports four K-Ar analyses from alteration micas, with a wide age range. The two oldest ages (105 +/- 4 Ma, and 97.3 +/- 3.4 Ma) are approximately coincident with the age of emplacement of the Cassiar suite of intrusions. The two younger ages (65.4 +/- 2.3 Ma and 67.1 +/- 2.3 Ma) likely represent thermal overprinting of the K-Ar systematics in fine-grained micas.

Unlike Ketz River, the sulphide mineralogy at Midway is complex. Metal zoning is consistent with that observed in many manto deposits, with higher chalcopyrite and negligible galena content closer to the inferred thermal sources, whereas galena and sulphosalts were deposited away from inferred thermal sources (Bradford, 1988). This zoning pattern is similar to that inferred at Ketz River, where the Iona Silver Pb-Ag veins are interpreted as a distal form of



LEGEND

CRETACEOUS

Kqm Quartz monzonite

UPPER PALEOZOIC

uPsvub Accreted sedimentary, volcanic, and ultramafic rocks

PALEOZOIC AND (?) HADRYNIAN

Pcp Limestone, dolomite, shale, quartzite

5 0 5
kilometres

SYMBOLS

— · · · · Geological contact; defined, approximate, assumed

— — — — Fault, sense of movement unknown; defined, approximate

● — Normal fault; defined, approximate

▲ — Thrust fault, approximate

— — — — Strike-slip fault; defined

● 3 Mineral occurrence

Figure 7.2. Geological map of the Rancheria District and location map of the Midway deposit. Modified from Abbott, 1983.

mineralization that is genetically associated to manto and Fe-silicate mineralization (Cathro, 1992).

7.7.2.2 Central Colorado mineral belt

The Colorado Mineral Belt is a well studied, world class district with abundant precious and base metal mantos and associated styles of mineralization. Figures 7.3 and 7.4 show the geographical location and generalized geology of central Colorado. Mantos replace Early Cambrian to Mississippian limestones and dolomites. Low angle Laramide thrust faults control the location of orebodies (Thompson, 1998).

Unmineralized sections of the Leadville Dolomite in the Leadville, Buckeye Gulch, and Gilman deposits show systematic internal stratigraphy with 15 continuous beds, four of which host mineralization (Beaty, 1990). Three of the preferentially mineralized beds have coarse grain size and porous texture, whereas the fourth bed has abundant paleokarsts.

Monzonitic and granodioritic intrusive rocks are associated with most mineral deposits of the central Colorado mineral belt. K-Ar and Fission track ages of igneous rocks range between 45 and 35 Ma (Bookstrom, 1990). At Gilman, however, no plutonic rocks are exposed. Figure 7.5 is a schematic illustration of the Gilman deposit model, showing a concealed stock inferred to have served as a source of heat, fluid, sulphur, and metals. District-scale metal zoning typically involves high Au grades in close proximity to known intrusive centres. Peripheral veins are base metal rich. Silicification and sanding (dissolution of dolomite matrix, weakening the rock) are the most common forms of hydrothermal alteration in dolostones.

The Ketz River deposit is similar to deposits in the central Colorado mineral belt in terms of structural and stratigraphic controls over manto locations, and in the location of base metal rich

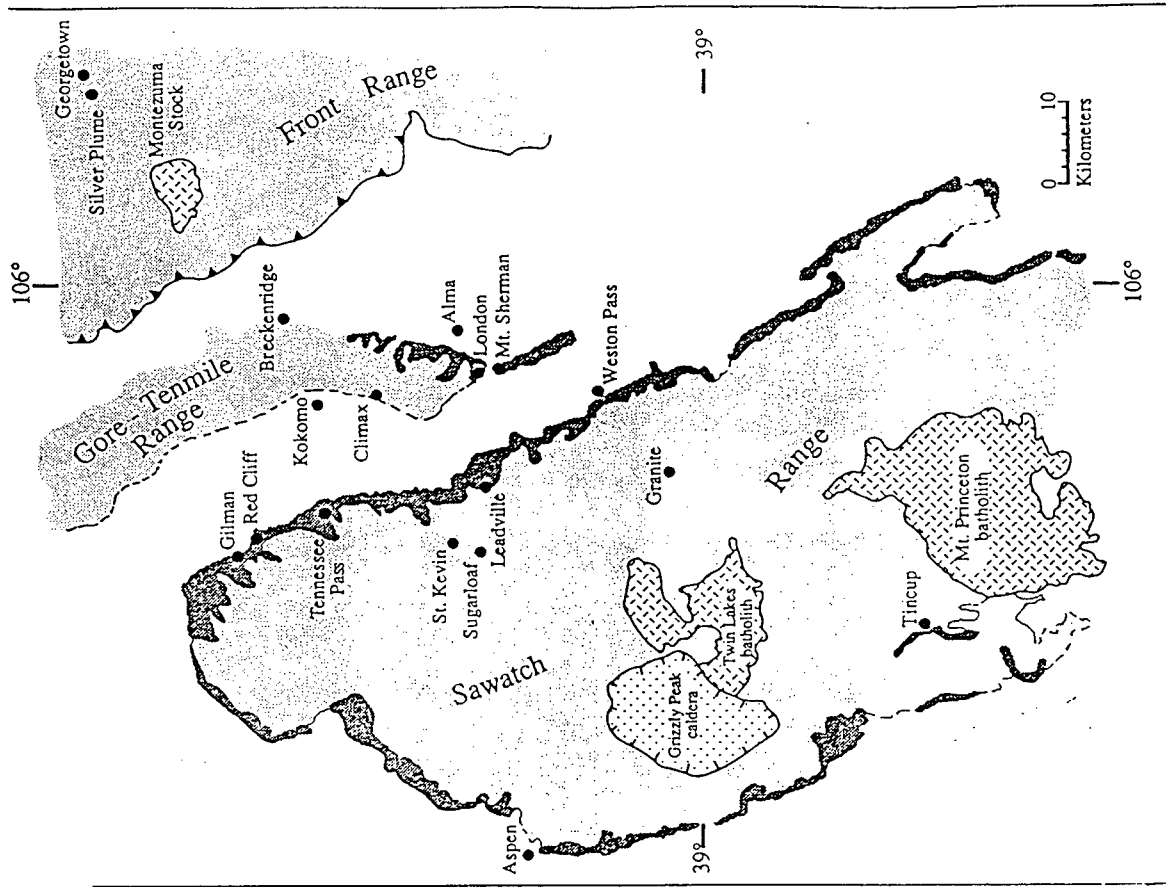


Figure 7.4. Generalized geological map of central Colorado, showing intrusive rocks (hatched), Precambrian rocks (light gray), Cambrian through Mississippian sedimentary rocks (dark gray), and location of deposits. From Beaty et al. (1990).

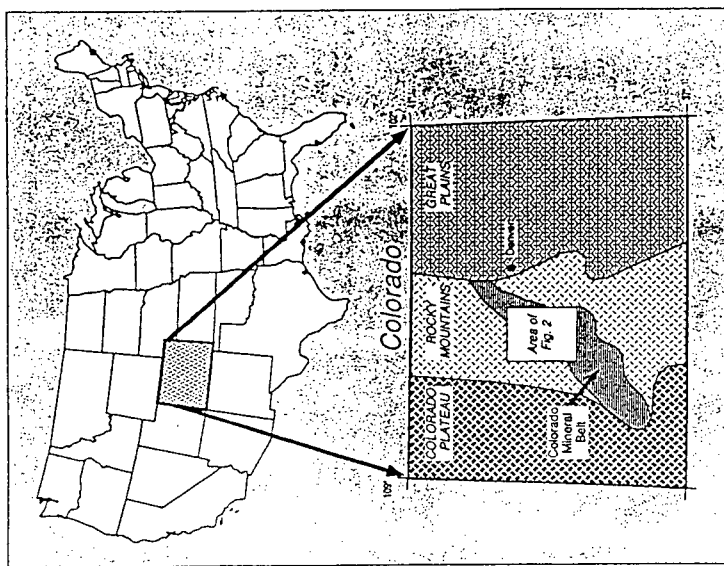


Figure 7.3. Map showing the location of the Colorado mineral belt. From Beaty et al. (1990).

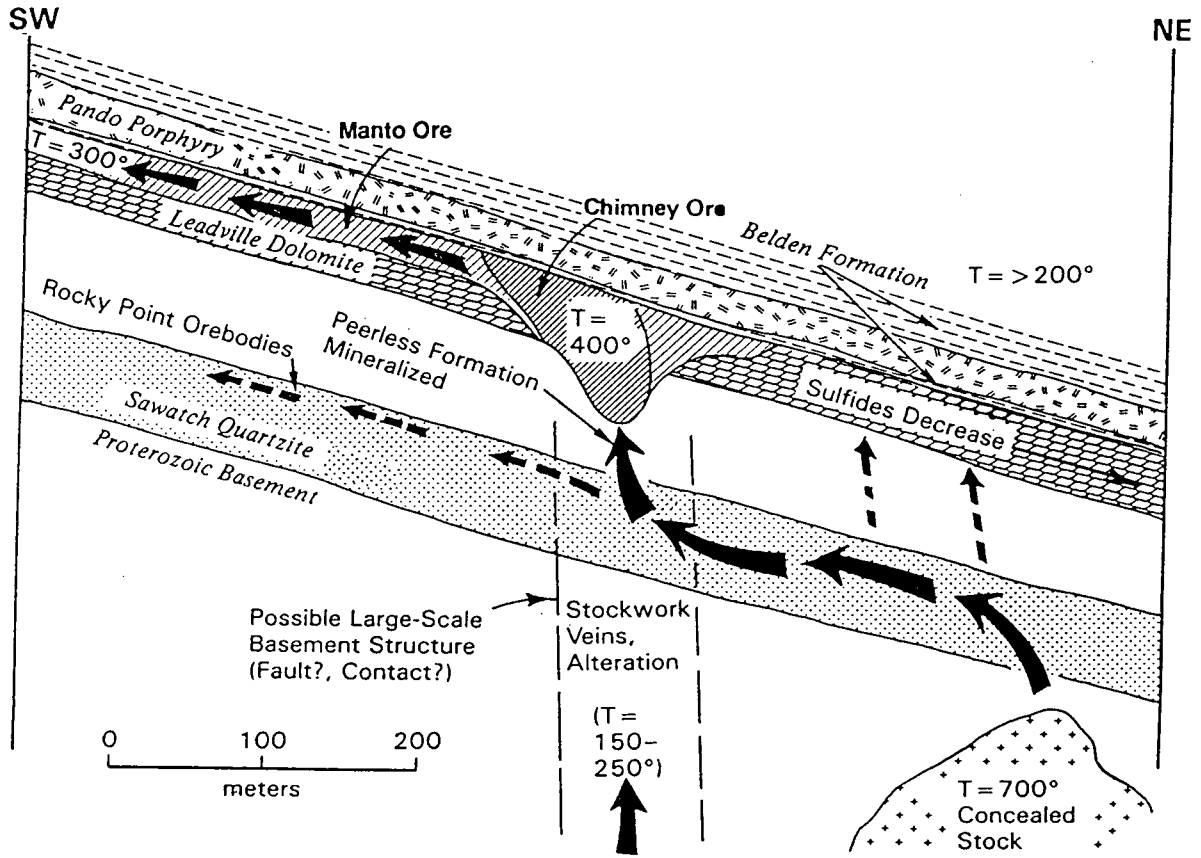


Figure 7.5. Schematic illustration of the hydrologic model interpreted to have produced the ore deposits at Gilman, Colorado. Approximate scale. The concealed stock is inferred to be the source of heat, fluid, sulphur, and metals. From Beaty et al. (1990).

veins peripheral to mineralizing centres. However, deposits of the scale and base metal content of those in the Colorado mineral belt have not yet been found in the Ketz River district.

7.8 Recommendations for future work

Three lines of research would greatly contribute to a better understanding of the Ketz River deposit: geochemical studies, additional geothermometry, and search for potentially related intrusive rocks that could be compared isotopically with the ores as possible metal sources.

Over 600 diamond drill holes were drilled in the Ketz River, Iona Silver, and Oxo areas. Drill core samples were only assayed for Au, and less commonly Ag. Re-splitting a representative suite of core samples and analyzing them for major and trace metals through full digestion ICP-MS or XRF would produce a useful database that may be used to characterize metal zoning in the deposit. Geostatistical treatment of the data could show zoning patterns that point toward areas with greater potential for gold mineralization.

Calcite-dolomite mineral pair geothermometry is feasible in Fe-silicate alteration and manto mineralization, where hydrothermal calcite crystals are large enough for microprobe analyses with large beam diameter, and can be easily distinguished from primary carbonates. The calcite-dolomite geothermometry would yield minimum temperatures of mineralization, which could be contrasted to maximum temperature estimates reported in this study.

Intrusive rocks of dioritic composition north of the Iona Silver veins have been reported. Finding, describing, dating, and analyzing trace lead isotopes in those intrusives could provide important information about the origin of fluids, metals, sulphur, and heat for the Ketz River deposit.

8 REFERENCES

- Abbott, G.A., 1983, Silver-bearing veins and replacement deposits of the Rancheria district. Yukon Exploration and Geology, Yukon Indian and Northern Affairs, p. 34-44.
- Abbott, 1986, Epigenetic mineral deposits of the Ketzia-Seagull district, Yukon. Yukon Geology, Indian and Northern Affairs Canada, v.1, p. 56-66.
- Andrew, A., Godwin, C.I., and Sinclair, A.J., 1984, Mixing line isochrons: A new interpretation of galena lead isotope data from southeastern British Columbia. Economic Geology, v. 79, p. 919-932.
- Bradford, J.A., and Godwin, C.I., 1988, Midway silver-zinc manto deposit, northern British Columbia (104O/16). British Columbia Ministry of Energy, Mines and Petroleum Resources, Geological Fieldwork 1987, Paper 1988-1, p. 353-360.
- Beaty, D.W., 1990, Origin of the ore deposits at Gilman, Colorado, *in* Beaty, D.W., Landis, G.P., and Thompson, T.B. (eds.), Carbonate-hosted sulfide deposits of the central Colorado mineral belt. Economic Geology Monograph 7, p. 193-265.
- Bookstrom, A.A., 1990, Igneous rock and carbonate-hosted ore deposits of the central Colorado mineral belt, *in* Beaty, D.W., Landis, G.P., and Thompson, T.B. (eds.), Carbonate-hosted sulfide deposits of the central Colorado mineral belt. Economic Geology Monograph 7, p. 45-65.
- Cathro, M.S., 1962, Geology and mineral deposits of the Ketzia River mining district, Yukon Territory, Canada. M. Sc. Thesis. Colorado School of Mines, 176 p.
- Childe, F.C., 1997, Timing and tectonic setting of volcanogenic massive sulphide deposits in British Columbia: Constraints from U-Pb geochronology, radiogenic isotopes, and geochemistry. Ph.D. thesis. University of British Columbia, 298 p.
- Doherty, A., 1997, Mamu-Bravo-Kulan claims, a VHMS exploration target based on geochemical and geophysical anomalies in Mississippian volcanics within Cassiar Platform, NTS105-F/7, 8, 9 &10. Exploration and Geological Services Division, Yukon, Indian and Northern Affairs Canada, p. 56-61.
- Dunham, R.J., 1962, Classification of carbonate rocks according to depositional texture, *in* Ham, W.E., (ed.); Classification of Carbonate Rocks. American Association of Petroleum Geologists Mem. 1, p. 108-121.
- Driver, L., Creaser, R., Chacko, T, and Erdmer, P., 1998, Petrogenesis of the Cretaceous Cassiar batholith, Yukon-B. C., Canada. Lithoprobe SNORCLE report of the 1998 combined meeting. Vancouver, p.158.
- Farmer, G.L., and Depaolo, D.J., 1997, Sources of hydrothermal components: Heavy isotopes, *in* Barnes, H.L. (ed.), Hydrothermal ore deposits. John Wiley & Sons, Inc., 3rd edition, p. 31-62.
- Folk, R.L., 1962, Spectral subdivision of limestone types, *in* Ham, W.E., (ed.), Classification of Carbonate Rocks. American Association of Petroleum Geologists Mem. 1, p. 62-84.
- Fritz, W.H., Cecile, M.P., Norford, B.S., Morrow, D., and Geldsetzer, H.H.J., 1991, Cambrian to Middle Devonian assemblages, *in* Geology of the Cordilleran Orogen in Canada, H.

- Gabrielse and C.J. Yorath (ed.); Geological Survey of Canada, Geology of Canada, no.4, p. 151-218.
- Fritz, W.H., and Crimes, T.P., 1985, Lithology, trace fossils, and correlation of Precambrian-Cambrian boundary beds, Cassiar Mountains, north-central British Columbia. Geological Survey of Canada. Paper 83-13, 24 p.
- Godwin, C.I., and Sinclair, A.J., 1982, Average lead isotope growth curves for shale-hosted zinc-lead deposits, Canadian Cordillera. *Economic Geology*, v. 77, p. 675-690.
- Godwin, C.I., Sinclair, A.J., and Ryan, B.D., 1982, Lead isotope models for the genesis of carbonate-hosted Zn-Pb, shale-hosted Ba-Zn-Pb, and silver-rich deposits in the Northern Canadian Cordillera. *Economic Geology*, v. 77, p. 82-94.
- Gordey, S.P., 1981, Stratigraphy, structure and tectonic evolution of the southern Pelly Mountains in the Indigo Lake area, Yukon Territory. Geological Survey of Canada. Paper 81-318, 44 p.
- Gordey, S.P., 1991, Devonian-Mississippian clastics of the Foreland and Omineca Belts, *in* Geology of the Cordilleran Orogen in Canada, H. Gabrielse and C. J. Yorath (ed.); Geological Survey of Canada, Geology of Canada, no.4, p. 230-242.
- Holbek, P.M., and Wilson, R.G., 1998, The Wolf Discovery: A Kuroko-style volcanogenic massive sulphide deposit hosted by rift-related, alkaline felsic volcanic rocks. Yukon Exploration and Geology. Exploration and Geological Services Division, Yukon, Indian and Northern Affairs Canada, p. 115-120.
- Kretschmar, U., and Scott, S.D., 1976, Phase relations involving arsenopyrite in the system Fe-As-S and their application. *Canadian Mineralogist*, v. 14, p. 364-386.
- Lewis, P., 1997, Notes on the structural geology of the Silvertip property. Preliminary report for Imperial Metals, 7 p.
- Newberry, R.J., McCoy, D.T., and Brew, D.A., 1995, Plutonic-hosted gold ores in Alaska: Igneous versus metamorphic origins. *Resource Geology Special Issue*, N. 18, p. 57-100.
- McCoy, et al. (in prep.), Paragenesis and mineralogy of central Alaska gold deposits. PhD thesis. University of Alaska Fairbanks.
- McCoy, D.T., Newberry, R.J., Layer, P., DiMarchi, J.J., Bakke, A., Mastermann, J.S., and Minehane, D.L., 1997, Plutonic related deposits of interior Alaska. *Economic Geology Monograph* 9, p. 191-241.
- Mortensen, J.K., 1982, Geological setting and tectonic significance of Mississippian felsic metavolcanic rocks in the Pelly Mountains, southeastern Yukon Territory. *Can. J. Earth Sci.*, v. 19, p. 8-22.
- Mortensen, J.K., 1998, New advances in Yukon geology driven by geochronology during the last ten years, *in* Cordillera revisited: Recent developments in cordilleran geology, tectonics, and mineral deposits. *Cordilleran Roundup Short Course Notes*, p. 76-85.
- Mortensen, J.K., and Tosdal, R., 1998, Geochronology of mineral deposits. MDRU Short Course # 23, 84p.
- Read, B.C., 1980, Lower Cambrian archeocyathid buildups, Pelly Mountains, Yukon Territory. Geological Survey of Canada, Paper 78-18, 54 p.

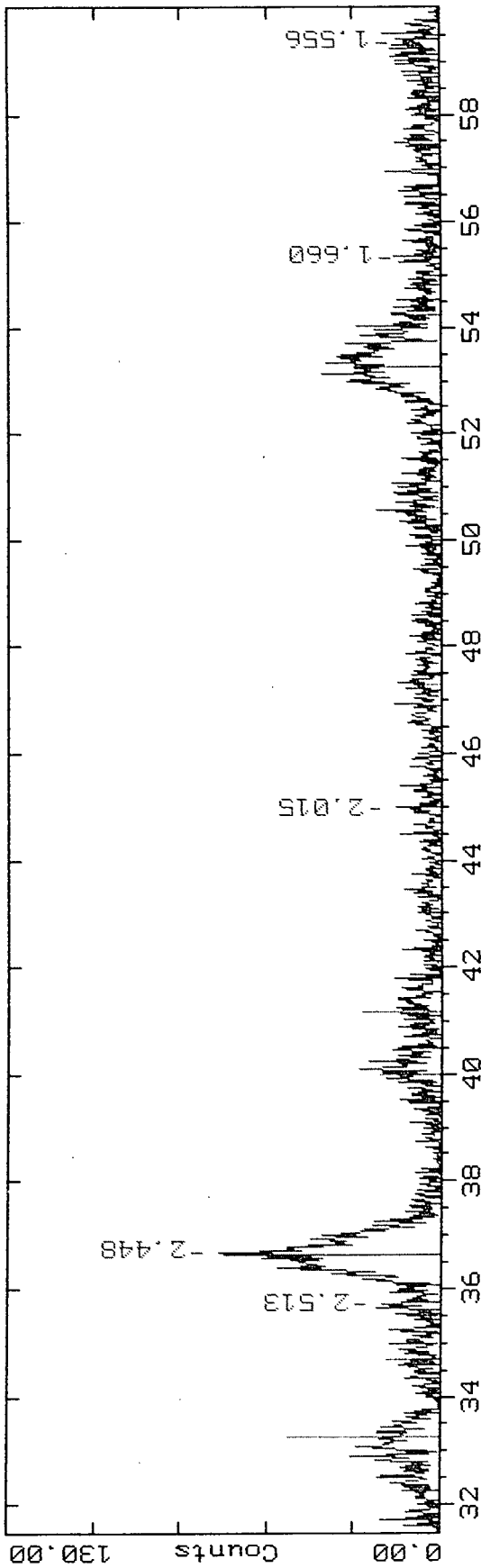
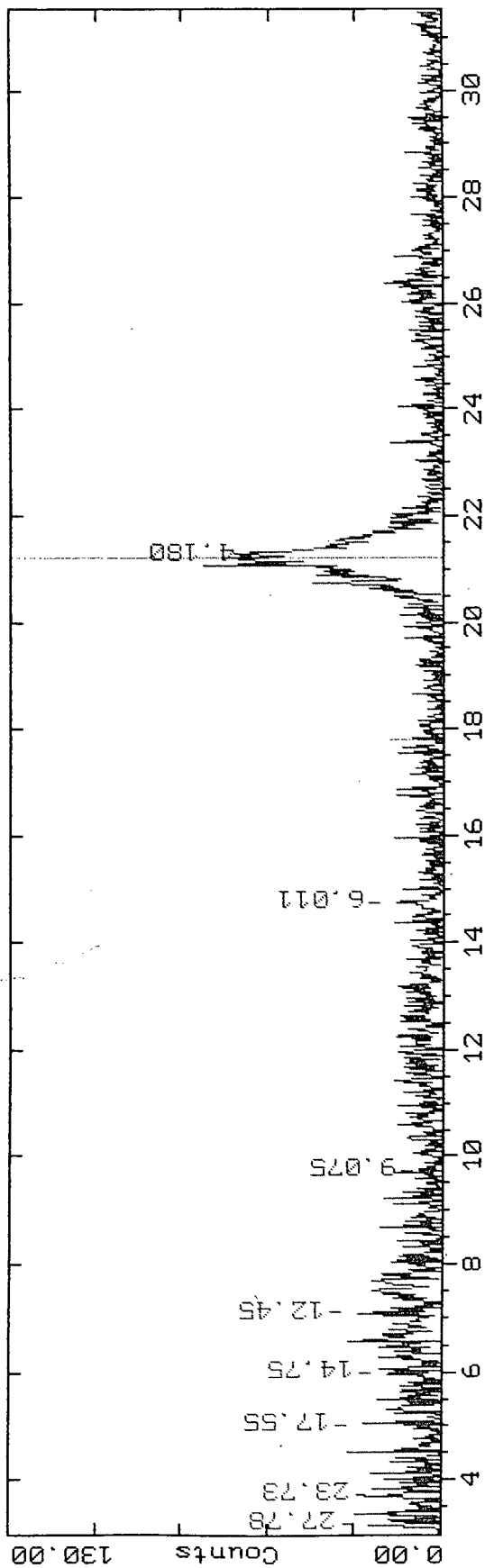
- Sharp, Z.D., Essene, E.J., and Kelly, W.C., 1985, A re-examination of the arsenopyrite geothermometer: Pressure considerations and applications to natural assemblages. *Canadian Mineralogist*, v. 23, p. 517-534.
- Sillitoe, R.H., and Bonham, H.F., 1990, Sediment-hosted gold deposits: Distal products of magmatic-hydrothermal systems. *Geology*, v. 18, p. 157-161.
- Staveley, J.A., 1992, The mineralogy and geochemistry of polymetallic mineral deposits at the Ketz River Gold Mine, Pelly Mountains, central Yukon Territory. M. Sc. Thesis. University of Alberta, 81 p.
- Steiger, R.H., and Jäger, E., 1977, Subcommittee on Geochronology: Convention on the use of decay constants in geo- and cosmochronology. *Earth and Planetary Science Letters*, v. 26, p. 207-221.
- Stroschein, R., 1997, Report on the 1996 exploration program, Ketz River project, south central Yukon. Internal report, YGC Resources Inc.
- Templeman-Kluit, 1977a, Geology of Quiet Lake (105F) and Finlayson Lake (105G) map areas, Yukon Territory. Geological Survey of Canada, Open File 486.
- Templeman-Kluit, 1977b, Stratigraphic and structural relations between Selwyn Basin, Pelly-Cassiar Platform, and Yukon Crystalline Terrane in the Pelly Mountains, Yukon, *in* Report of Activities, Part A. Geological Survey of Canada, Paper 77-1A. p. 223-227.
- Thompson, T. 1998, Carbonate-hosted sulfide deposits of the central Colorado mineral belt: Introduction, general discussion, and summary. *Economic Geology Monograph 7*, p. 1-18.
- Titley, S.R., 1993, Characteristics of high-temperature carbonate hosted massive sulphide ores in the United States, Mexico and Peru, *in* Kirkham, R.V., Sinclair, W.D., Thorpe, R.I., and Duko, J.M. (eds.), *Mineral Deposit Modeling*. Geological Association of Canada Special Paper 40, p. 585-614.
- Wheeler, J.O., Green, L.H., and Roddick, J.A., 1960, Quiet Lake, Yukon Territory. Geological Survey of Canada, Map 7-1960.
- Woodsworth, G.J., Anderson, R.G., and Armstrong, R.L., 1991, Plutonic regimes, Chapter 15 *in* *Geology of the Cordilleran Orogen in Canada*, H. Gabrielse and C. J. Yorath (ed.); Geological Survey of Canada, *Geology of Canada*, no.4, p. 493-523.
- Yardley, B.W.D., MacKenzie, W.S., and Guilford, C., 1990, *Atlas of metamorphic rocks and their textures*. Longman Scientific & Technical, 120 p.
- Zartman, R.E., and Doe, B.R., 1981, Plumbotectonics: the model. *Tectonophysics*, v. 75, p. 135-162.

APPENDIX A

X-Ray diffraction analyses of oxides.

17-Dec-1996 19:45

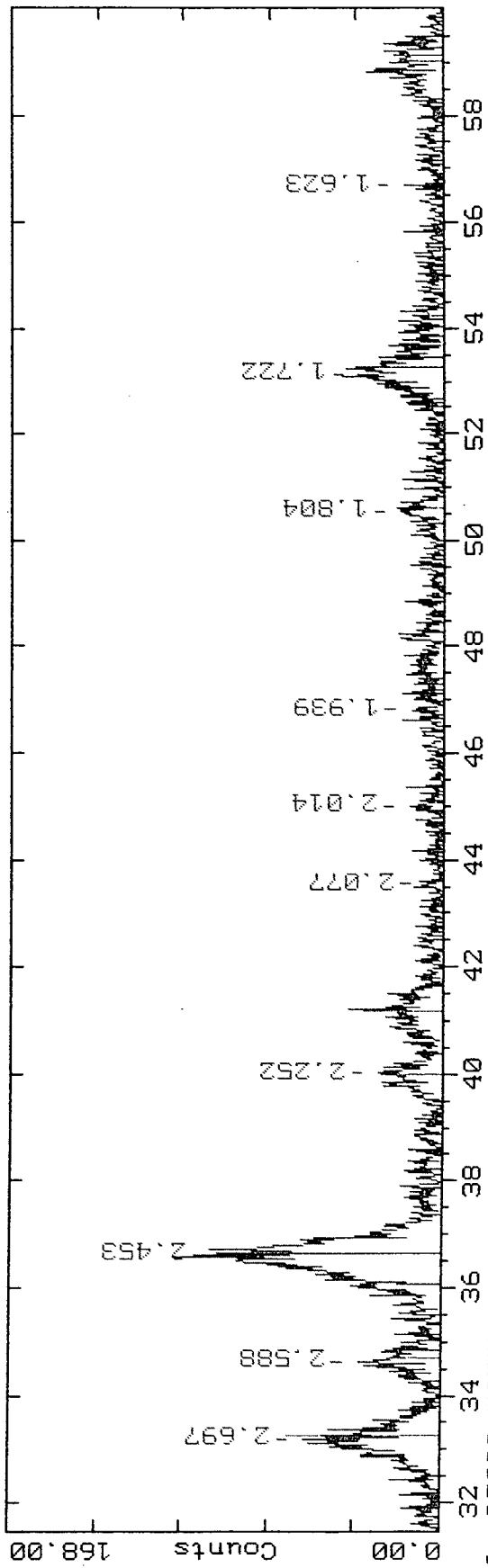
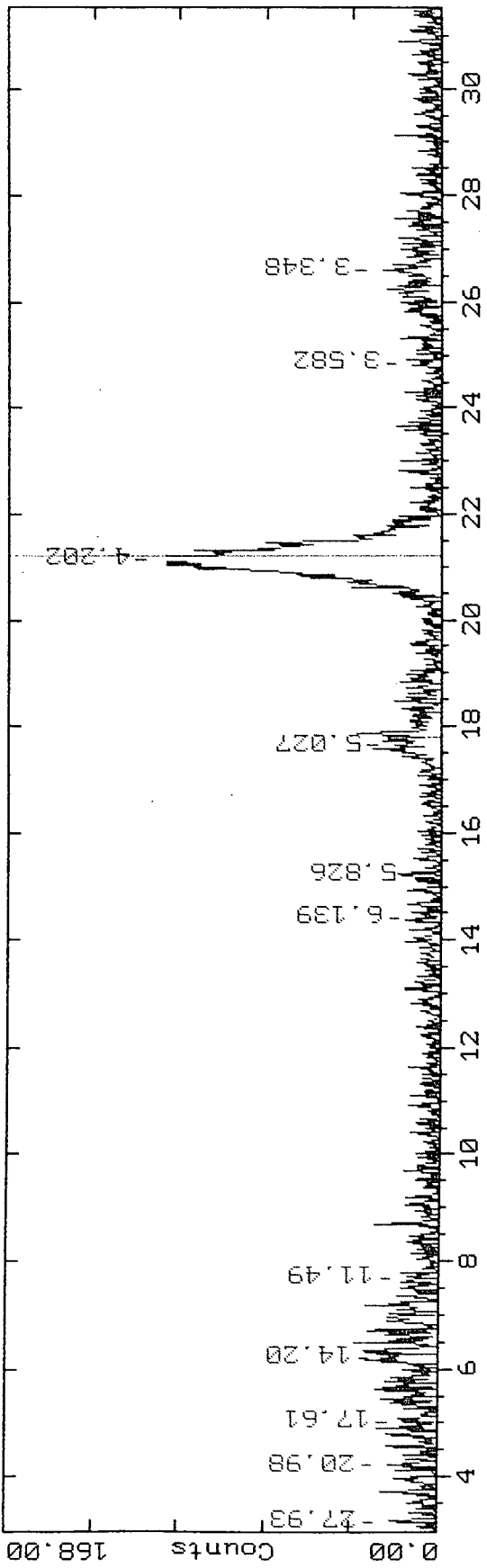
2-Theta - Scale



C:\D5000\USERDATA\AF_14_A.RAW AF_14_A (CT: 0.8s, SS:0.020dg, WL: 1.540940)
29-0713 I FeO(OH) Goethite (WL: 1.540940)

17-Dec-1996 21:06

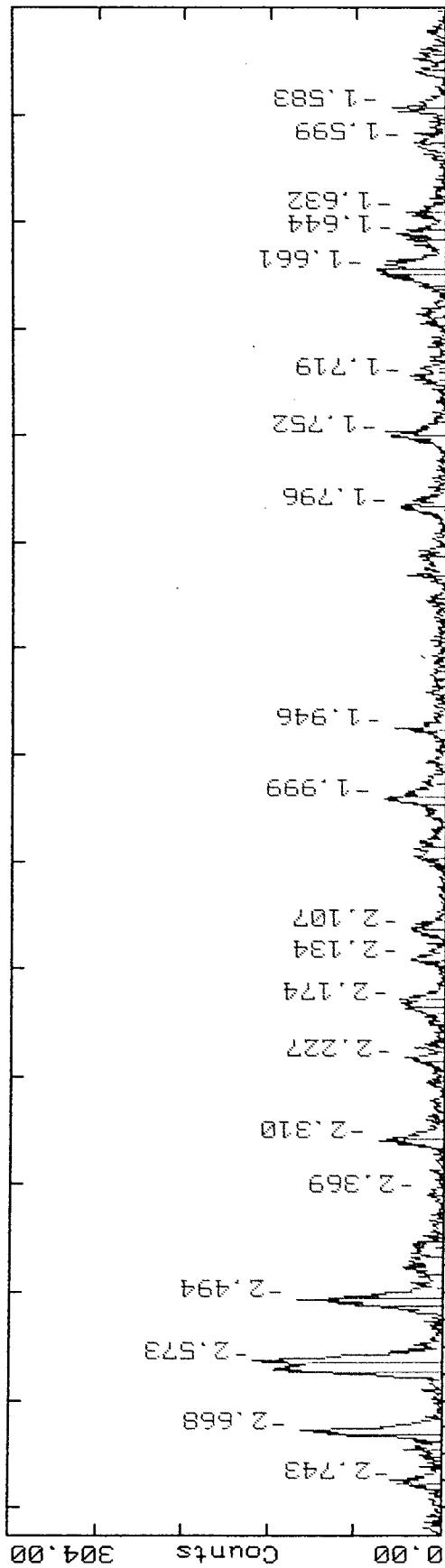
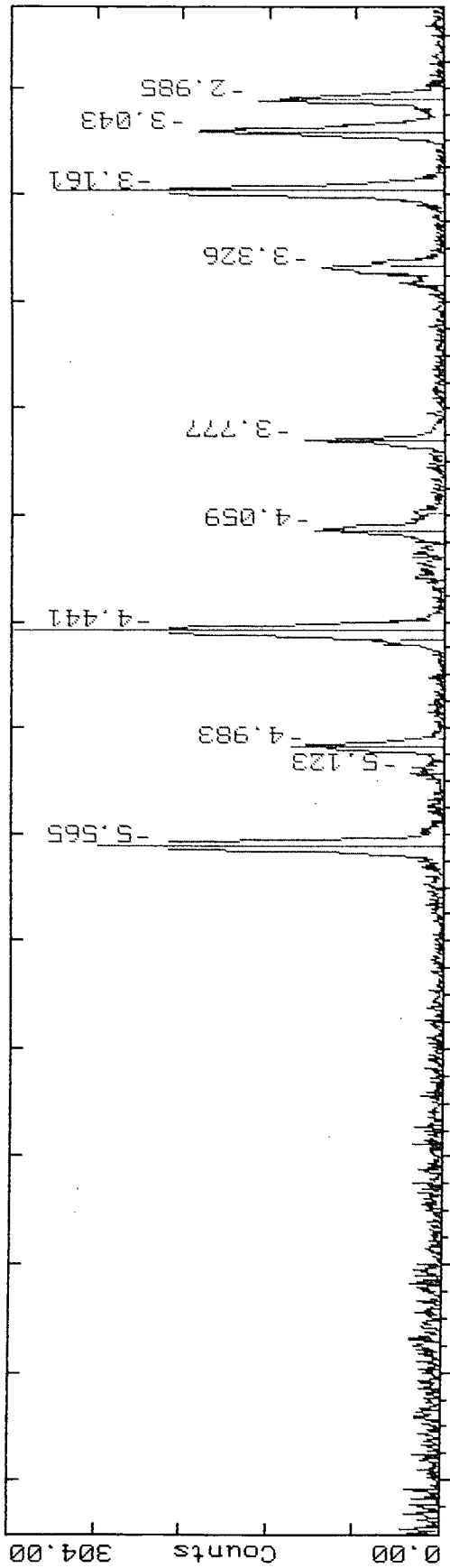
2-Theta - Scale



C:\D5000\USERDATA\CATHEDRA\RAW CATHEDRAL (CT: 0.8s, SS:0.020dg, WL: 1.54094a)
29-0713 I Fe(OH) Goethite (NL: 1.54094a)

15-Dec-1996 15:39

2-Theta - Scale



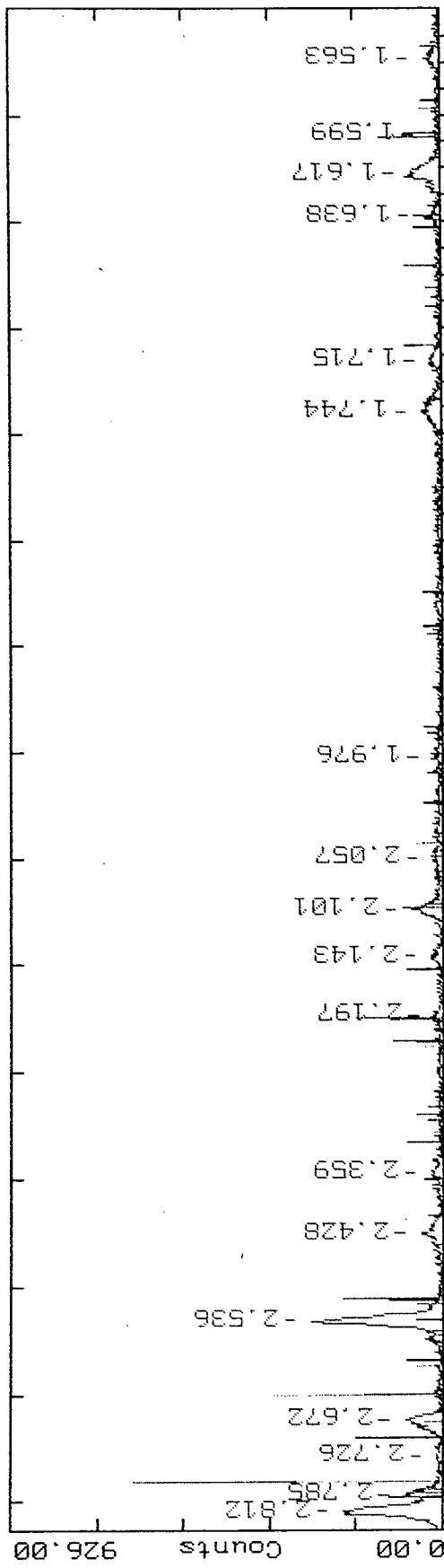
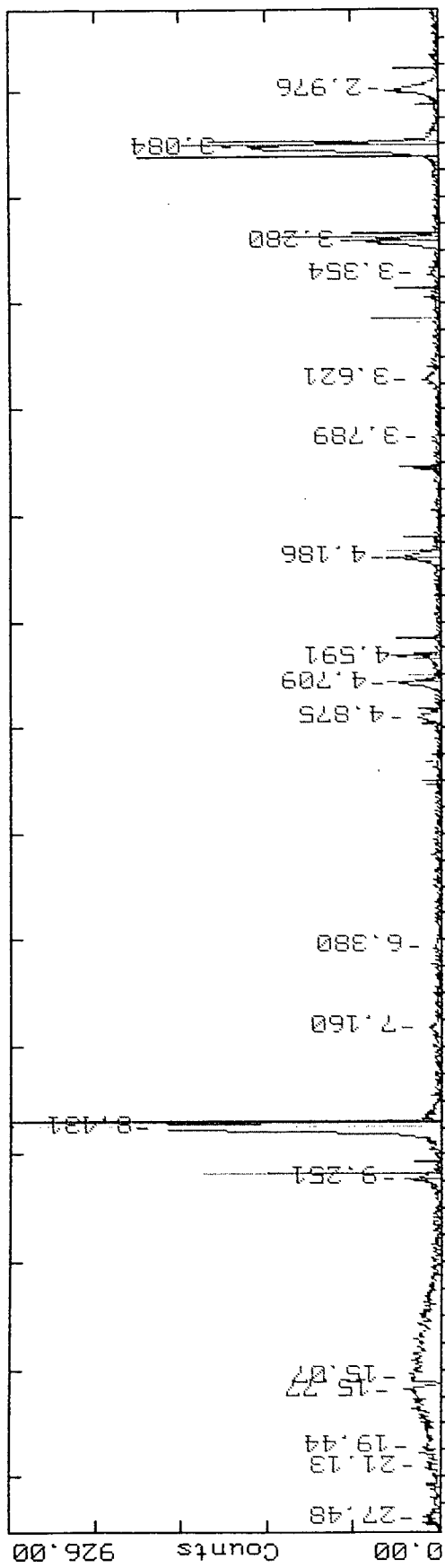
C:\D5000\USERDATA\AF135A.RAW AF135A (CT: 0.8s, SS:0.020dg, WL: 1.5409Ao, DX: -.150)
 57-0468 * FeAsO4.2H2O Scorodite (ML: 1.5409Ao)
 29-0713 I Fe(OH) Goethite (ML: 1.5409Ao)

APPENDIX B

X-Ray diffraction analyses of Fe-amphibole.

17-Dec-1996 22:16

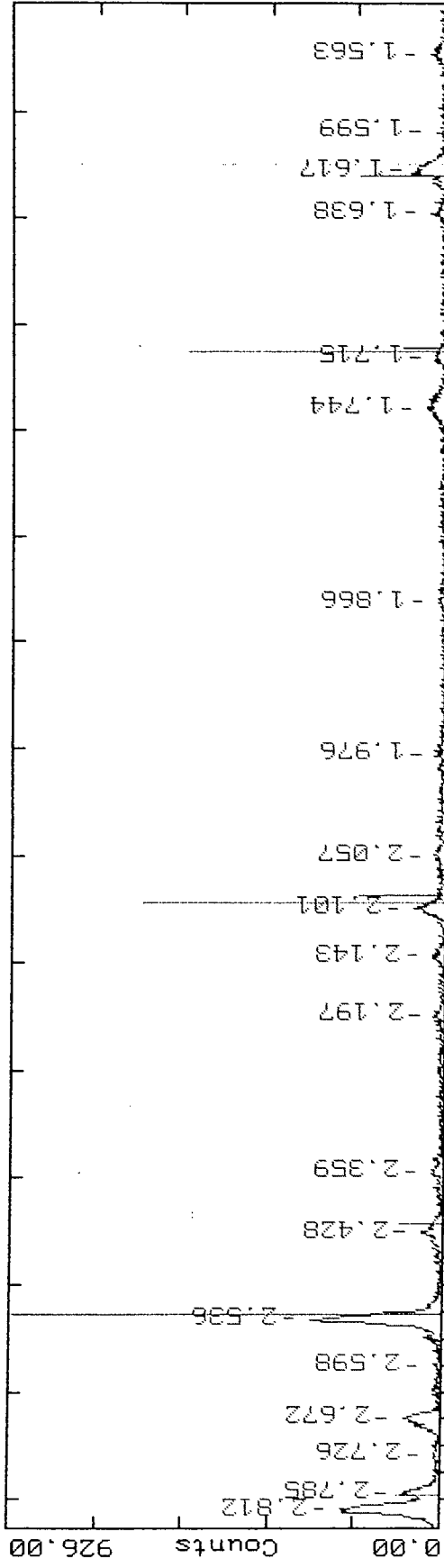
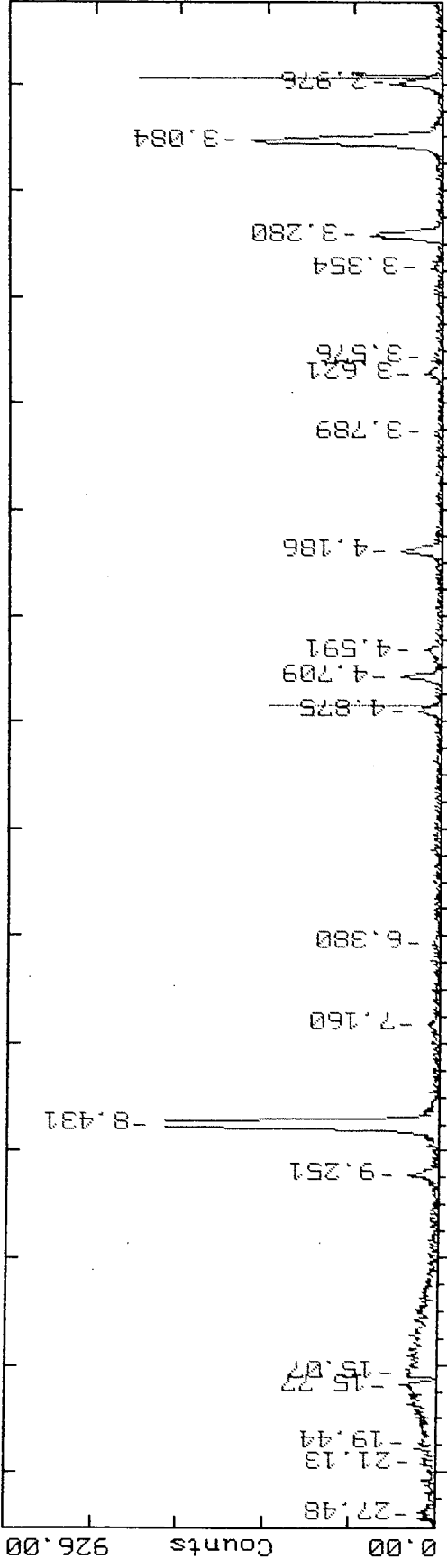
2-Theta - Scale



C:\D5000\USERDATA\KR_95_50_RAW_KR_95_505_B (CT: 0.8s, 88:0.020dg, WL: 1.5409Ao)
 42-0545 * (Fe0.6Mg0.4)7S18O22(OH)2 Cummerite (WL: 1.5409Ao)
 33-0300 0 (Fe,Mg)7S18O22(OH)2 Dannemorite (WL: 1.5409Ao)
 44-1401 I Fe7S18O22(OH)2 Grunerite (WL: 1.5409Ao)
 20-0481 I (Ca,Na)2.26(Mg,Fe,Al)5.15(Si,Al)8O22(OH)2 Magnesiohornblende (WL: 1.5409Ao)

17-Dec-1996 22:34

2-Theta - Scale



C:\D5000\USERDATA\KR_95_50_RAW\KR_95_505_B (CT: 0.8s, SS:0.0200dg, WL: 1.54094Å)
3-0858 D Fe3O4 Magnetite (WL: 1.54094Å)
13-06614 D Fe3O4 Magnetite (WL: 1.54094Å)

APPENDIX C

Microprobe analyses of arsenopyrite.
A% = atomic percent

sample	label	A%(As)	A%(S)	A%(Fe)	A%(Mn)	A%(Co)	A%(Ni)	A%(Cu)	A%(Zn)	A%(Sb)
4448	48-A1	29.82	37.45	32.63	0.00	0.00	0.00	0.08	0.00	0.02
	48-A2	29.53	37.75	32.68	0.00	0.00	0.00	0.01	0.00	0.01
	48-A3	29.74	37.58	32.64	0.00	0.00	0.00	0.00	0.02	0.01
	48-A4	29.77	37.62	32.58	0.00	0.00	0.01	0.02	0.01	0.01
	48-A5	28.44	38.77	32.67	0.00	0.00	0.01	0.08	0.03	0.00
	48-B1	29.45	37.61	32.93	0.00	0.00	0.00	0.00	0.00	0.00
	48-B2	29.24	37.65	33.06	0.00	0.00	0.01	0.01	0.01	0.01
	48-B3	29.22	37.79	32.88	0.00	0.00	0.01	0.05	0.00	0.03
	48-B4	29.53	37.41	33.01	0.00	0.00	0.00	0.00	0.02	0.02
	48-B5	29.65	37.42	32.88	0.00	0.00	0.02	0.00	0.01	0.02
	48-B6	29.58	37.42	32.96	0.00	0.00	0.00	0.00	0.01	0.04
	48-B7	29.71	37.16	33.10	0.00	0.00	0.02	0.00	0.00	0.01
	48-C1	28.74	38.39	32.87	0.00	0.00	0.00	0.00	0.00	0.00
	48-C2	29.35	37.73	32.88	0.00	0.00	0.00	0.01	0.01	0.01
	48-C3	29.31	37.67	32.99	0.00	0.00	0.01	0.00	0.00	0.01
	48-C5	28.51	38.45	33.02	0.00	0.00	0.00	0.00	0.00	0.02
	48-C6	28.88	38.19	32.88	0.00	0.00	0.02	0.01	0.02	0.00
5353	53D-1	28.74	38.35	32.86	0.00	0.00	0.01	0.01	0.00	0.03
	53D-2	29.32	37.79	32.76	0.00	0.00	0.00	0.11	0.00	0.02
	53D-3	28.79	38.14	33.01	0.00	0.00	0.02	0.03	0.00	0.01
	53D-4	28.71	38.34	32.94	0.00	0.00	0.01	0.00	0.00	0.00
	53e1	28.67	38.41	32.90	0.00	0.00	0.00	0.00	0.00	0.01
	53e2	28.93	38.22	32.83	0.00	0.00	0.00	0.01	0.00	0.01
	53e4	29.31	37.70	32.97	0.00	0.00	0.01	0.00	0.00	0.00
	53e5	28.81	38.27	32.87	0.00	0.00	0.03	0.02	0.00	0.00
	53e6	29.62	37.45	32.91	0.00	0.00	0.01	0.00	0.01	0.00
	53e7	29.29	37.83	32.85	0.00	0.00	0.00	0.02	0.00	0.00
	53e8	30.40	36.34	33.23	0.00	0.00	0.01	0.00	0.01	0.00
	53e9	29.45	37.54	32.97	0.00	0.00	0.00	0.00	0.03	0.00
	53e1-	29.45	37.58	32.95	0.00	0.00	0.00	0.02	0.00	0.01
	53e11	29.37	37.62	32.93	0.00	0.00	0.02	0.02	0.00	0.04
	53F-1	26.58	40.53	32.86	0.00	0.00	0.00	0.00	0.02	0.00
	53F-2	28.63	38.35	33.01	0.00	0.00	0.01	0.00	0.00	0.00
	53F-3	28.90	38.07	33.01	0.00	0.00	0.00	0.01	0.01	0.00
	53F-6	28.66	38.44	32.87	0.00	0.02	0.00	0.00	0.00	0.00
	53G-2	29.55	37.49	32.95	0.00	0.00	0.00	0.00	0.00	0.00
	53G-6	30.48	36.48	33.01	0.00	0.00	0.00	0.02	0.01	0.00
	53G-7	30.05	36.49	33.44	0.00	0.00	0.00	0.00	0.00	0.01
	53G-8	29.30	37.87	32.80	0.00	0.00	0.03	0.00	0.00	0.00
	53G-5	30.14	36.81	33.04	0.00	0.01	0.00	0.00	0.00	0.00
	53G-1	28.69	38.70	32.56	0.00	0.00	0.01	0.02	0.02	0.00
4427	27a-1	31.92	34.95	33.03	0.00	0.00	0.03	0.01	0.05	0.02
	27a-2	31.83	35.08	33.01	0.00	0.01	0.00	0.02	0.04	0.01
	27a-3	32.13	34.73	33.10	0.00	0.00	0.02	0.00	0.00	0.02
	27a-4	31.85	35.07	33.05	0.00	0.00	0.00	0.00	0.00	0.03
	27a-5	31.64	35.30	32.99	0.00	0.00	0.00	0.03	0.03	0.01
	27b-1	31.84	35.38	32.76	0.00	0.00	0.00	0.00	0.01	0.00
	27b-2	32.90	33.93	33.11	0.00	0.02	0.00	0.00	0.00	0.04
	27b-3	33.24	33.76	32.90	0.00	0.00	0.02	0.04	0.00	0.03
	27b-4	32.70	34.32	32.89	0.00	0.02	0.02	0.00	0.02	0.03
	27b-5	29.67	37.40	32.92	0.00	0.00	0.00	0.00	0.00	0.00
	27b-6	29.20	37.78	33.00	0.00	0.00	0.01	0.00	0.00	0.01
	27b-7	29.32	37.88	32.74	0.00	0.00	0.00	0.01	0.01	0.03

sample	label	A%(As)	A%(S)	A%(Fe)	A%(Mn)	A%(Co)	A%(Ni)	A%(Cu)	A%(Zn)	A%(Sb)
4427	27b-8	29.92	36.82	33.21	0.00	0.00	0.00	0.00	0.03	0.02
	27b-9	29.37	37.73	32.71	0.00	0.00	0.03	0.15	0.00	0.00
	27b-10	28.81	38.34	32.83	0.00	0.00	0.00	0.01	0.00	0.00
	27b-11	29.47	37.64	32.87	0.00	0.00	0.00	0.01	0.00	0.02
	27b-12	30.19	36.95	32.82	0.00	0.00	0.00	0.03	0.00	0.01
	27b-13	29.72	37.26	32.97	0.00	0.00	0.01	0.00	0.00	0.03
	27b-14	29.64	37.31	33.02	0.00	0.00	0.00	0.01	0.00	0.02
	27b-15	29.06	38.27	32.64	0.00	0.01	0.00	0.00	0.00	0.02
	27b-16	29.55	37.50	32.90	0.00	0.00	0.03	0.00	0.00	0.01
	27b-17	29.54	37.73	32.65	0.00	0.02	0.01	0.00	0.01	0.02
	27b-18	29.69	37.22	33.05	0.00	0.00	0.02	0.01	0.00	0.01
	27b-19	29.46	37.84	32.63	0.00	0.00	0.00	0.01	0.00	0.05
	27b-20	29.35	37.64	32.85	0.00	0.00	0.01	0.15	0.00	0.01
	27b-21	30.07	37.04	32.85	0.00	0.00	0.01	0.02	0.00	0.00
	27b-22	29.59	37.31	33.08	0.00	0.00	0.00	0.00	0.01	0.01
	27b-23	29.53	37.50	32.94	0.00	0.00	0.00	0.00	0.00	0.03
	27c-1	28.68	38.31	32.95	0.00	0.00	0.02	0.04	0.00	0.00
	27c-2	29.82	37.17	32.99	0.00	0.00	0.00	0.00	0.01	0.01
	27c-3	29.32	37.68	32.98	0.00	0.00	0.00	0.00	0.00	0.02
	27c-4	29.31	37.70	32.98	0.00	0.00	0.00	0.00	0.00	0.00
	27c-6	29.67	37.57	32.73	0.00	0.01	0.00	0.01	0.00	0.01
	27c-7	29.89	37.01	33.04	0.00	0.00	0.00	0.04	0.00	0.01
	27c-8	28.88	38.08	33.01	0.00	0.00	0.00	0.01	0.00	0.01
	27c-9	28.89	37.99	33.06	0.00	0.00	0.03	0.00	0.02	0.00
	27c-10	28.93	38.42	32.65	0.00	0.00	0.00	0.00	0.00	0.00
	27d-1	29.33	37.79	32.87	0.00	0.00	0.00	0.00	0.00	0.01
	27d-2	29.19	37.97	32.80	0.00	0.00	0.00	0.04	0.00	0.00
	27d-3	29.16	37.92	32.89	0.00	0.00	0.02	0.00	0.01	0.00
	27d-4	28.94	38.12	32.90	0.00	0.00	0.02	0.01	0.00	0.01
	27d-5	28.83	38.16	32.96	0.00	0.00	0.04	0.00	0.01	0.00
	27d-6	30.69	36.53	32.74	0.00	0.00	0.00	0.01	0.02	0.00
	27e1	30.51	36.21	33.26	0.00	0.00	0.00	0.01	0.00	0.02
	27e2	29.35	37.85	32.79	0.00	0.00	0.00	0.00	0.00	0.01
	27e3	29.39	37.64	32.93	0.00	0.01	0.00	0.01	0.00	0.02
	27f-1	28.86	38.11	33.02	0.00	0.00	0.00	0.00	0.01	0.00
	27f-2	29.09	37.89	33.01	0.00	0.00	0.00	0.01	0.00	0.00
	27f-3	28.46	38.64	32.90	0.00	0.00	0.00	0.00	0.00	0.00
	27f-4	28.68	38.15	33.15	0.00	0.00	0.01	0.00	0.00	0.02
	27f-6	29.53	37.55	32.87	0.00	0.00	0.01	0.01	0.01	0.02
	27f-7	29.27	37.44	33.21	0.00	0.00	0.02	0.03	0.01	0.02
	27h-1	29.66	37.23	33.06	0.00	0.01	0.02	0.00	0.02	0.00
	27h-2	28.92	38.01	33.04	0.00	0.00	0.01	0.01	0.00	0.00
	27h-3	29.70	37.01	33.24	0.00	0.00	0.00	0.02	0.03	0.00
	27h-4	29.20	37.47	33.30	0.00	0.00	0.01	0.00	0.03	0.00
	27h-5	29.43	37.56	32.96	0.00	0.01	0.00	0.01	0.03	0.00
	27h-6	29.22	37.76	32.97	0.00	0.00	0.02	0.01	0.00	0.01
	27h-7	29.49	37.18	33.29	0.00	0.00	0.01	0.00	0.02	0.01
	27i-1	29.20	37.80	32.98	0.00	0.00	0.00	0.01	0.00	0.00
	27i-2	29.29	37.65	33.02	0.00	0.00	0.02	0.00	0.00	0.01
	27i-3	29.00	38.11	32.86	0.00	0.00	0.01	0.02	0.00	0.00
	27i-4	29.34	37.60	33.02	0.00	0.00	0.02	0.00	0.00	0.02
	27i-5	28.03	38.96	32.96	0.00	0.01	0.00	0.01	0.01	0.01
	27i-6	29.87	37.34	32.75	0.00	0.00	0.02	0.00	0.01	0.01
	27i-7	29.35	37.82	32.78	0.00	0.00	0.03	0.00	0.00	0.02
	27i-8	29.83	37.05	33.11	0.00	0.00	0.00	0.00	0.01	0.00
	27i-9	29.23	37.82	32.91	0.00	0.00	0.02	0.00	0.00	0.02
	27i-10	29.43	37.81	32.75	0.00	0.00	0.00	0.00	0.00	0.00

sample	label	A%(As)	A%(S)	A%(Fe)	A%(Mn)	A%(Co)	A%(Ni)	A%(Cu)	A%(Zn)	A%(Sb)
4427	27i-11	29.30	37.93	32.75	0.00	0.00	0.00	0.01	0.01	0.00
	27i-12	29.97	37.06	32.96	0.00	0.00	0.00	0.00	0.00	0.00
4425	25-1	31.73	35.19	32.99	0.00	0.00	0.00	0.04	0.04	0.00
	25-2	31.17	35.89	32.93	0.00	0.00	0.00	0.00	0.00	0.00
	25-3	29.65	37.16	33.13	0.00	0.00	0.01	0.00	0.03	0.02
	25-4	29.70	37.17	33.07	0.00	0.00	0.02	0.00	0.02	0.02
	25-5	28.88	37.97	33.09	0.00	0.00	0.00	0.00	0.02	0.03
	25-6	29.56	37.14	33.25	0.00	0.00	0.00	0.02	0.00	0.02
	25-7	29.58	37.29	33.10	0.00	0.00	0.01	0.02	0.00	0.00
	25-8	29.42	37.35	33.17	0.00	0.00	0.01	0.00	0.02	0.01
	25-9	29.86	36.67	33.41	0.00	0.01	0.00	0.03	0.01	0.01
	25-10	29.62	37.14	33.19	0.00	0.00	0.00	0.02	0.01	0.02
	25-11	29.43	37.17	33.34	0.00	0.00	0.01	0.02	0.00	0.03
	25-12	29.48	37.46	33.02	0.00	0.00	0.02	0.00	0.00	0.02
	25-13	27.61	39.25	33.13	0.00	0.00	0.00	0.00	0.01	0.00
	25-14	29.77	37.04	33.12	0.00	0.00	0.01	0.00	0.02	0.04
	25b-3	29.69	37.37	32.91	0.00	0.00	0.01	0.00	0.01	0.01
	25b-4	29.31	37.78	32.88	0.00	0.00	0.00	0.00	0.01	0.02
	25b-5	29.37	37.53	33.03	0.00	0.00	0.00	0.05	0.02	0.00
25b-6	29.34	37.85	32.79	0.00	0.00	0.00	0.00	0.00	0.02	
25b-7	29.14	36.35	34.44	0.00	0.00	0.02	0.01	0.00	0.04	
25b-8	29.25	37.81	32.93	0.00	0.00	0.00	0.01	0.00	0.00	
4426	26c-1	28.39	37.38	34.21	0.00	0.00	0.02	0.00	0.00	0.01
	26c-2	29.04	37.85	33.08	0.00	0.00	0.01	0.00	0.00	0.01
	26c-3	29.29	37.79	32.91	0.00	0.00	0.00	0.00	0.01	0.01
	26c-4	29.46	37.47	33.02	0.00	0.00	0.00	0.01	0.04	0.00
	26c-5	26.96	35.25	37.75	0.02	0.00	0.01	0.01	0.00	0.01
	26c-6	28.42	38.35	33.20	0.00	0.00	0.00	0.01	0.00	0.01
	26c-7	27.80	39.30	32.87	0.00	0.00	0.01	0.00	0.00	0.03
	26c-8	28.79	38.15	33.03	0.00	0.00	0.00	0.02	0.00	0.01
	26c-9	29.36	37.66	32.94	0.00	0.00	0.00	0.00	0.04	0.00
	26c-10	30.01	36.97	32.98	0.00	0.00	0.01	0.00	0.00	0.02
	26c-11	28.67	38.47	32.82	0.00	0.00	0.01	0.01	0.02	0.00
	26c-12	29.16	37.84	32.96	0.00	0.00	0.00	0.01	0.02	0.02
	26c-13	29.08	37.99	32.91	0.00	0.00	0.02	0.00	0.00	0.00
	26d-1	28.89	38.28	32.81	0.00	0.00	0.01	0.00	0.00	0.00
	26d-2	29.37	37.53	33.07	0.00	0.00	0.01	0.00	0.02	0.00
	26d-3	29.29	37.98	32.70	0.00	0.00	0.00	0.00	0.02	0.00
	26d-4	29.07	37.87	33.02	0.00	0.00	0.01	0.00	0.01	0.02
	26d-5	28.56	38.45	32.94	0.00	0.00	0.00	0.01	0.03	0.00
	26d-6	28.85	38.19	32.93	0.00	0.00	0.00	0.00	0.00	0.02
	26d-7	29.09	37.83	33.02	0.00	0.00	0.02	0.01	0.00	0.02
	26d-8	29.39	37.41	33.16	0.00	0.00	0.00	0.02	0.00	0.02
	26d-9	29.52	37.52	32.93	0.00	0.00	0.00	0.00	0.01	0.02
	26d-11	28.16	38.99	32.84	0.00	0.00	0.00	0.00	0.00	0.01
	26d-12	29.16	37.91	32.89	0.00	0.00	0.01	0.00	0.01	0.01
	26d-13	29.46	37.58	32.92	0.00	0.00	0.01	0.00	0.01	0.02
	26d-14	29.37	37.48	33.11	0.00	0.00	0.00	0.04	0.00	0.00
26d-15	29.36	37.54	33.03	0.00	0.00	0.01	0.01	0.00	0.05	
26d-16	29.05	37.81	33.13	0.00	0.00	0.01	0.00	0.00	0.00	
26d-17	29.42	37.60	32.95	0.00	0.00	0.00	0.01	0.01	0.01	
26d-18	29.28	37.70	32.98	0.00	0.00	0.00	0.02	0.00	0.02	
26d-19	29.17	38.04	32.74	0.00	0.00	0.00	0.02	0.03	0.01	

sample	label	A%(As)	A%(S)	A%(Fe)	A%(Mn)	A%(Co)	A%(Ni)	A%(Cu)	A%(Zn)	A%(Sb)
4426	26d-20	29.19	37.67	33.12	0.00	0.00	0.00	0.00	0.01	0.00
	26d-21	29.30	37.76	32.92	0.00	0.00	0.01	0.00	0.00	0.00
	26d-23	29.42	37.53	33.03	0.00	0.00	0.02	0.00	0.00	0.00
	26d-24	28.95	38.05	32.98	0.00	0.00	0.02	0.01	0.00	0.00
	26d-25	29.96	37.07	32.96	0.00	0.00	0.01	0.00	0.00	0.01
	26d-26	29.36	37.62	33.01	0.00	0.00	0.00	0.00	0.00	0.01
	26d-27	28.77	38.32	32.88	0.00	0.00	0.01	0.00	0.01	0.02
	26d-28	29.30	37.62	33.03	0.00	0.00	0.01	0.00	0.00	0.03
	26d-29	29.40	37.74	32.77	0.00	0.00	0.01	0.01	0.00	0.07
	26d-30	29.18	37.63	33.14	0.00	0.00	0.00	0.03	0.02	0.00
	26d-31	29.09	37.78	33.10	0.00	0.00	0.00	0.00	0.00	0.02
	26d-32	29.34	37.71	32.94	0.00	0.00	0.00	0.00	0.00	0.01
	26e	29.11	37.87	32.99	0.00	0.00	0.00	0.01	0.00	0.01
	26e1	29.35	37.70	32.94	0.00	0.00	0.00	0.00	0.00	0.00
	26e2	27.34	39.73	32.90	0.00	0.01	0.00	0.01	0.00	0.00
	26e3	29.19	37.65	33.14	0.00	0.00	0.00	0.00	0.00	0.01
	2634	28.94	38.05	32.97	0.00	0.00	0.00	0.01	0.00	0.02
	26e5	28.89	37.96	33.09	0.00	0.00	0.00	0.02	0.01	0.01
	26e6	28.97	37.99	32.98	0.00	0.00	0.02	0.01	0.03	0.00
	26e7	29.24	37.61	33.09	0.00	0.00	0.02	0.00	0.01	0.03
	26e8	28.08	38.80	33.10	0.00	0.00	0.02	0.00	0.00	0.00
	26e9	29.52	37.30	33.13	0.00	0.00	0.00	0.00	0.02	0.03
	26e10	27.89	39.34	32.74	0.00	0.00	0.01	0.00	0.00	0.02
	26e11	29.34	37.65	33.00	0.00	0.00	0.00	0.00	0.00	0.00
	26e12	29.12	37.89	32.94	0.00	0.00	0.01	0.01	0.02	0.00
	26e13	28.54	38.33	33.07	0.00	0.00	0.01	0.03	0.00	0.01
	26e14	29.19	38.07	32.69	0.00	0.00	0.01	0.00	0.01	0.03
	26e15	29.20	37.76	33.02	0.00	0.00	0.00	0.01	0.00	0.01
	26e16	29.29	37.83	32.86	0.00	0.00	0.00	0.00	0.00	0.01
	26e17	29.39	37.59	32.99	0.00	0.00	0.02	0.00	0.00	0.00
	26e18	29.82	37.17	32.98	0.00	0.00	0.00	0.00	0.01	0.01
	26e19	30.02	37.00	32.97	0.00	0.00	0.00	0.00	0.01	0.00
	26e20	29.45	37.60	32.93	0.00	0.00	0.00	0.01	0.00	0.01
	26e21	28.83	38.08	33.02	0.00	0.00	0.04	0.02	0.00	0.01
	26e22	29.00	38.13	32.84	0.00	0.00	0.00	0.00	0.00	0.01
	26e23	29.01	38.08	32.88	0.00	0.00	0.00	0.02	0.00	0.01
5320	20-1	31.68	31.60	33.21	0.00	0.00	0.00	0.03	0.00	0.04
	20-2	31.81	31.80	33.07	0.00	0.00	0.00	0.00	0.03	0.04
	20-3	27.73	27.70	32.57	0.00	0.02	0.00	0.01	0.02	0.00
	20-4	28.24	28.20	32.79	0.00	0.00	0.02	0.01	0.00	0.00
	20-5	27.64	27.60	32.48	0.00	0.00	0.00	0.01	0.00	0.02
	20-6	27.40	27.40	32.60	0.00	0.00	0.01	0.00	0.00	0.01
	20-7	28.46	28.50	32.76	0.00	0.00	0.00	0.00	0.00	0.00
	20-8	28.07	28.10	32.88	0.00	0.00	0.01	0.00	0.00	0.00
	20-9	28.33	28.30	33.12	0.00	0.00	0.00	0.00	0.00	0.01
	20-10	27.55	27.50	32.78	0.00	0.00	0.00	0.01	0.00	0.01
	20-11	29.34	29.30	33.08	0.00	0.00	0.00	0.00	0.00	0.00
	20-12	27.76	27.80	32.74	0.00	0.00	0.00	0.00	0.01	0.01
	20-13	29.00	29.00	32.97	0.00	0.02	0.00	0.01	0.01	0.02
4449	49-1	29.38	37.88	32.71	0.00	0.00	0.02	0.01	0.00	0.00
	49-2	28.70	38.69	32.55	0.00	0.00	0.03	0.00	0.00	0.03
	49-4	29.31	37.92	32.71	0.00	0.00	0.01	0.00	0.02	0.02
	49-5	28.87	38.33	32.77	0.00	0.00	0.01	0.00	0.00	0.01
	49d-1	29.20	37.81	32.89	0.00	0.04	0.03	0.00	0.01	0.03

sample	label	A%(As)	A%(S)	A%(Fe)	A%(Mn)	A%(Co)	A%(Ni)	A%(Cu)	A%(Zn)	A%(Sb)
4449	49d-2	29.31	37.75	32.83	0.00	0.01	0.03	0.01	0.02	0.04
	49d-3	28.04	38.97	32.92	0.00	0.03	0.02	0.00	0.02	0.00
	49d-5	29.22	37.94	32.75	0.00	0.03	0.04	0.00	0.00	0.01
	49d-6	29.23	37.77	32.93	0.00	0.04	0.01	0.00	0.00	0.01
	49d-10	29.72	37.43	32.71	0.00	0.04	0.01	0.00	0.07	0.02
	49d-11	29.17	38.27	32.52	0.00	0.00	0.03	0.01	0.00	0.00
	49d-12	29.40	37.63	32.89	0.00	0.04	0.02	0.01	0.01	0.01
	49d-13	29.42	37.72	32.82	0.00	0.03	0.01	0.00	0.00	0.01
	49d-15	29.26	37.92	32.74	0.00	0.05	0.00	0.02	0.00	0.00
	49d-16	29.55	37.33	33.01	0.00	0.02	0.01	0.01	0.01	0.06
	49d-17	29.05	38.02	32.82	0.00	0.04	0.04	0.01	0.00	0.03
	49d-18	28.92	38.30	32.70	0.00	0.05	0.03	0.00	0.00	0.01
	49d-19	30.39	37.52	32.07	0.00	0.00	0.00	0.00	0.00	0.02
	49d-20	29.39	37.74	32.75	0.00	0.06	0.03	0.00	0.00	0.03
	49f-1	28.55	38.51	32.90	0.00	0.00	0.02	0.01	0.00	0.01
	49f-2	29.30	37.66	32.98	0.00	0.04	0.00	0.00	0.01	0.01
	49f-3	28.39	38.63	32.90	0.00	0.00	0.02	0.00	0.01	0.05
	49f-4	29.39	37.62	32.89	0.00	0.00	0.04	0.02	0.00	0.03
	49f-5	27.47	39.70	32.76	0.00	0.02	0.04	0.00	0.00	0.00
	49f-6	28.16	38.95	32.84	0.00	0.00	0.03	0.00	0.00	0.02
	49f-7	29.21	38.05	32.71	0.00	0.00	0.00	0.00	0.01	0.02
	49f-8	28.62	37.86	33.47	0.00	0.00	0.03	0.01	0.00	0.00
5354	54a-1	28.99	37.97	32.99	0.00	0.02	0.00	0.01	0.01	0.01
	54a-2	28.35	38.76	32.87	0.00	0.01	0.00	0.01	0.00	0.00
	54a-3	29.09	37.92	32.91	0.00	0.00	0.03	0.03	0.00	0.02
	54a-4	28.78	38.26	32.92	0.00	0.00	0.00	0.00	0.03	0.01
	54a-5	29.53	37.33	33.09	0.00	0.00	0.00	0.02	0.02	0.01
	54a-6	29.07	37.84	33.04	0.00	0.00	0.01	0.01	0.01	0.01
	54a-7	28.67	38.21	33.07	0.00	0.02	0.00	0.00	0.03	0.00
	54a-8	29.06	38.11	32.77	0.00	0.00	0.00	0.03	0.01	0.01
	54a-9	29.77	37.28	32.92	0.00	0.00	0.01	0.00	0.00	0.01
	54a-10	29.82	37.49	32.68	0.00	0.00	0.00	0.01	0.00	0.01
	54a-11	29.22	37.99	32.69	0.00	0.04	0.03	0.02	0.00	0.01
	54a-12	29.52	37.41	33.03	0.00	0.01	0.01	0.00	0.01	0.01
	54a-13	29.21	37.66	33.12	0.00	0.01	0.00	0.00	0.00	0.00
	54a-14	29.48	37.42	33.07	0.00	0.00	0.00	0.01	0.00	0.00
	54a-15	29.20	37.66	33.14	0.00	0.00	0.00	0.00	0.00	0.01
	54a-16	29.98	37.27	32.73	0.00	0.00	0.00	0.01	0.00	0.01
	54a-17	29.03	38.12	32.81	0.00	0.00	0.00	0.01	0.02	0.01
	54a-18	29.88	37.49	32.62	0.00	0.00	0.00	0.00	0.00	0.01
	54a-19	27.95	39.08	32.84	0.00	0.09	0.02	0.02	0.00	0.00
	54a-20	29.36	38.04	32.59	0.00	0.00	0.01	0.00	0.00	0.00
	54a-21	29.48	37.52	32.96	0.00	0.00	0.01	0.00	0.02	0.00
	54a-22	29.02	38.13	32.85	0.00	0.00	0.00	0.00	0.00	0.00
	54a-23	29.03	38.01	32.95	0.00	0.01	0.00	0.00	0.00	0.00
	54a-24	29.42	37.74	32.82	0.00	0.00	0.01	0.01	0.00	0.00
	54b-1	28.79	38.53	32.64	0.00	0.00	0.03	0.01	0.00	0.00
	54b-2	29.07	38.51	32.38	0.00	0.00	0.01	0.01	0.01	0.01
	54b-3	29.23	37.92	32.82	0.00	0.00	0.00	0.01	0.01	0.01
	54b-4	29.13	37.85	32.91	0.00	0.00	0.03	0.02	0.05	0.00
	54b-5	28.71	38.40	32.83	0.00	0.00	0.01	0.02	0.03	0.00
	54b-6	29.07	38.51	32.40	0.00	0.00	0.01	0.00	0.00	0.00
	54b-7	29.27	37.98	32.73	0.00	0.00	0.00	0.00	0.00	0.02
	54b-8	29.63	37.58	32.76	0.00	0.00	0.01	0.01	0.02	0.00
	54b-9	28.64	38.57	32.75	0.00	0.01	0.01	0.02	0.00	0.00

sample	label	A%(As)	A%(S)	A%(Fe)	A%(Mn)	A%(Co)	A%(Ni)	A%(Cu)	A%(Zn)	A%(Sb)
5354	54b-10	29.23	38.33	32.38	0.00	0.02	0.01	0.03	0.01	0.00
	54b-11	29.26	37.93	32.76	0.00	0.00	0.01	0.01	0.02	0.01
	54b-12	28.64	38.51	32.84	0.00	0.00	0.00	0.00	0.00	0.00
	54b-13	28.70	38.51	32.75	0.00	0.00	0.03	0.00	0.00	0.01
	54b-14	28.51	38.87	32.62	0.00	0.00	0.00	0.00	0.00	0.00
	54b-15	28.68	38.55	32.74	0.00	0.00	0.00	0.00	0.02	0.00
	54b-16	29.40	38.03	32.52	0.00	0.00	0.00	0.01	0.02	0.02
	54b-17	30.23	36.68	33.05	0.00	0.00	0.00	0.00	0.03	0.00
	54b-18	29.24	38.15	32.57	0.00	0.00	0.02	0.00	0.01	0.00
	54b-19	28.63	38.66	32.66	0.00	0.01	0.01	0.02	0.00	0.01
	54b-20	29.52	37.96	32.51	0.00	0.00	0.00	0.00	0.00	0.01
	54b-21	29.36	37.73	32.87	0.00	0.00	0.01	0.01	0.01	0.00
	54b-22	29.23	38.08	32.66	0.00	0.00	0.01	0.00	0.00	0.01
	54c-1	27.83	39.14	32.73	0.00	0.00	0.04	0.26	0.00	0.00
	54c-2	29.32	37.48	32.81	0.00	0.00	0.02	0.35	0.01	0.02
	54c-3	29.16	37.70	32.80	0.00	0.00	0.03	0.29	0.02	0.00
	54c-4	28.61	38.73	32.56	0.00	0.01	0.00	0.09	0.00	0.00
	54c-5	29.11	37.71	32.95	0.00	0.00	0.00	0.22	0.00	0.00
	54c-6	27.75	39.16	32.53	0.00	0.00	0.02	0.51	0.02	0.00
	54c-7	28.74	37.61	32.66	0.00	0.00	0.00	0.97	0.00	0.01
	54d-1	27.47	39.53	32.84	0.00	0.13	0.00	0.01	0.00	0.01
	54d-2	29.55	37.31	33.13	0.00	0.01	0.00	0.00	0.00	0.00
	54d-3	29.41	37.90	32.65	0.00	0.00	0.00	0.00	0.01	0.02
	54d-4	29.08	38.32	32.55	0.00	0.02	0.00	0.00	0.00	0.03
	54d-5	29.40	38.11	32.44	0.00	0.00	0.01	0.02	0.01	0.01
	54d-6	29.28	37.76	32.96	0.00	0.00	0.00	0.00	0.00	0.00
	54d-7	29.51	37.71	32.73	0.00	0.03	0.01	0.00	0.00	0.02
	54d-8	29.82	37.20	32.92	0.00	0.03	0.02	0.00	0.00	0.01
	54d-9	29.61	37.70	32.65	0.00	0.00	0.00	0.00	0.00	0.04
	54d-10	29.09	37.96	32.91	0.00	0.01	0.00	0.00	0.00	0.02
	54d-11	29.11	37.81	33.07	0.00	0.00	0.01	0.00	0.00	0.00
	54d-12	30.34	36.57	33.07	0.00	0.00	0.00	0.00	0.01	0.00
	54d-13	28.94	38.56	32.48	0.00	0.00	0.00	0.01	0.01	0.00
	54d-14	29.21	37.89	32.87	0.00	0.00	0.03	0.00	0.00	0.00
	54d-15	28.27	38.97	32.68	0.00	0.03	0.02	0.00	0.01	0.00
	54d-16	29.45	37.74	32.78	0.00	0.00	0.00	0.03	0.00	0.00
	54d-17	27.86	39.26	32.77	0.00	0.06	0.02	0.00	0.04	0.00
	54d-18	29.27	37.82	32.84	0.00	0.02	0.02	0.01	0.03	0.00
	54d-19	30.15	37.17	32.65	0.00	0.02	0.00	0.00	0.00	0.01
	54d-20	28.78	38.18	33.03	0.00	0.00	0.00	0.01	0.00	0.00
	54d-21	29.44	37.47	33.07	0.00	0.01	0.00	0.00	0.00	0.01
	54d-22	29.39	37.81	32.76	0.00	0.00	0.00	0.02	0.02	0.00
	54d-23	28.95	38.43	32.59	0.00	0.00	0.00	0.02	0.00	0.00
	54d-24	29.03	37.89	32.99	0.00	0.01	0.03	0.01	0.02	0.02
	54d-25	29.74	37.84	32.39	0.00	0.00	0.00	0.00	0.00	0.02
	54d-26	29.39	37.66	32.92	0.00	0.01	0.00	0.02	0.00	0.00
	54d-27	29.71	37.98	32.26	0.00	0.00	0.00	0.02	0.01	0.00
	54d-28	28.74	38.47	32.72	0.00	0.02	0.02	0.00	0.02	0.02
	54d-29	29.35	37.84	32.76	0.00	0.00	0.01	0.01	0.00	0.03
	54d-30	29.33	37.70	32.92	0.00	0.02	0.00	0.00	0.00	0.03
	54d-31	30.12	37.32	32.51	0.00	0.03	0.01	0.00	0.00	0.01
	54d-32	28.27	38.80	32.88	0.00	0.03	0.00	0.01	0.00	0.01
	54d-33	28.99	37.95	32.99	0.00	0.00	0.02	0.02	0.02	0.01
	54d-34	29.16	37.87	32.93	0.00	0.00	0.00	0.02	0.00	0.00
	54d-35	29.82	37.20	32.95	0.00	0.00	0.00	0.00	0.00	0.02
	54d-36	29.06	37.83	33.08	0.00	0.01	0.00	0.01	0.00	0.00
	54f-1	29.29	38.03	32.54	0.00	0.00	0.01	0.12	0.00	0.01

sample	label	A%(As)	A%(S)	A%(Fe)	A%(Mn)	A%(Co)	A%(Ni)	A%(Cu)	A%(Zn)	A%(Sb)
5354	54f-2	29.40	37.69	32.76	0.00	0.00	0.00	0.14	0.00	0.00
	54i-1	27.25	40.06	32.60	0.00	0.05	0.01	0.00	0.01	0.01
	54i-2	27.92	39.06	32.96	0.00	0.04	0.01	0.00	0.00	0.00
	54i-3	28.91	37.74	33.31	0.00	0.00	0.02	0.01	0.01	0.01
	54i-4	30.34	36.65	32.98	0.00	0.00	0.01	0.01	0.00	0.01
	54k-1	29.74	37.21	32.99	0.00	0.00	0.02	0.00	0.02	0.01
	54k-2	29.64	37.38	32.95	0.00	0.00	0.03	0.00	0.00	0.00
	54k-3	28.43	38.57	32.94	0.00	0.02	0.02	0.00	0.02	0.00
	54k-4	29.48	37.74	32.77	0.00	0.00	0.01	0.00	0.00	0.00
	54k-5	29.65	37.41	32.91	0.00	0.00	0.01	0.00	0.00	0.02
5376	76-2	28.22	38.97	32.67	0.00	0.00	0.01	0.02	0.00	0.11
	76-3	29.09	38.05	32.68	0.00	0.00	0.00	0.00	0.08	0.10
	76-4	29.02	38.23	32.66	0.00	0.00	0.00	0.00	0.03	0.05
	76-5	28.84	38.37	32.73	0.00	0.00	0.00	0.00	0.04	0.01
	76b-1	29.14	38.10	32.70	0.00	0.00	0.01	0.03	0.02	0.00
	76b-2	28.85	38.51	32.56	0.00	0.00	0.00	0.02	0.01	0.06
	76b-3	28.74	38.53	32.67	0.00	0.00	0.00	0.00	0.01	0.04
	76b-4	27.40	39.83	32.72	0.00	0.00	0.01	0.00	0.00	0.03
	76c-1	29.09	38.20	32.65	0.00	0.00	0.00	0.01	0.00	0.04
	76c-2	29.24	37.90	32.79	0.00	0.00	0.02	0.00	0.03	0.02
	76c-3	28.75	38.50	32.70	0.00	0.00	0.00	0.01	0.00	0.02
	76c-4	28.44	38.55	32.96	0.00	0.00	0.00	0.00	0.00	0.04
	76c-5	29.22	38.20	32.52	0.00	0.00	0.00	0.00	0.00	0.06
	76c-6	28.77	38.35	32.81	0.00	0.00	0.01	0.01	0.00	0.05
	76c-7	27.88	39.48	32.62	0.00	0.00	0.00	0.02	0.00	0.00
	76c-8	29.11	37.95	32.87	0.00	0.00	0.00	0.03	0.00	0.04
	76c-9	28.60	38.50	32.75	0.00	0.00	0.01	0.00	0.03	0.09
	76c-10	28.52	38.86	32.57	0.00	0.00	0.00	0.00	0.00	0.04
	76c-11	29.31	37.95	32.69	0.00	0.00	0.00	0.00	0.02	0.03
	76c-12	28.63	38.70	32.62	0.00	0.00	0.00	0.01	0.01	0.02
	76c-13	28.78	38.48	32.66	0.00	0.00	0.01	0.04	0.00	0.02
	76c-14	27.95	39.21	32.72	0.00	0.00	0.02	0.00	0.03	0.06
	76c-15	28.60	38.67	32.68	0.00	0.00	0.03	0.00	0.00	0.01
	76c-16	28.99	38.37	32.59	0.00	0.01	0.00	0.00	0.00	0.04
	76c-17	28.88	38.35	32.72	0.00	0.00	0.01	0.01	0.00	0.02
	76c-18	28.78	38.34	32.85	0.00	0.00	0.00	0.01	0.00	0.02
	76c-19	28.47	38.95	32.42	0.00	0.00	0.00	0.01	0.07	0.08
	76c-20	28.27	39.00	32.61	0.00	0.00	0.00	0.00	0.03	0.09
	76c-21	28.93	38.45	32.53	0.00	0.00	0.00	0.00	0.02	0.07
	76c-23	27.44	39.88	32.64	0.00	0.00	0.01	0.01	0.00	0.02
	76c-24	28.91	38.41	32.59	0.00	0.00	0.00	0.00	0.02	0.05
	76c-25	28.65	38.53	32.69	0.00	0.01	0.01	0.00	0.04	0.07
	76c-26	29.44	38.06	32.45	0.00	0.00	0.00	0.00	0.03	0.03
76c-27	29.32	38.07	32.59	0.00	0.00	0.01	0.00	0.00	0.02	
76c-28	29.81	37.65	32.53	0.00	0.00	0.00	0.01	0.00	0.00	
76c-29	27.84	39.48	32.62	0.00	0.00	0.00	0.00	0.00	0.06	
76c-30	27.96	39.21	32.78	0.00	0.00	0.03	0.00	0.00	0.01	
76c-31	28.35	39.10	32.51	0.00	0.00	0.00	0.00	0.00	0.03	
76c-32	27.45	39.89	32.64	0.00	0.00	0.00	0.00	0.00	0.02	
76c-33	28.18	39.20	32.56	0.00	0.00	0.01	0.01	0.00	0.03	
5375	75d-1	29.20	38.58	32.21	0.00	0.00	0.00	0.00	0.00	0.00
	75d-2	28.33	39.08	32.57	0.00	0.00	0.02	0.01	0.00	0.01
	75d-3	27.60	40.01	32.37	0.00	0.00	0.00	0.00	0.01	0.00

sample	label	A%(As)	A%(S)	A%(Fe)	A%(Mn)	A%(Co)	A%(Ni)	A%(Cu)	A%(Zn)	A%(Sb)
5375	75d-4	28.45	38.77	32.69	0.00	0.00	0.00	0.06	0.00	0.02
	75d-5	28.10	39.45	32.43	0.00	0.00	0.00	0.01	0.00	0.01
	75d-6	28.89	38.65	32.44	0.00	0.00	0.00	0.01	0.02	0.00
	75d-7	28.36	38.94	32.62	0.00	0.03	0.03	0.00	0.01	0.00
	75d-8	28.28	39.18	32.52	0.00	0.01	0.00	0.00	0.00	0.01
	75d-9	29.36	38.33	32.17	0.00	0.00	0.00	0.09	0.01	0.03
	75d-10	29.14	38.24	32.59	0.00	0.00	0.02	0.00	0.00	0.02
	75d-11	29.47	38.04	32.46	0.00	0.00	0.01	0.00	0.00	0.01
	75d-12	29.53	37.94	32.47	0.00	0.00	0.02	0.00	0.02	0.01
	75d-13	29.12	38.44	32.41	0.00	0.00	0.00	0.00	0.02	0.02
	75e	28.68	38.55	32.54	0.00	0.00	0.01	0.13	0.00	0.09
	75e1	27.99	39.66	32.21	0.00	0.00	0.00	0.13	0.00	0.00
	75e2	29.48	37.71	32.77	0.00	0.00	0.02	0.00	0.00	0.02
	75e3	29.37	37.95	32.65	0.00	0.00	0.01	0.00	0.00	0.01
	75e4'	29.14	38.10	32.70	0.00	0.00	0.00	0.03	0.01	0.02
	75f-1	28.10	39.53	32.32	0.00	0.00	0.00	0.04	0.00	0.01
	75f-2	28.04	39.35	32.57	0.00	0.00	0.02	0.00	0.00	0.02
	75f-3	28.07	39.35	32.53	0.00	0.00	0.00	0.02	0.02	0.02
	75f-4	28.53	39.04	32.36	0.00	0.00	0.00	0.00	0.00	0.07
	75f-5	28.11	39.31	32.55	0.00	0.00	0.00	0.00	0.00	0.03
	75f-6	27.98	39.60	32.36	0.00	0.00	0.02	0.00	0.00	0.04
	75f-7	28.62	38.72	32.51	0.00	0.00	0.01	0.01	0.00	0.13
	75f-8	28.35	39.15	32.42	0.00	0.00	0.00	0.02	0.00	0.05
	75f-9	28.27	39.28	32.42	0.00	0.00	0.01	0.00	0.00	0.01
	75f-10	28.17	39.36	32.45	0.00	0.00	0.00	0.00	0.00	0.01
	75f-11	27.76	39.70	32.50	0.00	0.00	0.01	0.00	0.00	0.03
	75f-12	27.99	39.37	32.58	0.00	0.00	0.01	0.01	0.02	0.02
	75f-13	27.48	40.00	32.52	0.00	0.00	0.00	0.00	0.00	0.00
	75f-14	27.84	39.71	32.40	0.00	0.00	0.01	0.01	0.00	0.03
	75g-1	28.68	38.64	32.57	0.00	0.00	0.00	0.00	0.00	0.10
	75g-2	28.76	38.37	32.72	0.00	0.00	0.01	0.00	0.01	0.12
	75g-3	28.60	38.44	32.86	0.00	0.00	0.00	0.00	0.00	0.10
	75g-4	28.64	38.83	32.44	0.00	0.00	0.00	0.00	0.01	0.08
	75g-5	28.60	38.32	32.97	0.00	0.00	0.00	0.00	0.00	0.10
	75g-6	28.65	38.55	32.75	0.00	0.00	0.01	0.01	0.00	0.03
	75g-7	28.44	38.91	32.63	0.00	0.01	0.00	0.01	0.01	0.01
	75g-8	28.31	38.98	32.64	0.00	0.00	0.00	0.00	0.03	0.03
	75g-9	28.95	38.34	32.65	0.00	0.00	0.00	0.02	0.00	0.03
	75g-10	28.81	38.52	32.62	0.00	0.00	0.00	0.00	0.00	0.05
	75g-11	28.20	39.29	32.43	0.00	0.00	0.01	0.01	0.00	0.06
	75g-12	28.30	39.23	32.40	0.00	0.00	0.02	0.00	0.01	0.04
	75g-13	27.98	39.73	32.28	0.00	0.00	0.00	0.00	0.00	0.01
	75g-14	28.48	39.44	32.00	0.00	0.00	0.02	0.02	0.01	0.03
	75g-15	28.25	39.16	32.59	0.00	0.00	0.00	0.00	0.00	0.00
	75g-16	28.89	38.49	32.55	0.00	0.00	0.00	0.01	0.04	0.02
	75g-17	28.89	38.51	32.55	0.00	0.00	0.00	0.02	0.00	0.03
	75g-18	28.64	38.92	32.42	0.00	0.00	0.00	0.00	0.00	0.01
	75g-19	28.15	39.23	32.62	0.00	0.00	0.00	0.00	0.00	0.00
	75h-1	28.77	38.69	32.48	0.00	0.00	0.01	0.00	0.00	0.04
	75h-2	28.23	39.15	32.54	0.00	0.00	0.02	0.00	0.00	0.05
	75h-3	28.52	38.65	32.69	0.00	0.00	0.02	0.03	0.00	0.09
	75h-4	28.44	38.87	32.62	0.00	0.00	0.02	0.00	0.01	0.05
	75i-1	28.75	38.77	32.43	0.00	0.00	0.00	0.00	0.01	0.03
	75i-2	28.76	38.34	32.85	0.00	0.00	0.01	0.00	0.00	0.04
	75i-3	29.42	38.21	32.31	0.00	0.00	0.02	0.00	0.00	0.04
	75i-4	28.75	38.89	32.28	0.00	0.00	0.00	0.00	0.02	0.05
	75i-5	29.18	38.28	32.50	0.00	0.00	0.00	0.00	0.00	0.03

sample	label	A%(As)	A%(S)	A%(Fe)	A%(Mn)	A%(Co)	A%(Ni)	A%(Cu)	A%(Zn)	A%(Sb)
5375	75i-6	29.09	38.58	32.30	0.00	0.00	0.00	0.00	0.00	0.03
	75i-7	27.86	39.79	32.32	0.00	0.00	0.00	0.00	0.00	0.03
	75i-8	29.62	38.10	32.25	0.00	0.00	0.00	0.00	0.01	0.02
	75j-1	27.56	39.75	32.67	0.00	0.00	0.00	0.00	0.00	0.03
	75j-2	27.69	39.81	32.46	0.00	0.00	0.00	0.00	0.01	0.03
	75j-3	27.87	39.60	32.51	0.00	0.01	0.00	0.00	0.00	0.01
	75j-4	28.09	39.27	32.61	0.00	0.00	0.01	0.00	0.00	0.01
	75j-5	28.57	38.66	32.67	0.00	0.01	0.00	0.01	0.00	0.07
	75j-6	27.57	39.02	33.35	0.00	0.00	0.02	0.00	0.00	0.04
	75j-7	28.86	38.60	32.49	0.00	0.00	0.00	0.00	0.00	0.03
	75j-8	28.34	39.22	32.36	0.00	0.00	0.00	0.01	0.01	0.06
	75k-1	28.92	38.58	32.43	0.00	0.00	0.00	0.02	0.00	0.04
	75k-2	27.15	40.35	32.47	0.00	0.00	0.01	0.00	0.00	0.01
	75k-3	28.55	38.82	32.60	0.00	0.00	0.00	0.00	0.00	0.02
	75k-4	29.20	37.74	32.97	0.00	0.00	0.00	0.00	0.02	0.06
	75k-5	28.24	39.21	32.51	0.00	0.00	0.00	0.00	0.00	0.02
	75k-6	28.39	39.02	32.58	0.00	0.00	0.01	0.00	0.00	0.00
	75k-7	28.81	38.38	32.77	0.00	0.00	0.01	0.00	0.03	0.00
	75k-8	28.27	38.97	32.70	0.00	0.00	0.00	0.03	0.00	0.03
	75k-9	27.61	39.82	32.55	0.00	0.00	0.00	0.01	0.00	0.02
	75k-10	28.20	39.19	32.59	0.00	0.00	0.00	0.01	0.00	0.01
	75k-11	26.72	40.79	32.45	0.00	0.00	0.02	0.00	0.00	0.02
	75k-12	27.98	39.74	32.25	0.00	0.00	0.01	0.00	0.00	0.03
	75k-13	27.57	40.03	32.36	0.00	0.00	0.01	0.01	0.00	0.00
	75k-14	27.78	39.48	32.70	0.00	0.00	0.02	0.00	0.00	0.01
	75k-15	27.71	39.87	32.37	0.00	0.00	0.00	0.00	0.03	0.03
	75k-16	28.61	38.93	32.45	0.00	0.00	0.00	0.00	0.00	0.01
	75k-17	28.18	39.53	32.28	0.00	0.00	0.00	0.00	0.00	0.00
	75k-18	29.02	38.38	32.55	0.00	0.02	0.02	0.00	0.00	0.00
	75k-19	28.20	39.57	32.23	0.00	0.00	0.00	0.00	0.00	0.00
	75k-20	29.20	38.45	32.29	0.00	0.00	0.00	0.01	0.03	0.02
	75k-21	28.71	38.47	32.75	0.00	0.00	0.00	0.01	0.01	0.04
	75k-22	28.19	39.27	32.50	0.00	0.00	0.00	0.00	0.02	0.02
	75k-23	28.07	39.44	32.44	0.00	0.00	0.02	0.00	0.00	0.03
	75k-24	28.25	39.25	32.45	0.00	0.00	0.02	0.01	0.00	0.02
	75k-25	28.61	39.08	32.30	0.00	0.00	0.00	0.00	0.00	0.01
4447	47a-1	29.65	37.24	33.06	0.00	0.00	0.00	0.01	0.00	0.04
	47a-2	29.49	37.61	32.88	0.00	0.00	0.00	0.00	0.01	0.01
	47a-3	29.61	37.27	33.08	0.00	0.00	0.00	0.01	0.01	0.01
	47a-4	29.10	37.86	33.02	0.00	0.01	0.00	0.00	0.00	0.00
	47a-5	29.05	37.94	33.00	0.00	0.00	0.00	0.00	0.00	0.00
	47a-6	29.27	37.78	32.89	0.00	0.01	0.00	0.00	0.03	0.02
	47a-7	29.67	37.29	33.01	0.00	0.01	0.00	0.01	0.00	0.00
	47a-8	29.92	36.82	33.20	0.00	0.02	0.00	0.02	0.00	0.02
	47a-9	29.58	37.40	32.98	0.00	0.00	0.00	0.02	0.00	0.02
	47b-1	28.95	37.99	33.01	0.00	0.01	0.00	0.00	0.05	0.00
	47b-2	28.77	38.18	33.00	0.00	0.03	0.00	0.00	0.00	0.02
	47b-3	29.44	37.79	32.71	0.00	0.00	0.00	0.00	0.04	0.02
	47b-4	29.46	37.41	33.08	0.00	0.00	0.00	0.03	0.00	0.02
	47b-5	29.32	37.64	32.96	0.00	0.03	0.00	0.03	0.00	0.02
	47b-6	29.31	37.68	32.99	0.00	0.00	0.00	0.00	0.01	0.01
	47b-7	28.57	38.54	32.85	0.00	0.02	0.00	0.02	0.00	0.00
	47b-8	27.87	39.75	32.33	0.00	0.02	0.00	0.03	0.00	0.00
	47b-9	28.87	38.39	32.69	0.00	0.05	0.00	0.00	0.00	0.01
	47c-1	29.31	37.57	33.07	0.00	0.01	0.00	0.02	0.01	0.01

sample label	A%(As)	A%(S)	A%(Fe)	A%(Mn)	A%(Co)	A%(Ni)	A%(Cu)	A%(Zn)	A%(Sb)
4447 47c-2	29.50	37.58	32.89	0.00	0.00	0.00	0.01	0.00	0.02
47c-3	28.98	38.09	32.93	0.00	0.00	0.00	0.00	0.00	0.00
47c-5	28.95	38.28	32.74	0.00	0.00	0.00	0.01	0.02	0.00
47c-6	28.78	38.58	32.63	0.00	0.00	0.00	0.00	0.00	0.01
47c-7	29.61	37.53	32.83	0.00	0.02	0.00	0.00	0.01	0.00
47d-1	29.51	37.48	32.97	0.00	0.00	0.00	0.00	0.02	0.02
47d-2	29.05	38.09	32.85	0.00	0.00	0.00	0.00	0.00	0.00
47d-3	29.11	38.19	32.67	0.00	0.00	0.00	0.00	0.00	0.02
47d-4	29.52	37.31	33.11	0.00	0.00	0.00	0.00	0.01	0.05
47d-5	28.60	38.40	32.99	0.00	0.01	0.00	0.00	0.00	0.01
47d-6	30.46	36.31	33.16	0.00	0.04	0.00	0.00	0.03	0.01
47d-7	29.85	37.21	32.88	0.00	0.02	0.00	0.00	0.00	0.04
47d-8	29.24	37.96	32.78	0.00	0.00	0.00	0.00	0.00	0.01
47d-9	30.04	36.74	33.19	0.00	0.01	0.00	0.00	0.00	0.01
47d-10	29.26	37.70	32.92	0.00	0.08	0.00	0.01	0.00	0.02
47d-11	27.94	39.34	32.65	0.00	0.03	0.00	0.00	0.02	0.01
47d-12	27.59	39.42	32.98	0.00	0.00	0.00	0.00	0.00	0.00
47d-13	28.93	38.01	33.05	0.00	0.00	0.00	0.00	0.00	0.01
47d-14	29.76	37.39	32.80	0.00	0.00	0.00	0.00	0.01	0.04
47d-15	29.75	37.44	32.77	0.00	0.00	0.00	0.01	0.00	0.03
47f-1	29.08	37.88	33.01	0.00	0.02	0.00	0.00	0.00	0.01
47f-2	28.95	38.18	32.84	0.00	0.00	0.00	0.01	0.00	0.02
47f-3	29.63	37.28	33.07	0.00	0.00	0.00	0.00	0.00	0.01
47f-4	29.72	37.44	32.80	0.00	0.00	0.00	0.01	0.00	0.03
47f-5	28.89	38.08	33.02	0.00	0.00	0.00	0.00	0.00	0.01
47f-6	29.56	37.34	33.08	0.00	0.00	0.00	0.00	0.02	0.00
47f-7	29.06	37.92	33.01	0.00	0.00	0.00	0.01	0.00	0.00
47f-8	29.35	37.90	32.72	0.00	0.02	0.00	0.00	0.00	0.01
47f-9	28.94	38.20	32.83	0.00	0.00	0.00	0.01	0.00	0.02
47f-10	29.04	38.21	32.74	0.00	0.00	0.00	0.00	0.00	0.01
47f-11	28.77	38.36	32.86	0.00	0.00	0.00	0.00	0.00	0.00
47f-12	28.31	38.80	32.86	0.00	0.00	0.00	0.02	0.00	0.00
47f-13	29.18	37.89	32.93	0.00	0.00	0.00	0.00	0.00	0.00
47f-14	29.44	37.25	33.27	0.00	0.00	0.00	0.02	0.00	0.02
47f-15	29.52	37.56	32.92	0.00	0.00	0.00	0.00	0.00	0.00
47f-16	29.07	37.85	33.05	0.00	0.00	0.00	0.02	0.00	0.00
47f-17	28.27	38.78	32.92	0.00	0.00	0.00	0.01	0.01	0.01
47f-18	29.64	37.49	32.84	0.00	0.00	0.00	0.01	0.00	0.01

APPENDIX D

Step heating $^{40}\text{Ar}/^{39}\text{Ar}$ analyses.

UAF069-26 4448 WM 12-19-97 KETZA

Weighted average of J from standards = 0.009101 +/- 0.000028

Laser Power (mWatt)	Cumulative 39Ar	40Ar/39Ar measured	37Ar/39Ar measured	36Ar/39Ar measured	% Atmospheric 40Ar	37Ca/39K +/-	40*/39K +/-	Age (Ma)	+/- (Ma)
100	0.0077	189.311	0.017	0.631	98.539	0.017	0.001	2.765	15.494
150	0.0153	144.368	0.016	0.491	100.440	0.016	0.001	-0.635	8.774
200	0.0222	81.896	0.029	0.259	93.494	0.029	0.001	5.327	0.623
300	0.0278	46.722	0.102	0.141	89.129	0.102	0.002	5.076	0.376
450	0.0694	18.340	0.065	0.039	62.195	0.065	0.000	6.923	0.218
600	0.1185	10.213	0.006	0.007	21.607	0.006	0.000	7.984	0.049
750	0.1849	8.950	0.004	0.003	8.738	0.004	0.000	8.142	0.024
900	0.2691	8.634	0.005	0.002	5.210	0.005	0.000	8.157	0.051
1050	0.3845	8.213	0.004	0.001	3.416	0.004	0.000	7.905	0.042
1200	0.5053	8.118	0.005	0.001	2.636	0.005	0.000	7.876	0.041
1350	0.6221	8.091	0.006	0.000	1.678	0.006	0.000	7.927	0.036
1500	0.7211	8.413	0.008	0.001	1.931	0.008	0.000	8.222	0.035
1650	0.7909	9.117	0.011	0.001	2.034	0.011	0.000	8.904	0.063
1800	0.8439	9.897	0.015	0.001	1.514	0.015	0.000	9.719	0.027
2000	0.8806	10.879	0.022	0.001	2.080	0.022	0.000	10.625	0.042
3500	0.9464	13.440	0.085	0.001	2.448	0.085	0.000	13.083	0.082
8500	1.0000	15.168	0.883	0.003	5.356	0.884	0.002	14.337	0.136
Integrated		12.927	0.062	0.014	32.173	0.062	0.000	8.749	0.137
								138.2	2.1

APPENDIX E

Sample preparation for lead isotopic analyses.

Sample preparation procedure for Pb-Pb analyses

1. Picking sulphides (Childe, 1997)

Chip out sulphide fragments from the hand sample. Crush the fragments in a plastic rock sample bag, and separate the cleanest pieces in a plastic watch glass. Re-crush the clean portion in another plastic bag, and pour contents into the second half of the plastic watch glass. Pour ethanol in the watch glass, and separate the cleanest grains with clean tweezers, under a binocular microscope.

2. Picking carbonate rock

Chip out a clean fragment from the hand specimen. Crush the fragment in a plastic rock sample bag to chip sizes approximately 3-5 mm in diameter. Separate cleanest pieces with clean tweezers into a small beaker.

3. Acid cleaning and dissolution (Childe, 1997)

Acid cleaning (sulphides, except for galena):

- Move sample to savilex beakers.
- Add 1-2 ml 2 bottle 3N HNO₃ and cap.
- Pour off HNO₃. Rinse in acetone three times. Evaporate to dryness in laminar flow hood.
- Add 1-2 ml 2 bottle 6N HCl and cap. Reflux for 10 minutes on low heat.
- Pour off HCl. Rinse in acetone three times. Evaporate to dryness in laminar flow hood.
- Samples are now clean and ready for dissolution.

Dissolution (sulphides, except for galena):

- Add 1-2 ml 2 bottle 3N HNO₃ to each savillex, cap and reflux on hot plate in laminar flow hood for 12 hours (overnight) at 80° C.
- Dry down samples on hot plate in laminar flow hood, and repeat above HNO₃ dissolution for another 12 hours (overnight).

Dissolution and Pb extraction (sulphides, carbonate rock, and galena):

-Uncap beakers and evaporate to dryness on hot plate, maximize separation of beakers. Rinse caps in 2 bottle water and store in hood.

-Handle carefully, sample may be very static. Add 0.5 ml MQ water to wash inside surface of beakers. Take to dryness. Addition of water may be left out of procedures if there is no particulate on sides of beaker.

-Add 0.5 ml 2N HCL and evaporate to moist paste. Do not dry out. This step takes 30 min to 1+ hours, and should be monitored carefully.

-Dissolve paste in 1 ml 1 N HBr on hot plate for 3 days.

-Remove Bio-Rad columns from storage container, rinse with MQ water, and place on rack. Load columns with 1 ml clean Dow 100-200 mesh anionic resin in 6 N HCl, let stand 30 minutes to allow resin to settle. Follow check list below for the two day chemical extraction and purification of Pb:

		1 st day	2 nd day
Clean resin:	add 3-4 ml 6N HCl	_____	_____
	add 2 ml 2B H ₂ O	_____	_____
Equilibrate Columns:	add 2 ml 1N HBr	_____	_____
	add 2 ml 1N HBr	_____	_____
Load sample onto columns in 1N HBr		_____	_____
Wash columns:	add 2 ml 1N HBr	_____	_____
	add 2 ml 1N HBr	_____	_____
Remove HBr:	add 2 ml 2N HCl	_____	_____
	add 2 ml 2N HCl	_____	_____
	Place <i>clean</i> savillex beaker under column		
Elute Pb from columns:	add 2 ml 6N HCl	_____	_____
DAY 2 ONLY:	Add 2-3 drops 0.3N H ₃ PO ₄	_____	_____
Dry on hot plate (3 to 4 hours)		_____	_____
DAY 1 ONLY:	Add 2-3 drops 2N HCl,		(finished!!)
	dry slightly	_____	
DAY 3 ONLY:	Re-dissolve in 1ml 1N HBr,		
	2-3 hours, capped	_____	

At the end of day 2 remove columns from stand, rinse under MQ water to dislodge resin from columns. Return to correct storage container and ultrasonic for 30 minutes. Samples are now ready for isotopic analysis following the procedures outlined for Pb-rich sulphides and sulphosalts.

APPENDIX F

Calculations of mu values for likely Pb reservoirs.

Calculations of average μ values for Early Cambrian limestone and Proterozoic sediments.

Equations and values used:

$$(^{206}\text{Pb}/^{204}\text{Pb})_{t_2} = (^{206}\text{Pb}/^{204}\text{Pb})_{t_1} + \mu(e^{\lambda_1 t_1} - e^{\lambda_1 t_2})$$

$$(^{207}\text{Pb}/^{204}\text{Pb})_{t_2} = (^{207}\text{Pb}/^{204}\text{Pb})_{t_1} + (\mu/137.88) * (e^{\lambda_2 t_1} - e^{\lambda_2 t_2})$$

$$\lambda_1 = 0.155125 * 10^{-9}$$

$$\lambda_2 = 0.98485 * 10^{-9}$$

a) Calculations assuming that Early Cambrian limestone is the principal source of Pb:

$t_1 = 550$ Ma (approximate age of host limestone)

$t_2 = 110$ Ma (approximate age of mineralization)

$$(^{206}\text{Pb}/^{204}\text{Pb})_{t_1} = 18.443 \text{ (from Godwin and Sinclair, 1982)}$$

$$(^{207}\text{Pb}/^{204}\text{Pb})_{t_1} = 15.66 \text{ (from Godwin and Sinclair, 1982)}$$

$$(^{206}\text{Pb}/^{204}\text{Pb})_{t_2} = 19.541 \text{ (average of ratios from vein samples, outliers removed)}$$

$$(^{207}\text{Pb}/^{204}\text{Pb})_{t_2} = 15.745 \text{ (average of ratios from vein samples, outliers removed)}$$

$$(^{206}\text{Pb}/^{204}\text{Pb})_{t_2} = (^{206}\text{Pb}/^{204}\text{Pb})_{t_1} + \mu(e^{\lambda_1 t_1} - e^{\lambda_1 t_2})$$

$$19.541 = 18.443 + \mu(e^{0.0853} - e^{0.0171})$$

$$\mu = 15.271$$

$$(^{207}\text{Pb}/^{204}\text{Pb})_{t_2} = (^{207}\text{Pb}/^{204}\text{Pb})_{t_1} + (\mu/137.88) * (e^{\lambda_2 t_1} - e^{\lambda_2 t_2})$$

$$15.745 = 15.66 + (\mu/137.88) * (e^{0.5417} - e^{0.1083})$$

$$\mu = 19.388$$

$$\text{average } \mu = 17.329$$

b) Calculations assuming that Proterozoic metasediments (basement rocks) are the principal source of Pb:

$t_1 = 1.85$ Ga (approximate basement age)

$t_2 = 110$ Ma (approximate age of mineralization)

$$(^{206}\text{Pb}/^{204}\text{Pb})_{t_1} = 15.497 \text{ (from Godwin and Sinclair, 1982)}$$

$$(^{207}\text{Pb}/^{204}\text{Pb})_{t_1} = 15.269 \text{ (from Godwin and Sinclair, 1982)}$$

$$(^{206}\text{Pb}/^{204}\text{Pb})_{t_2} = 19.541 \text{ (average of ratios from vein samples, outliers removed)}$$

$$(^{207}\text{Pb}/^{204}\text{Pb})_{t_2} = 15.745 \text{ (average of ratios from vein samples, outliers removed)}$$

$$({}^{206}\text{Pb}/{}^{204}\text{Pb})_{t_2} = ({}^{206}\text{Pb}/{}^{204}\text{Pb})_{t_1} + \mu(e^{\lambda_{111}t_2} - e^{\lambda_{1y_2}})$$

$$19.541 = 15.497 + \mu(e^{0.287} - e^{0.0171})$$

$$\mu = 12.83$$

$$({}^{207}\text{Pb}/{}^{204}\text{Pb})_{t_2} = ({}^{207}\text{Pb}/{}^{204}\text{Pb})_{t_1} + (\mu/137.88) * (e^{\lambda_{211}t_2} - e^{\lambda_{2y_2}})$$

$$15.745 = 15.269 + (\mu/137.88) * (e^{1.822} - e^{0.1083})$$

$$\mu = 12.9459$$

$$\text{average } \mu = 12.888$$